Report to Sandia Laboratory on University of Wisconsin Fusion Engineering Program Design Activities for the Light Ion Beam Fusion Target Development Facility from August 1981 to February 1982

B. Badger, R.L. Engelstad, A.M. Hassanein, G.L. Kulcinski, K.J. Lee, E.G. Lovell, T.J. McCarville, G.A. Moses, R.R. Peterson, I.N. Sviatoslavsky, and A. White

February 1982

UWFDM-457

FUSION TECHNOLOGY INSTITUTE

UNIVERSITY OF WISCONSIN

MADISON WISCONSIN

Report to Sandia Laboratory on University of Wisconsin Fusion Engineering Program Design Activities for the Light Ion Beam Fusion Target Development Facility from August 1981 to February 1982

B. Badger, R.L. Engelstad, A.M. Hassanein, G.L. Kulcinski, K.J. Lee, E.G. Lovell, T.J. McCarville, G.A. Moses, R.R. Peterson, I.N. Sviatoslavsky, and A. White

Fusion Technology Institute
University of Wisconsin
1500 Engineering Drive
Madison, WI 53706

http://fti.neep.wisc.edu

February 1982

UWFDM-457

DOE/DP/40161-1

Report to Sandia Laboratory on University of Wisconsin Fusion Engineering Program Design Activities for the Light Ion Beam Fusion Target Development Facility from August 1981 to February 1982

FINAL REPORT

B. Badger, R.L. Engelstad, A.M. Hassanein, G.L. Kulcinski,
K.J. Lee, E.G. Lovell, T.J. McCarville, G.A. Moses,
R.R. Peterson, I.N. Sviatoslavsky, and A. White

Fusion Engineering Program
Nuclear Engineering Department
University of Wisconsin
Madison, WI 53706

February 1982

Prepared for the U.S. Department of Energy Under Contract DE-AS08-81DP40161

UWFDM-457

Table of Contents

1. Introduction and Summary

A. Introduction

This is a progress report outlining our activities during the period August 1981-February 1982. The report is a compendium of Fusion Engineering Program UWFDM documents covering the various tasks undertaken during this seven month time period. As such, it is "informal" and is meant to have a limited distribution outside of UW and Sandia.

Our statement of work for this time period is reproduced below to serve as a focus for the remainder of the report.

Statement of Work

This proposal is for a continuation of research on cavity and first wall design for light ion beam fusion. The work focusses on the design of a Target Development Facility (TDF) to be used for the testing of high yield targets. This facility will also be used for "radiation effects" simulations. In particular, the "kinetic" blast and thermal loadings on the vessel first wall due to pellet emanations both absorbed and unabsorbed by the gas in the vessel will be studied. The results of this effort will fall into four major areas.

1. *A structural frame to support the armor plated first wall will be designed.*

2. *Models will be developed to predict the permissible thermal and mechanical stresses in the first wall, structural frame, and ducts. This will be consistent with an expected lifetime of 1.5×10^4 full yield target shots and 5×10^4 pulsed power shots.*

3. *A method for replacement of the wall panels will be developed, consistent with the mechanical design.*

4. *Neutron activation levels in the vicinity of the wall panels, frame, and components of the beam line will be computed.*

The report is divided into three major parts. Section two is a survey to determine suitable structural materials for the first wall and support frame. Section three is a description of the mechanical design of the first wall and frame. It also includes a discussion of the methods recently developed to analyze the frame's response to the blast overpressure. Section four covers new results in the area of cavity gas dynamics calculations. The appendix gives a list of publications, reports, theses, etc., that have resulted from our work. In the final part of this section we provide an "executive summary" of the progress report.

B. Executive Summary

The Light Ion Beam Fusion Target Development Facility is designed to test high yield targets (200 MJ) at the rate of 10 shots per day for a lifetime of five years. It is expected to be built in the early 1990's time frame. Table I gives typical parameters for this facility. Figure 1 shows a conceptual design of the LIB-TDF. The pulsed power driver is similar in design to the PBFA-I and PBFA-II facilities. There is an oil-filled outer annular tank that contains the Marx capacitor banks. Inside of this is a water filled annular section containing the intermediate storage capacitors and pulse forming lines. The water serves as the dielectric medium. Inside of this are sixty magnetically insulated transmission lines through which the power flows from the "water section" to the ion diodes located outside of the first wall of the target chamber. This section is filled with borated water that serves as a radiation shield. This water shield effectively moderates and absorbs the fusion neutrons. This section can be drained to gain easy access to the target chamber through the diagnostic port on the top. Further drainage will allow the removal of the top "head" of the target chamber for complete access

Table I. Single Pulse Test Facility Parameters

Pellet	
Nature	Cryogenic
Energy requirement	< 4 MJ
Gain	50
Yield	< 200 MJ
Mass	0.5 gm
Radius	0.5 cm
Driver	
Energy in store	15 MJ
Energy at diodes	8 MJ
Diode voltage	4 MV
Ion specie	He^{++}
Ion energy	8 MeV
Power at diodes	200 TW
Pulse width at diodes	40 ns
Response time	1.5 μs
Jitter time	10 ns
Channel	
Length	4.0 m
Current	85 KA
Current rise time	1 μs
Radius at firing time	0.5 cm
Density rarefaction factor	4
Number	60
Channel Laser System	
Laser pulse width	1 μs
Distance from last mirror to pellet	10 m
Beam-aiming mirror radius	5 cm
Beam-aiming mirror mass	0.2 kg
Pellet tracking distance	10 cm
Hydromotion at firing time	Negligible
Aperture vane port radius	2 cm

Table I. (continued)

Aperture open time	200 s
Blanket port radius	10 cm
Pellet Injection and Tracking	
Pellet acceleration	500 m/sec^2 (500 g's)
Accelerator tube length	9 m
Pellet injection velocity	300 m/sec
Allowable beam incidence error	1 mm
Beam-aiming mirror actuator energy	1 J
Cavity Gas	
Type	99.8% Ar, 0.2% Na or N_2
Density	$7 \times 10^{23}/m^3$
Temperature	300°K
Cavity	
Shape	Cylinder
Height	6.0 m
Radius	3.0 m
Overpressure incident on wall	1.7 MPa
Shot repetition rate	10/day
First Wall	
Thickness	3 cm
Material	Aluminum
Design	Solid plate panels
Number of panels	60
Panel width	0.47 m
Panel height	2 m
Cycles to failure	1.5×10^4

Figure 1 Light Ion Beam Target Development Facility

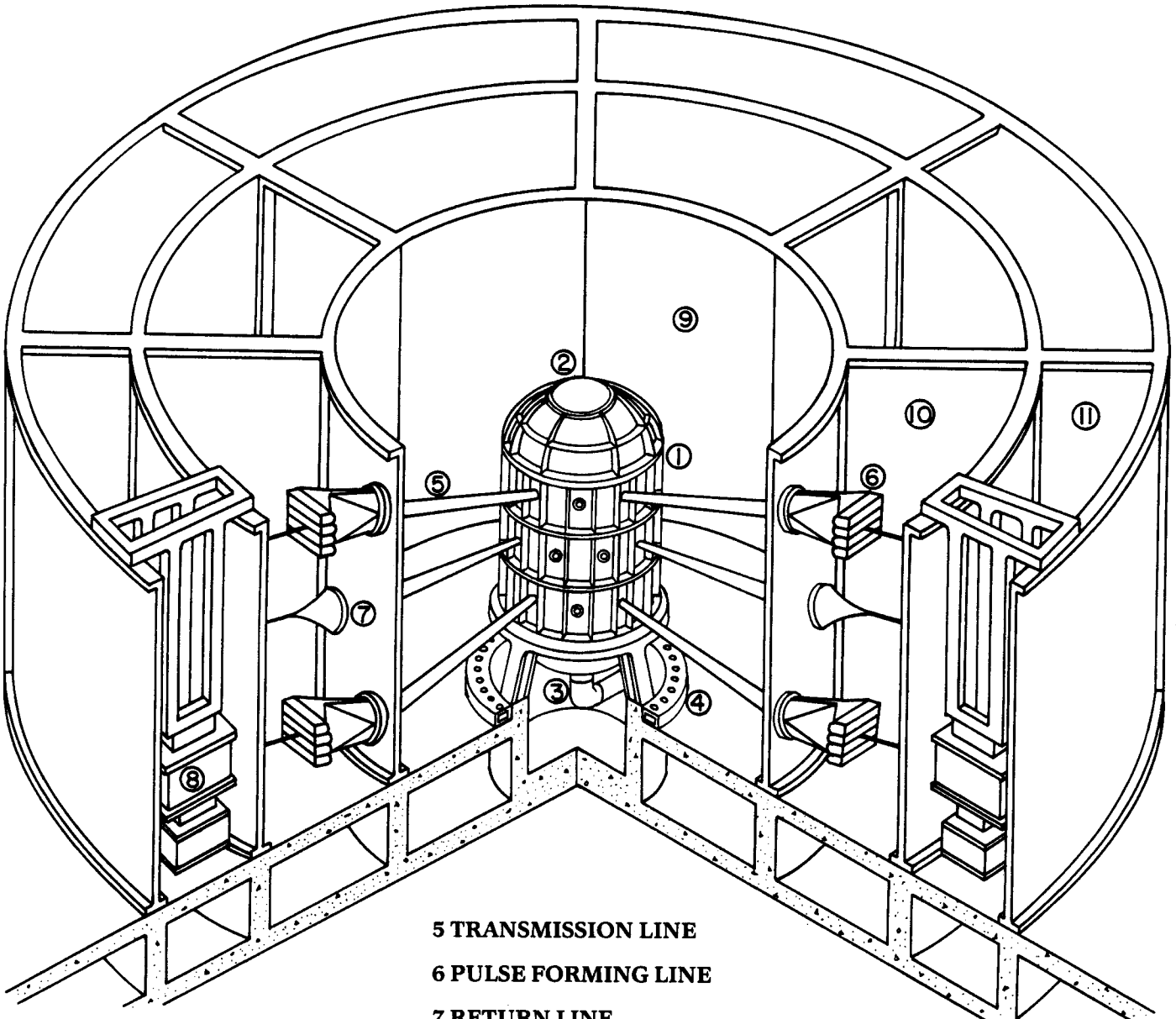

1 TARGET CHAMBER

2 DIAGNOSTIC PORT

3 PURGE LINE

4 AIR BUBBLE PLENUM

5 TRANSMISSION LINE

6 PULSE FORMING LINE

7 RETURN LINE

8 BEAM MARX GENERATOR

9 SHIELDING POOL - WATER

10 PULSE FORMING SECTION - WATER

11 ENERGY STORAGE SECTION - OIL

to the inside. This is shown schematically in Figs. 2 and 3 for two different concepts. For "non-nuclear" testing, the water can be removed completely for access to the magnetically insulated transmission lines and the ion diodes.

The target chamber consists of permanent first wall panels, welded to a permanent structural frame. A closeup view of this design is shown in Fig. 4. The first wall armor plate is about 3 cm thick and the frame consists of a "tubular beam" design to give high stiffness per unit mass. Transmittal of the blast overpressure through the first wall and into the water shield is a concern with this design. We propose that this shock be strongly attenuated in the water by a region containing air bubbles created by the bubble plenum shown around the base of the target chamber. Work on this concept is still in progress.

With the exception of its size, twice the linear dimension of PBFA-II, this facility bears a striking resemblence to swimming pool type fission research reactors. *The new key element of the overall design is the water shield that allows great flexibility in terms of access to the target chamber and surrounding hardware.*

A survey of seven different metal alloys has been done to determine which is most suitable as the first wall material. These alloys are Al 6061, Al 5086, 304 SS, HT-9 ferritic steel, Ti-6V-4Al, Cu-Be C17200, and Cu-Be C17600. The two aluminum alloys are nearly the same. Discussions with Alcoa engineers indicated that Al 6061 is best for rolled sheet and Al 5086 is best for extruded stock. We looked at a common stainless steel alloy, 304 SS, and an advanced ferritic steel alloy, HT-9. A titanium alloy, Ti-6V-4Al, was considered because of its excellent high temperature, high strength characteristics. The two Cu-Be alloys were chosen because of their high thermal conduc-

Fig. 2

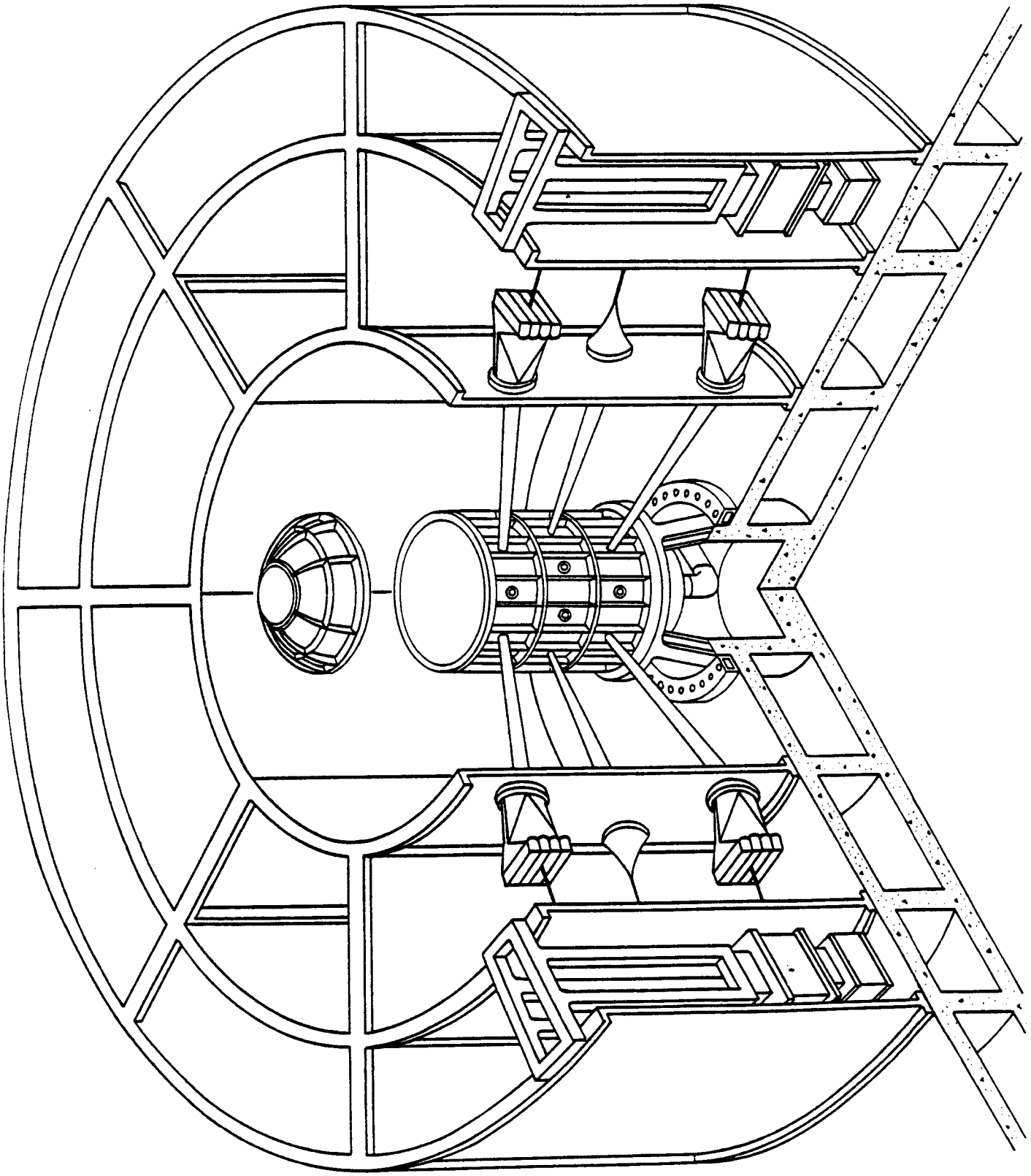

Target development facility target chamber access by removal of vessel head.

Fig. 3

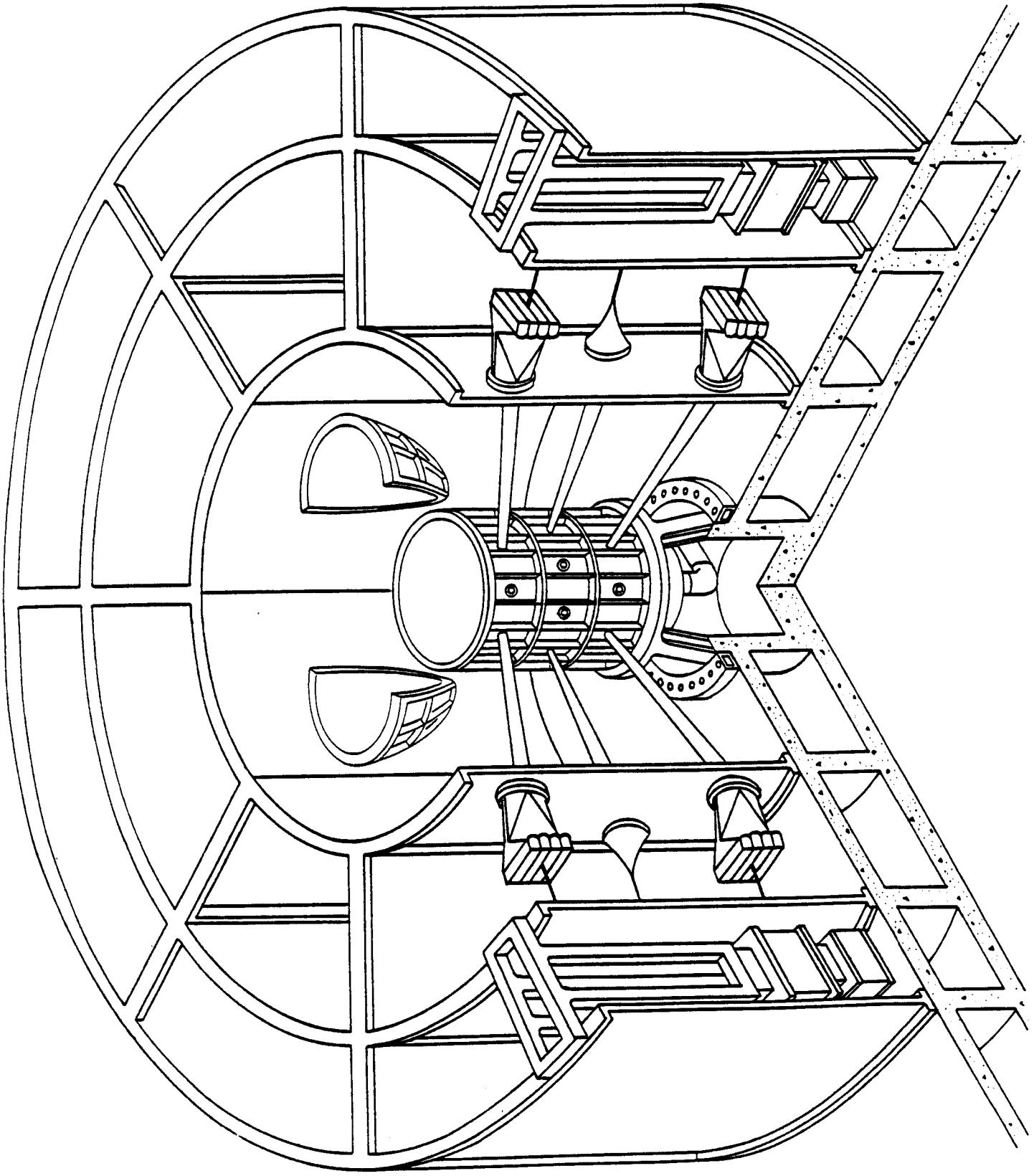

Target development facility target chamber access by opening of clam-shell top.

Fig. 4

CONCEPTUAL FIRST WALL STRUCTURAL SYSTEM

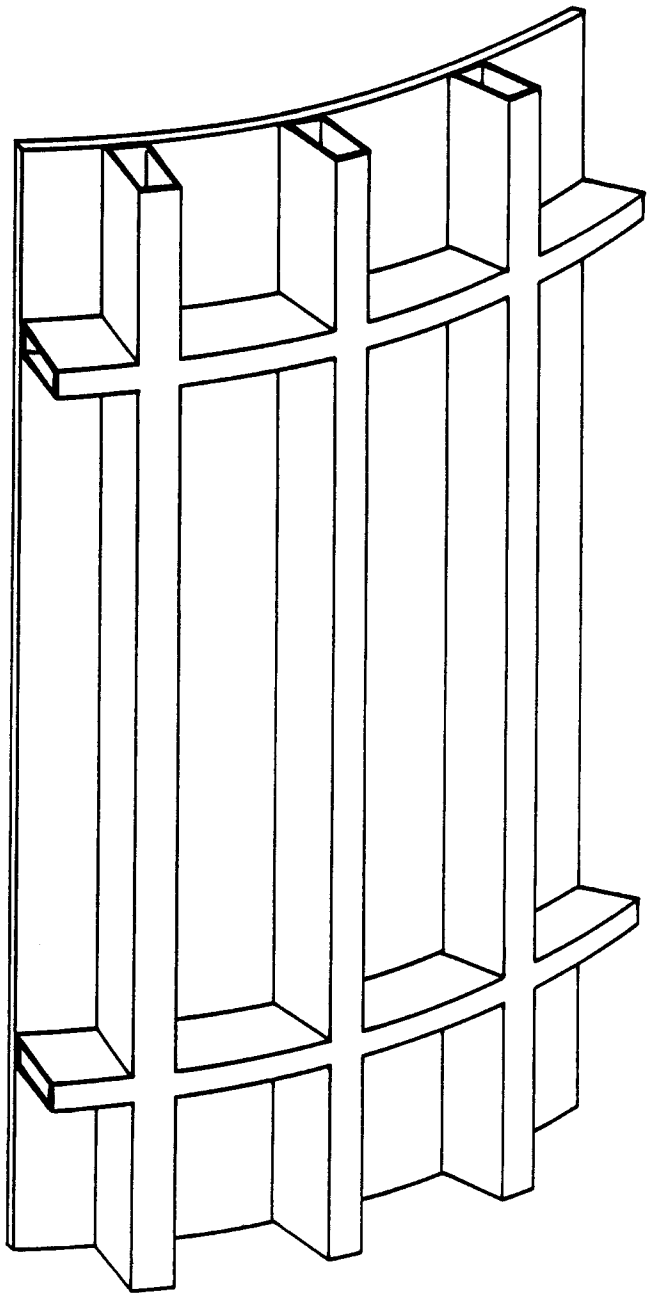

tivities. Physical properties such as specific heat, thermal conductivity, Young's modulus, Poisson's ratio, yield stress, fatigue lifetime, and others were assembled for all of these alloys and in some cases, for differing heat treatments (tempers) as well.

Worst case conditions from fireball calculations were used as input to first wall response calculations for each of these alloys. In other words, the highest overpressure and the highest heat flux obtained from the many fireball calculations were used together to design the first wall even though these conditions did not exist in the same cavity gas calculation. The worst overpressure is shown in Fig. 5 and the worst heat flux is in Fig. 6. This means that we have conservatively spanned the possible conditions within the target chamber. The first wall thicknesses required to meet fatigue lifetime constraints for the different alloys are given in Table II. Corresponding unfabricated costs are given in Table III.

A serious problem in this facility is induced radioactivity in the target chamber and its influence on access to the interior. Table IV shows the radiation dose received at the first wall and 8 meters from it after one week of operation for three of the candidate alloys. (Similar calculations for the other alloys are continuing.) We note that the two steels have lower initial dose levels but these do not decay away very rapidly. The long-lived isotopes responsible for this activity have not saturated after one week of operation and will continue to grow in concentration as the facility is operated. We see in Table V that after one year of operation these steels have very high dose levels even a week after shutdown. On the other hand, the aluminum alloy is initially very hot, but decays to safe levels after one week in both the

Fig. 5

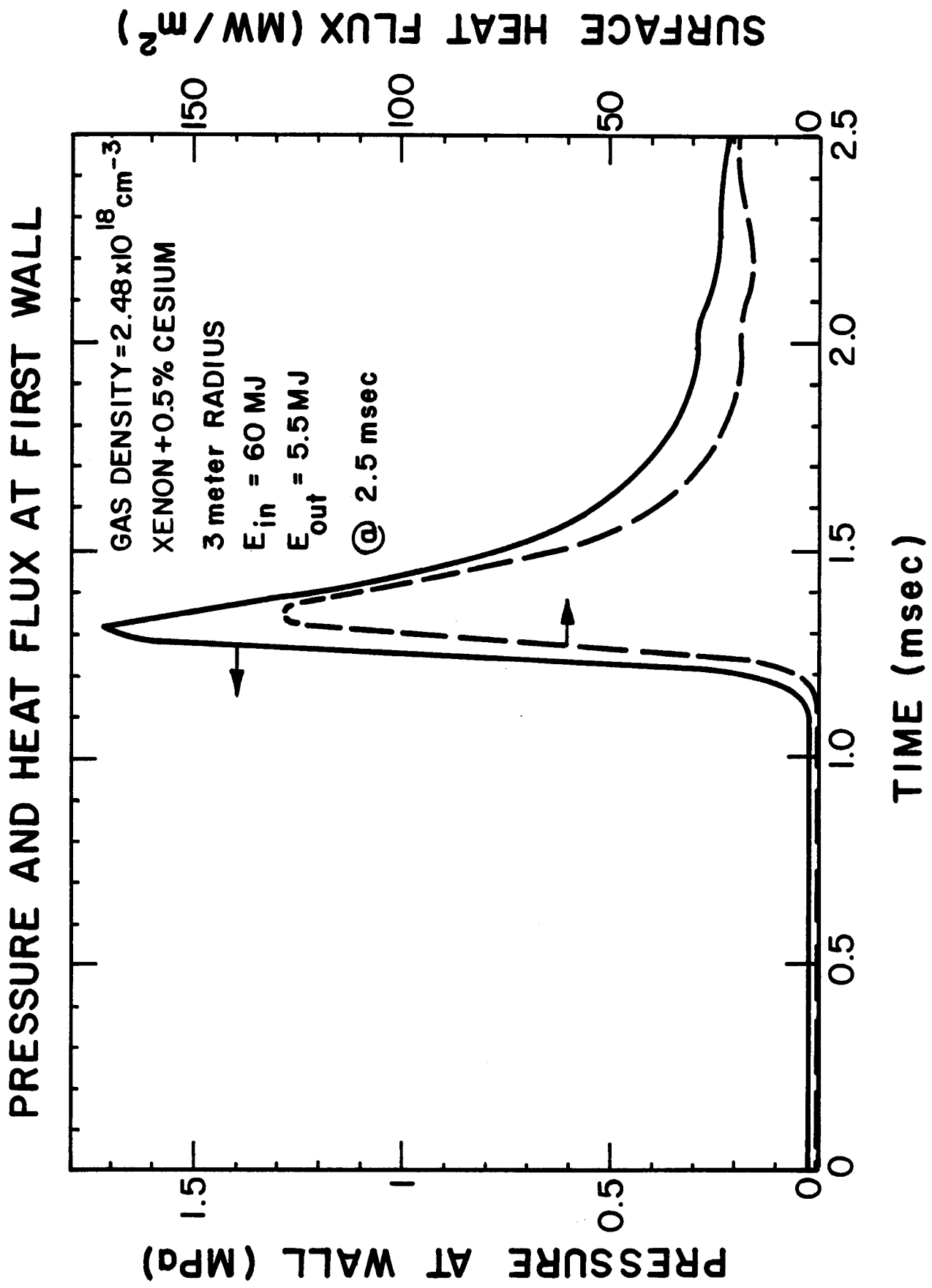
PRESSURE AND HEAT FLUX AT FIRST WALL
GAS DENSITY=2.48x10^18 cm^-3
XENON+0.5% CESIUM
3 meter RADIUS
E_in = 60 MJ
E_out = 5.5 MJ
@ 2.5 msec
PRESSURE AT WALL (MPa)
SURFACE HEAT FLUX (MW/m^2)
TIME (msec)
0
0.5
1.0
1.5
2.0
2.5
50
100
150

Fig. 6

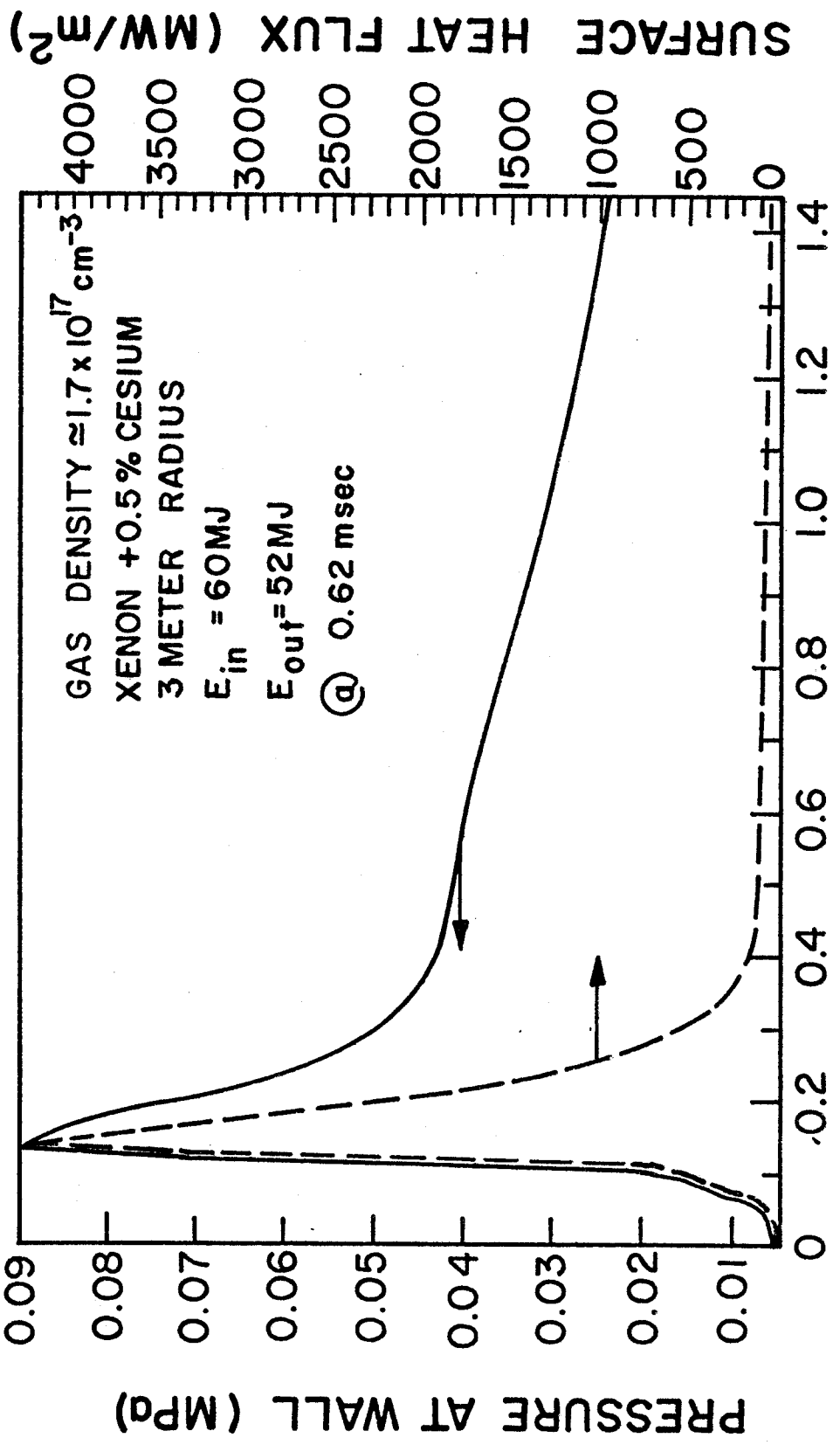

Heat flux and shock overpressure on a 3 meter radius first wall resulting from a 200 MJ microexplosion in a 5 Torr gas of xenon with 0.5% cesium.

Table II. Thickness Required to Avoid Excessive Flexural Stresses

Material	Thickness (cm)
Al 6061	3.0
Al 5086	3.0
304 SS	2.4
HT-9	2.0
Ti-6Al-4V	1.95
Cu-Be C17200	1.1
Cu-Be C17600	2.15

Table III. First Wall Panel Materials Costs (Unfabricated)

Material	Unit Cost ($/kg)	Mass (kg)	Cost ($)
Al 6061	1.8	1.92×10^4	3.5×10^4
Al 5086	1.8	1.89×10^4	3.4×10^4
304 SS	1.26	4.42×10^4	5.56×10^4
HT-9	18.	3.58×10^4	6.44×10^5
Ti-6Al-4V	27.8	1.98×10^4	5.5×10^5
Cu-Be C17200	8.35	2.16×10^4	1.8×10^5
Cu-Be C17600	8.35	4.72×10^4	4.0×10^5

Table IV. Dose Calculations for LIB-TDF

One Week Operating Time @ 16 kW

Time After Shutdown	Dose At First Wall (mr/hr)	Dose At Operating Floor (mr/hr)
	Al 6061	
0	2.1×10^{3}	2.3×10^{2}
1d	264.	28.
1w	0.4	4×10^{-2}
	HT-9	
0	369.	42.8
1d	13.9	1.56
1w	2.58	0.23
	SS 304	
0	373.	43.3
1d	5.8	0.66
1w	3.6	0.42

Table V. Dose Calculations for LIB-TDF

One Year Operating Time @ 16 kW

Time After Shutdown	Dose At First Wall (mr/hr)	Dose At Operating Floor (mr/hr)
	Al 6061	
0	2.1×10^3	230
1d	2.6×10^2	28
1w	1.65	0.18
	HT-9	
0	489	55
1d	114	13
1w	101	11
	SS 304	
0	481	54
1d	109	12
1w	105	12

one week and one year operating scenario. This has significant ramifications for hands-on access to the target chamber.

Our analysis of the first wall panel response is the same as reported previously and will not be repeated here. The analysis of the supporting structural frame is new and deserves some attention. Here again a very conservative approach has been taken. (Improvements to this approach are currently underway). It is assumed that all of the load on the first wall panels is carried as a distributed load by the frame that supports them. This is shown schematically in Fig. 7. A modal analysis for the rib and stringer elements of the frame, similar in spirit to that used for the panels, has been done to compute the deflections, stresses, and vibrational frequencies of the frame. This has been done for six of the candidate alloys thus far.

With this information we can compute the dimensions of the frame elements that are necessary to carry the load. This has been done for aluminum tubular components and Fig. 4 shows such a design to scale.

A qualitative summary of the preceding analysis is given in Table VI. *From this we can conclude that aluminum is a very attractive candidate for the structural material in the first wall and frame of the LIB-TDF.* A combination of acceptable mechanical properties, low induced radioactivity, and low cost lead us to this conclusion. The major problem with aluminum is its incompatibility with sodium or cesium in the cavity gas. This leads to the suggestion that N_2 or NH_3 be investigated as the cavity gas for the TDF.

In the area of cavity gas response we have made several advances. Calculations using the FIRE code have been done for cavity gas pressures ranging from 5 to 70 torr and these have been compared with previous calculations at 50 torr. Table VII shows this comparison. As expected, at lower gas

Fig. 7

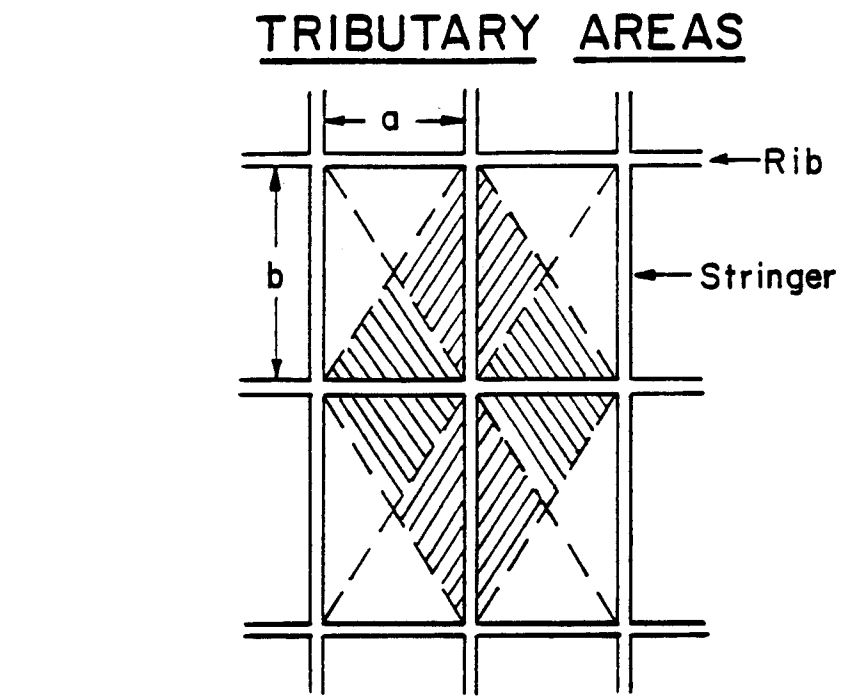
TRIBUTARY AREAS
a
b
Rib
Stringer

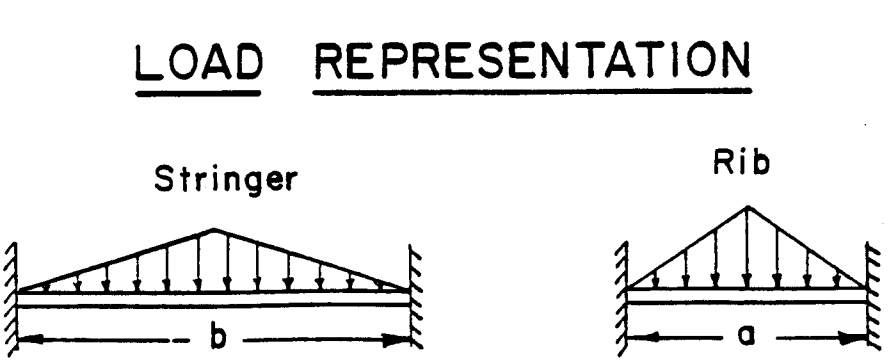
LOAD REPRESENTATION
Stringer
b
Rib
a

Table VI. Qualitative Summary of Materials Properties

Metal Alloy	Mech. Strength	Thermal Stress	Fabricability	Unfabricated $\frac{\text{cost}}{\text{unit mass}}$	Induced Radioactivity	Compatibility with Cavity Gas Na/Cs	Compatibility with Cavity Gas N_2	T_2 Retention	Compatibility with borated H_2O at Room Temperature
Al 6061 Al 5086	Adequate	Very good	Good	Very low	Low	Bad (NaOH dissolves Al)	Good	Good	Good ?
304 SS	Good	Poor	Good	Very low	High	Good	Good	Good	Good
HT-9	Good	Fair	Adequate	Very low	High	Good	Good	Good	Good
Ti-6Al-4V	Adequate	Poor	Adequate	Very high		Good - Oxide layer makes Ti compatible with almost everything	Good - Oxide layer	Bad	Good
Cu-Be	Adequate	Very Good	Fair	Moderate		Okay - NaCl, NaOH	Bad - with moist NH_3 Good - with dry NH_3	Good	Good

Table VII. Pressure, Heat Flux, and Temperature at First Wall

(200 MJ Explosion, Cavity Radius = 3 m)

Gas (Ambient)	Gas Pressure	Code Version	ΔP_{max} (Overpressure)		Q''_{max} (Heat Flux)		ΔT_{max} (°C) at Wall*
			MPa	Time (msec)	kW/cm^2	Time (msec)	
Argon and 0.2% Sodium	10 Torr	FIRE	0.21	0.31	123	0.184	1244
		X-RAY	0.20	0.33	114	0.183	1203
	20 Torr	FIRE	0.64	0.43	42	0.45	662
		X-RAY	0.61	0.43	42	0.32	675
	50 Torr	FIRE	1.25	0.626	20.5	0.676	294
		X-RAY	1.29	0.613	22.6	0.664	324
	70 Torr	FIRE	1.64	0.67	20.9	0.69	300
Xenon and 0.5% Cesium	5 Torr	X-RAY	0.089	0.136	422	0.136	2901
	10 Torr	FIRE	0.18	0.40	177	0.386	1670
	20 Torr	FIRE	0.69	0.695	92	0.695	809
	50 Torr	FIRE	1.33	1.16	19	1.16	243
	70 Torr	FIRE	1.71	1.32	12.9	1.35	150

*Wall material is HT-9.

pressure, the heat flux at the first wall is greatly enhanced and the mechanical overpressure is reduced. At these low pressures the high heat flux melts a very thin layer of material on the surface of the wall for all of the candidate materials. Our analysis to date shows that this will not pose any problem to the structural integrity of the wall.

The FIRE code has been substantially modified to include new options. The treatment of the radiative transfer can now be done using a separate "color temperature" to compute opacities that is not necessarily related to the fourth root of the energy density. This is an attempt to improve the flux limited diffusion treatment of radiation in the free streaming (non-equilibrium) limit. In the past we have started the hydrodynamic simulations using a predetermined, hot, isothermal sphere, at the center of a cold surrounding cavity gas. The FIRE code has been extended to start with a uniform cold gas and attenuate target x-rays, modeled as a point source, using tabulated photoelectric cross sections from the "Biggs tables" from Sandia. The code then determines the temperature distribution in the gas due to this x-ray deposition and uses this as its initial condition. Furthermore, target ions can be slowed down in the gas and the hydrodynamic response of the gas to this slowing down is dynamically computed. Hence we can see that under some circumstances, the ions can sweep gas out of the center of the cavity. This is demonstrated by comparing the R-t plots in Figs. 8 and 9 for gas densities of 5 torr and 0.05 torr. The ion slowing down is treated using analytic fits and tabulated input parameters derived from detailed slowing down calculations using the Brice model from Sandia. This new version of FIRE is fully documented.

Fig. 8

The position of the Lagrangian zones as a function of time for a density corresponding to 5 torr (0°C).

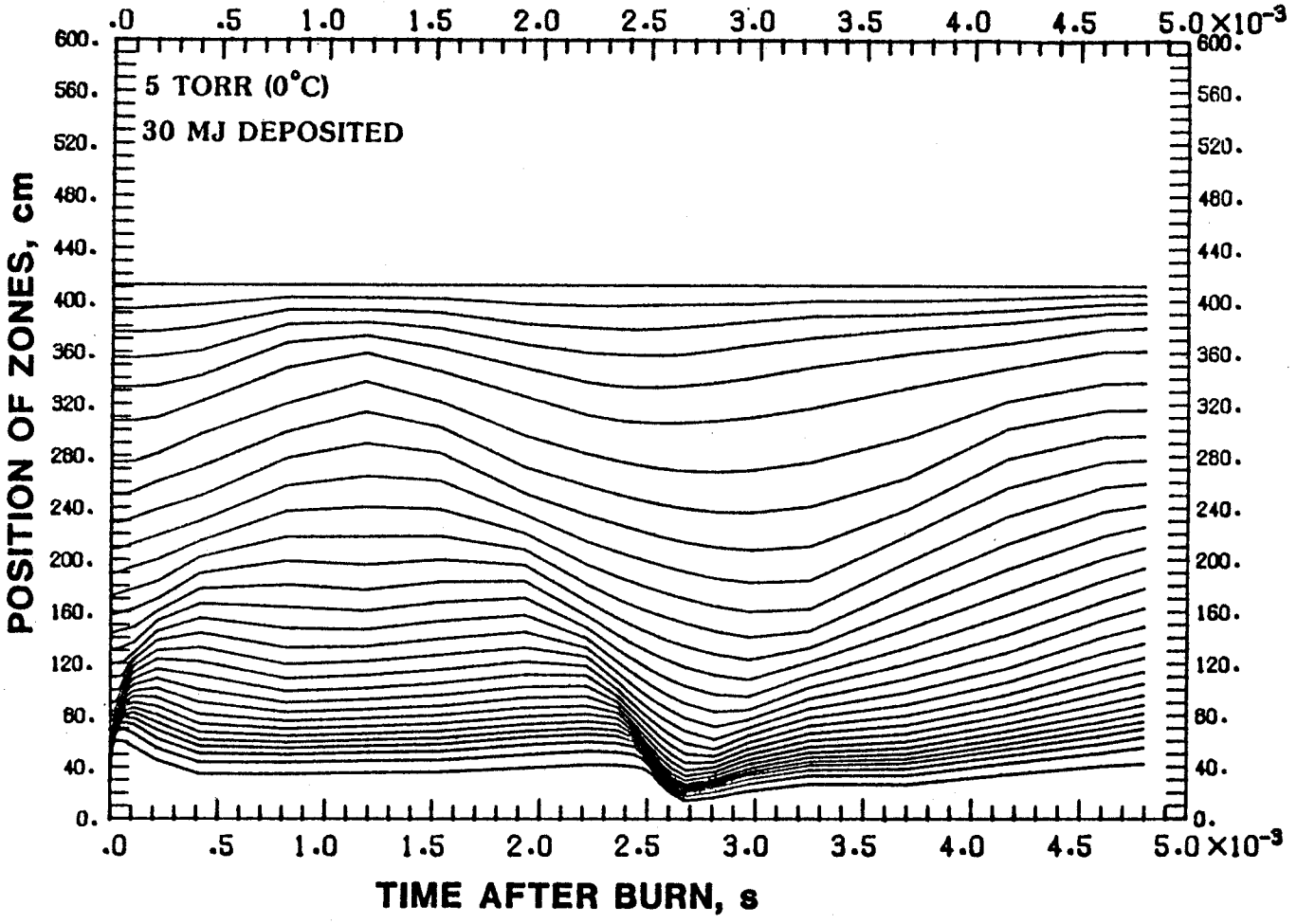

Fig. 9

The position of the Lagrangian zones as a function of time for a density corresponding to 0.05 torr (0°C).

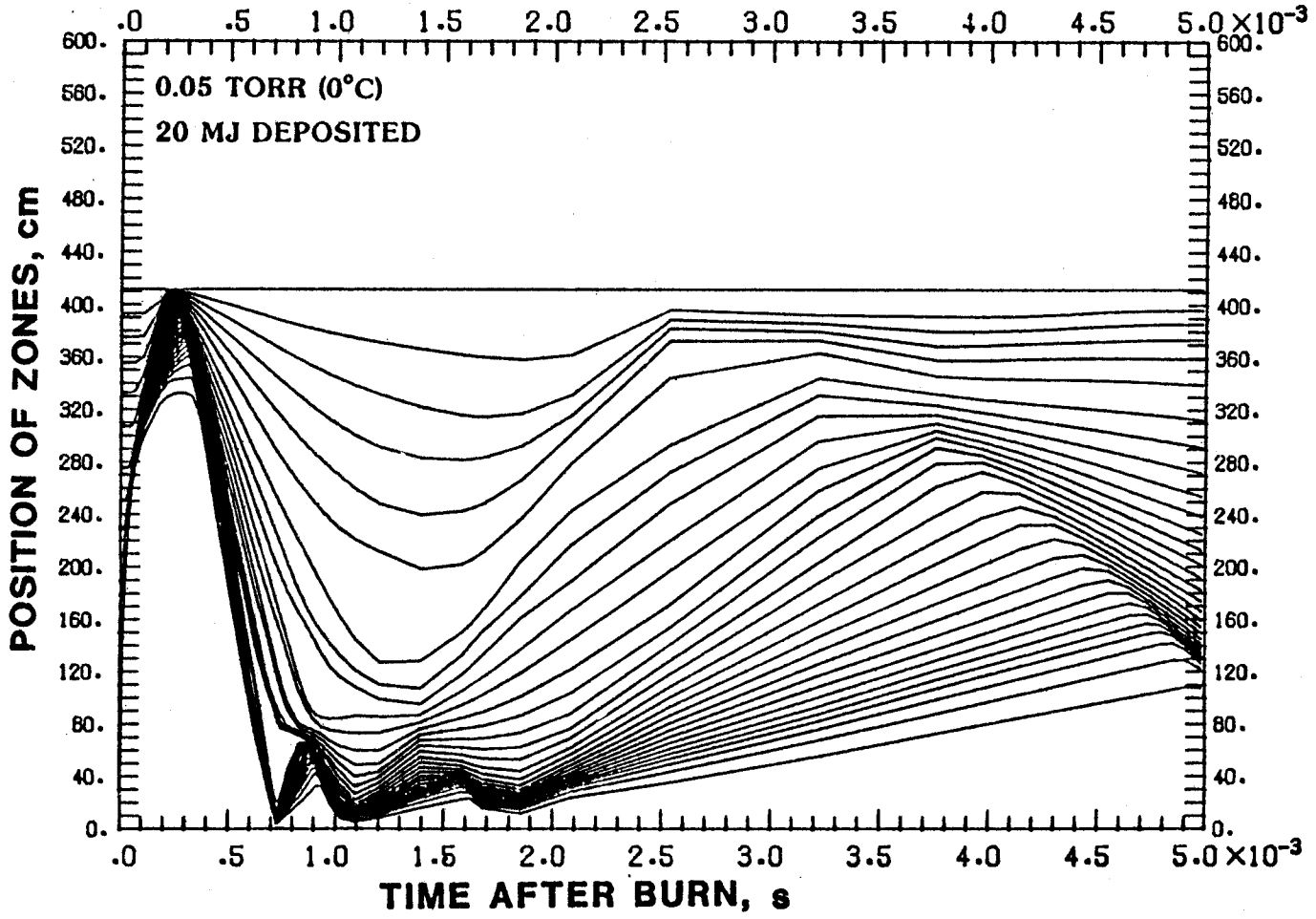

We have made an initial investigation of the possibility of fireball energy preferentially streaming down the plasma channels used for ion propagation. This is shown schematically in Fig. 10. This problem has been modeled using the one-dimensional FIRE code. The code was run using cylindrical symmetry to estimate the radial radiation conduction out of the hot channel into the surrounding cold gas. These results were used to determine a phenomenological radial heat loss term. This term was added to the code's finite difference equations and the code was then run in axial geometry to compute the propagation of the fireball energy down the channel to the diode. The preliminary result is shown in Fig. 11. *It appears that much of the initial fireball energy is "bled away" by the channels when the fireball is at a small radius. However, this energy is dissipated in the channels before reaching the diodes so that the energy density experienced by the diodes is not substantially different than that which we computed using simple spherical fireball models with no channel effects.*

In conclusion, we have undertaken investigations over the past seven months that were aimed at fulfilling the Statement of Work. We believe that we have succeeded in accomplishing this. We now have an integrated first wall and structural frame. This system has been designed to withstand 1.5×10^4 full power shots. The design has been done completely for a number of candidate materials. This was made possible by the integrated and versatile computer analysis package that we have previously developed for this purpose. An overall conceptual design of the Target Development Facility has been proposed. This includes a water shield, permanent structural frame and wall panels around the circumference of the target chamber, and a removable diagnostic port and removable head on the top of the target chamber. In combi-

Fig. 10
Schematic representation of heat transfer in plasma channels.

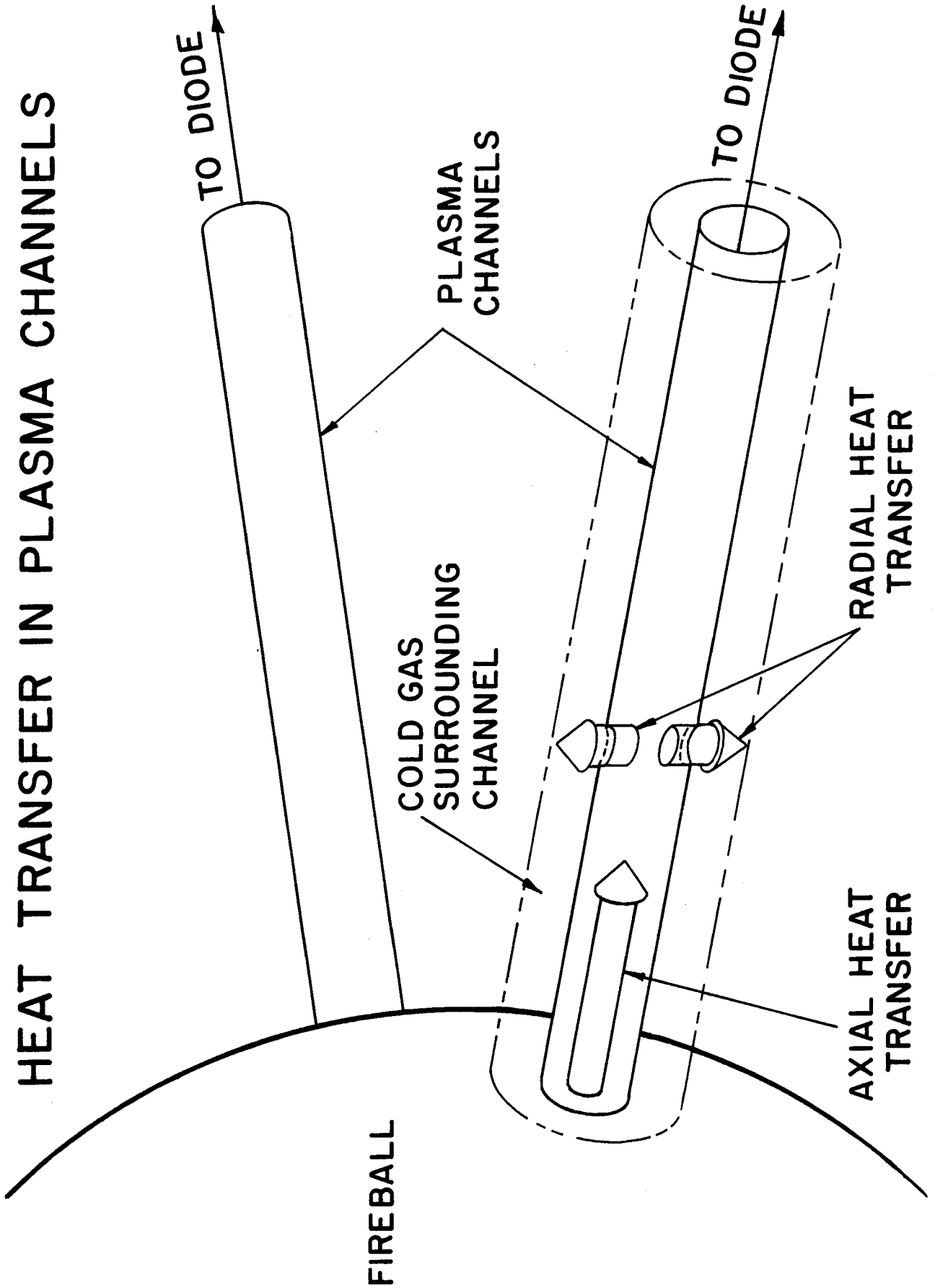

Fig. 11
Schematic representation of preliminary energy balance in plasma channels and density of energy radiated to first surface versus position on surface.

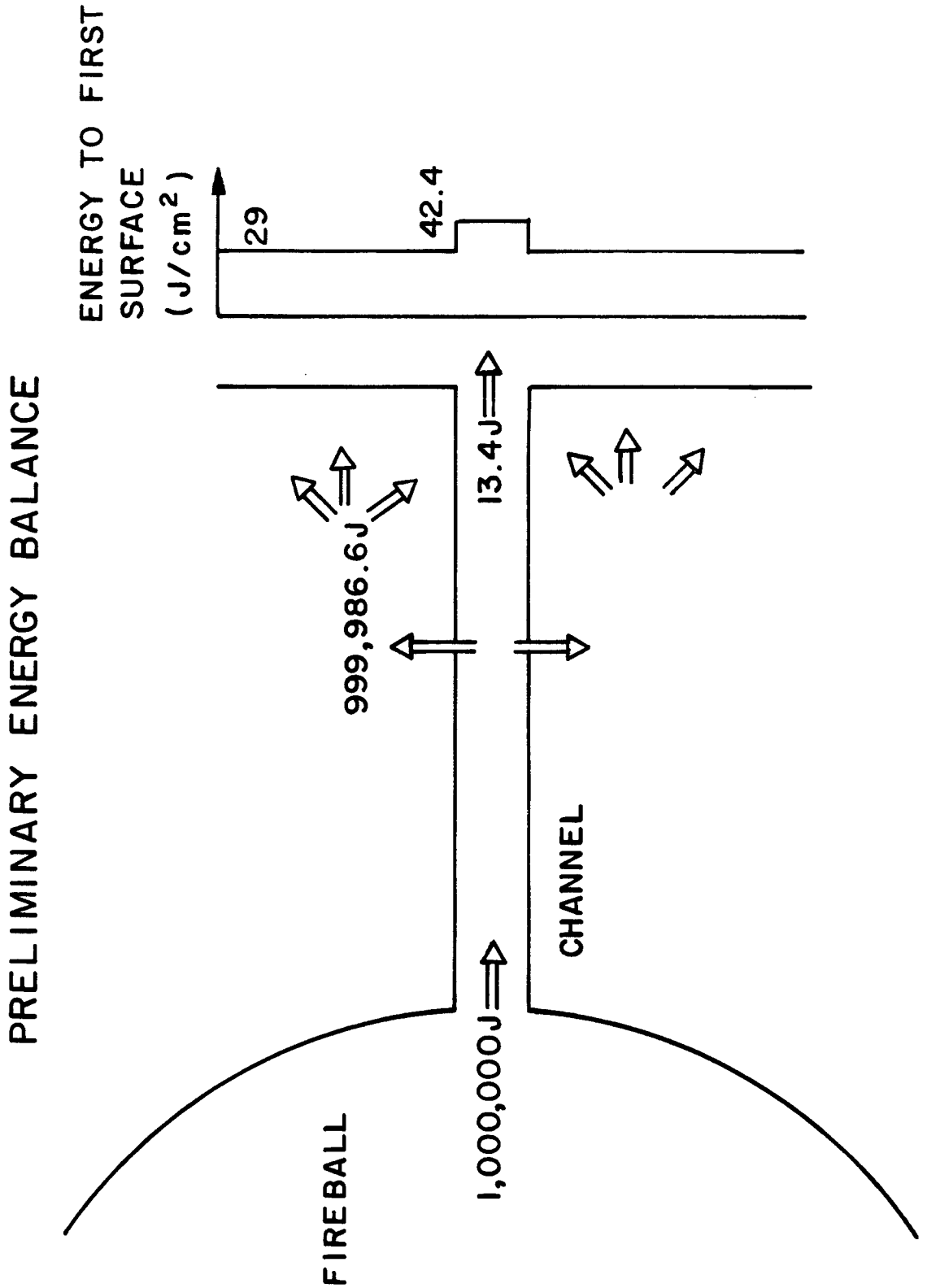

nation these provide excellent radiation shielding and easy access to the target chamber and surrounding hardware such as ion diodes. Neutron activation levels at the first wall have been computed for some of the candidate materials and calculations are currently underway for the others. Results of these calculations now point to aluminum as a very attractive structural material because it allows hands-on maintenance inside the target chamber within one week after shutdown.

2. Choice of First Wall Material in the LIB-TDF

In this section we have reproduced UWFDM-456. It is a discussion of our survey of first wall material choices.

Choice of First Wall Material in the Light Ion Beam Target Development Facility

R.R. Peterson, K.J. Lee, A. White, R. Engelstad,
E.G. Lovell, G.L. Kulcinski, and G.A. Moses

Fusion Engineering Program
Nuclear Engineering Department
University of Wisconsin
Madison, WI 53706

February 1982

UWFDM-456

Abstract

The choice of material for the first wall of the Light Ion Beam Target Development Facility is discussed. Materials considered are Al 6061, Al 5086, 304 stainless steel, HT-9 (ferritic steel), Ti-6Al-4V, Cu-Be C17200, and Cu-Be C17600. The thermal response, mechanical response and induced radioactivity in first walls made of each of these materials are calculated. Minimum thicknesses of these walls are determined and cost estimates are made for the material requirements for each wall. Finally Al 6061 is suggested as the best choice of first wall material.

I. Introduction

First wall design is a critical part of Inertial Confinement Fusion reactor design[1-4] and is also important to any experimental device where repetitive fusion target explosions are to be contained. An important first wall design feature is the choice of material. Important issues in the choice of first wall material include chemical compatibility with coolants and cavity gases, tritium retention, induced radioactivity, mechanical response to shocks and thermal response to heat fluxes. In this paper, these issues are faced for the first wall design in the Light Ion Beam Target Development Facility (TDF)[5] shown in Fig. 1.

In the TDF, fusion targets yielding approximately 200 MJ of energy would be tested roughly 10^4 times during the lifetime of the facility at the rate of 10 shots/day. The target chamber is a cylinder 3 meters in radius and is filled with 5-50 torr of gas. The target explosion generates a blast wave in the cavity gas that transmits a pulsed heat flux and a shock overpressure to the first wall. These effects have been simulated by the computer code FIRE[6] for various densities of argon with a 0.2% impurity of sodium and of xenon with a 0.5% impurity of cesium. The results of these simulations are shown in Table I where the density is expressed as the pressure the gas would have at room temperature. The maximum overpressure, the arrival time of the mechanical shock at the first wall, the maximum heat flux, its arrival time, and the temperature that an HT-9 wall would attain are all shown in Table I. Since there is some uncertainty about what cavity gas pressure would fill the TDF target chamber, the wall should be designed at this time to withstand the largest possible overpressure and the largest feasible heat flux.

Figure 1

Light Ion Beam Target Development Facility

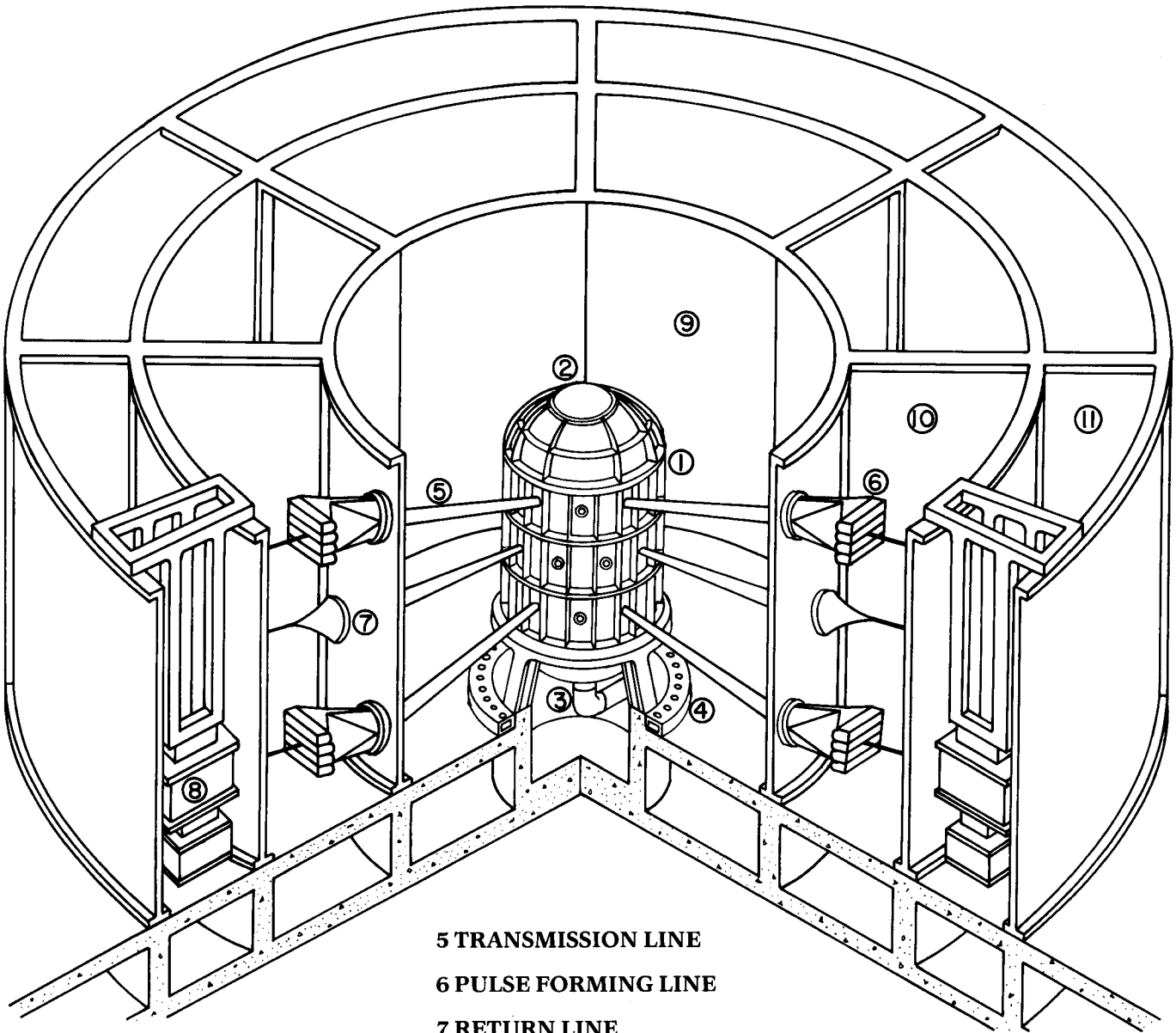

1 TARGET CHAMBER

2 DIAGNOSTIC PORT

3 PURGE LINE

4 AIR BUBBLE PLENUM

5 TRANSMISSION LINE

6 PULSE FORMING LINE

7 RETURN LINE

8 BEAM MARX GENERATOR

9 SHIELDING POOL – WATER

10 PULSE FORMING SECTION – WATER

11 ENERGY STORAGE SECTION – OIL

Table I. Pressure, Heat Flux, and Temperature at First Wall

(200 MJ Explosion, Cavity Radius = 3 m)

Gas (Ambient)	Gas Pressure	Code Version	ΔP_{max} (Overpressure)		Q''_{max} (Heat Flux)		ΔT_{max} (°C) at Wall*
			MPa	Time (msec)	kW/cm^2	Time (msec)	
Argon and 0.2% Sodium	10 Torr	FIRE	0.21	0.31	123	0.184	1244
		X-RAY	0.20	0.33	114	0.183	1203
	20 Torr	FIRE	0.64	0.43	42	0.45	662
		X-RAY	0.61	0.43	42	0.32	675
	50 Torr	FIRE	1.25	0.626	20.5	0.676	294
		X-RAY	1.29	0.613	22.6	0.664	324
	70 Torr	FIRE	1.64	0.67	20.9	0.69	300
Xenon and 0.5% Cesium	5 Torr	X-RAY	0.089	0.136	422	0.136	2901
	10 Torr	FIRE	0.18	0.40	177	0.386	1670
	20 Torr	FIRE	0.69	0.695	92	0.695	809
	50 Torr	FIRE	1.33	1.16	19	1.16	243
	70 Torr	FIRE	1.71	1.32	12.9	1.35	150

*Wall material is HT-9.

Several materials are proposed for the first wall. They are listed in Table II along with some qualitative properties of the materials. Mechanical strength, level of thermal stresses, induced radioactivity and materials costs will be discussed in various sections of the paper. The other properties listed in Table II are fabricability, compatibility with cavity gas, T_2 retention, and compatibility with borated water. Notice that as long as the cavity gas is dry NH_3 or N_2, the only material with any problems is Ti-6Al-4V having a high T_2 retention. If the cavity gas is NH_3, much of the tritium may get bound up in NT_3 and T_2 retention might no longer be a problem. If the cavity gas contains Na or Cs then aluminum is not a good first wall choice.

In Section II, the mechanical and thermal properties of each of these materials is investigated. In Section III we describe mechanical and fatigue response and determine the thickness of each material needed to support the load of the overpressure. In Section IV, the thermal response is investigated and the first wall panel thickness of each material is given. Cost estimates for the first wall materials are made in Section V and the induced radioactivity calculations are described in Section VI. Conclusions and a recommended choice of material are made in Section VII.

II. Thermal and Mechanical Properties

Before any calculations of the first wall mechanical and thermal response can be made, material properties must be identified. The choices of the first wall materials for the TDF cavity are aluminum based alloys (Al 6061 and Al 5086), copper based alloys (Cu-Be C17200 and Cu-Be C17600), titanium alloys (Ti-6Al-4V), and iron based alloys (stainless steel 304 and HT-9). It should be noted that the most important criterion for choosing the candidate materials

Table II. Qualitative Summary of Materials Properties

Metal Alloy	Mech. Strength	Thermal Stress	Fabricability	Unfabricated $\frac{\text{cost}}{\text{unit mass}}$	Induced Radioactivity	Compatibility with Cavity Gas Na/Cs	Compatibility with Cavity Gas N_2	T_2 Retention	Compatibility with Borated H_2O at Room Temperature
Al 6061 Al 5086	Adequate	Very good	Good	Very low	Low	Bad (NaOH dissolves Al)	Good	Good	Good ?
304 SS	Good	Poor	Good	Very low	High	Good	Good	Good	Good
HT-9	Good	Fair	Adequate	Very low	High	Good	Good	Good	Good
Ti-6Al-4V	Adequate	Poor	Adequate	Very high		Good - Oxide layer makes Ti compatible with almost everything	Good - Oxide layer	Bad	Good
Cu-Be	Adequate	Very Good	Fair	Moderate		Okay - NaCl, NaOH	Bad - with moist NH_3 Good - with dry NH_3	Good	Good

is the availability of a qualified metal industry. This criterion is met for all of the candidates.

The thermal (physical) and mechanical properties of the candidate metal alloys are important to the viability of the proposed TDF cavity design. Critical properties include density, heat capacity, thermal conductivity, melting temperature, thermal expansion coefficient, Poisson's ratio, Young's modulus, and tensile yield strength. There is a wide data base for the selected metal alloys with respect to non-fusion environments. Areas such as thermal properties of the candidate metal alloys at room temperature are well known because of their role in aerospace and fission technologies and there is a fair amount of data for moderately elevated temperatures.[7] Most of the data have been obtained from a recently published Metals Handbook[8] and the Structural Alloys Handbook.[9] A recent review of data for HT-9 is found in the "STARFIRE" report.[10] Table III summarizes the data base for the selected metal alloys and contains a quantitative comparison of the seven alloys considered in terms of the thermal and mechanical properties which are the most important to TDF cavity wall design philosophy.

The overall qualitative nature of the thermal properties can be well represented by examining the thermal diffusivity. Aluminum and copper alloys have superior thermal diffusivity compared to that of Ti and Fe based alloys. They allow a much lower temperature gradient at the first wall and will lead eventually to much smaller thermal stresses in the wall. However, their potential disadvantages are connected with their lower melting temperatures. This disadvantage might be corrected by allowing a melting layer at the surfaces facing the incident radiating heat flux. Temperature diffusion calculations indicate that all the candidate metal alloys show much higher maximum

Table III. Thermal and Mechanical Properties of Selected Metal Alloys (Room Temperature)

Metal Alloys	Temper Type	Density (ρ)	Specific Heat (C_p)	Thermal Conductivity (K)	Diffusivity ($K/\rho C_p$)	Melting Point	Thermal Expansion Coefficient (α)	Poisson's Ratio (ν)	Young's Modulus (E)	Yield Strength (σ_y)	$\frac{K(1-\nu)}{\alpha E}$	$\frac{2\sigma_y K(1-\nu)}{\alpha E}$
		g/cm^3	J/g·°K	W/m-°K	cm^2/sec	°C	$10^{-6}/°K$		GPa (KSI)	MPa (KSI)	W/m·MPa	W/m
Al 6061	T6	2.70	0.90	167	0.687	652	23.6	0.33	69 (10,000)	276 (40)	68.7	37920
Al 5086	H34	2.66	0.90	127	0.530	640	23.8	0.33	71 (10,300)	255 (37)	50	25680
304 SS	Annealed	8.0	0.50	16.2	0.0405	1375 ~ 1440	17.2	0.29	193 (28,000)	255 (36.9)	3.4	1750
HT-9		7.75	0.59	29	0.0634	1427 ~ 1482	10.6	0.265	200 (29,000)	442 (64)	10	8870
Ti-6Al-4V	Solution Treated and Aged Bar	4.43	0.67	6.8	0.0222	1660	8.8	0.33	110 (16,000)	1070 (155)	4.7	10030
Cu-Be (C17200)	TB00	8.25	0.42	118	0.340	980	16.7	0.3	128 (18,500)	283 (41)	38.7	21890
Cu-Be (C17600)	TB00	8.75	0.42	230	0.626	1068	16.7	0.3	128 (18,500)	173 (25)	75.5	26050

(Refs.: 1) Metals Handbook, 9th ed., American Society for Metals, Metals Park, Ohio (1979).
2) Structural Alloys Handbook, Battelle's Columbus Laboratories, Columbus, Ohio (1981).
3) Aerospace Structural metals Handbook, Mechanical Properties Data Center, Belfour Stulen, Inc., Traverse City, Michigan (1975, 1981).
4) C.C. Baker et al., "STARFIRE - A Commercial Tokamak Fusion Power Plant Study," Argonne National Laboratory (1980).

temperature differences at the wall than their own melting temperatures. This will be discussed in Section IV.

The mechanical properties of the selected metal alloys are also given in Table III. In terms of mechanical properties, combinations of low thermal expansion coefficients, smaller Young's modulii and high yield (tensile) strengths are desirable. For example, Ti-6Al-4V has a smaller thermal expansion coefficient and larger yield strength than the others. However, it has a much smaller thermal conductivity, which imposes a large thermal stress at the cavity wall as mentioned before. To resolve the paradox of the strongest materials having the worst thermal properties and to qualitatively represent the overall nature of the combined thermal and mechanical properties, the so-called thermal shock parameter is used. This parameter is a measure of the resistance of the metals to thermal stress failure and is defined as

$$P = \frac{2\,\sigma_y K(1 - \nu)}{\alpha E}$$

where: σ_y = yield (tensile) strength

K = thermal conductivity

ν = Poisson's ratio

α = thermal expansion coefficient

E = Young's modulus.

A larger value of P is preferred. It can be seen from Table III that Al and Cu based metal alloys have larger thermal shock parameters compared to that of the Fe and Ti based alloys.

It is well known that most of the metal alloys show wide variations in the thermal and mechanical properties depending on heat treatment, processing

variables and temperatures. Table IV shows the variations of the properties with respect to temper type and temperature. Aluminum based alloys have quite poor values as the temperature increases, while titanium alloys have an increasing value of the thermal shock parameter. Fe based alloys almost remain constant at elevated temperatures. The data base for the copper metal alloys suffers from the lack of related data at high temperatures.

A few important conclusions are drawn from this comparison:

1. The large value of thermal diffusivity for Al and Cu based alloys makes them clearly superior to Fe and Ti based alloys, even though their melting temperatures are relatively lower.
2. Al and Cu based alloys appear to be better choices again with respect to minimizing the thermal stresses due to much higher values of the thermal shock parameter.

III. Mechanical Response of the First Wall

One important constraint on the first wall material and design is that the stresses due to the flexure of wall panels must not exceed either the tensile yield stress or the stress that would lead to fatigue failure during the first wall lifetime. The first wall should last 10^7 flexures if 10^4 target explosions are expected and 10^3 flexures are allowed for each shot. This may be a conservative number but, as is shown in Section IV, it does not lead to excessively thick panels. Since determination of the damping of the flexures is very difficult and depends on the details of the design, it is clearly better to be conservative and choose a large number of flexures per shot. The tensile yield stresses are taken from the values tabulated in Section II. The requirement that the stress remain below the yield stress comes from a desire for the wall to retain its structural integrity. If the

Table IV. Thermal and Mechanical Properties of Selected Metal Alloys

Metal Alloy	Temper Type	Temperature	Thermal Conductivity (K)	Poisson's Ratio ν	Thermal Expansion Coefficient (α)	Young's Modulus (E)	Yield Strength (σ_y)	$\frac{K(1-\nu)}{\alpha E}$	$\frac{2\sigma_y K(1-\nu)}{\alpha E}$
		°C	W/m-°K		10^{-6}/°K	GPa (ksi)	MPa (ksi)	W/m-MPa	W/m
Al 6061	O	25	180	0.33	23.6	69 (10,000)	55 (8)	74	8176
	T4	25	154	0.33	23.6	69 (10,000)	145 (21)	63	18354
	T6	25	167	0.33	23.6	69 (10,000)	276 (40)	69	37920
	T6	300	167	0.33	25.8	38 (5,500)	12.4 (1.8)	114	2837
Al 5086	O	25	127	0.33	23.8	71 (10,300)	117 (17)	50	11800
	H34	25	127	0.33	23.8	71 (10,300)	255 (37)	50	25680
	O	300	127	0.33	25.8	71 (10,300)	29 (4.2)	46	2688

Table IV

Thermal and Mechanical Properties of Selected Metal Alloys - continued

304 SS	Annealed	25	16.2	0.29	17.2	193 (28,000)	255 (36.9)	3.4	1750
	Annealed	500	21.5	0.29	18.2	158 (22,900)	134 (19.4)	5.2	1400
HT-9		25	29	0.265	10.6	200 (29,000)	442 (64)	10	8870
		500	29	0.265	11.8	173 (25,000)	324 (47)	10.5	6796
Ti-6Al-4V	Annealed	25	6.6	0.33	8.8	110 (16,000)	1070 (125)	4.6	7850
	Solution Treated and Aged Bar	25	6.8	0.33	8.8	110 (16,000)	863 (155)	4.7	10030
	Solution Treated and Aged Bar	500	12.0	0.33	10.3	79 (11,500)	621 (90)	9.8	12220

Table IV

Thermal and Mechanical Properties of Selected Metal Alloys - continued

Cu-Be (C17200)	TB00	25	118	0.30	16.7	128 (18,500)	195 ~ 380 (28 ~ 55)	38.7	14950 ~ 29370
	TD01	25	118	0.30	16.7	128 (18,500)	415 ~ 605 (60 ~ 88)	38.7	32040 ~ 46980
	TH04	25	118	0.30	16.7	128 (18,500)	1140~1415 (165~205)	38.7	88110 ~ 109470
Cu-Be (C17600)	TB00	25	230	0.30	16.7	128 (18,500)	140 ~ 205 (20 ~ 30)	75.5	20840 ~ 31260
	H04	25	230	0.30	16.7	128 (18,500)	380 ~ 515 (55 ~ 75)	75.5	57310 ~ 78150
	TH04	25	230	0.30	16.7	128 (18,500)	690 ~ 825 (100~120)	75.7	104200 ~ 125040

wall material is forced to yield repetitively, the lifetime of the panel will be substantially reduced.

The mechanical flexural stresses are calculated for the largest overpressure which could be expected in the TDF cavity gas. This overpressure, which is shown in Fig. 2, was determined by a FIRE code[6] simulation of the response of a 70 torr cavity gas of xenon with a 0.5% impurity of cesium. The greatest reasonable overpressure is used because of the uncertainty in cavity gas response to the target microexplosion. Note that at lower pressures, such as 10 torr, the overpressure is a factor of 10 less. Hence, this is a very conservative choice.

The method of determining the flexural stresses is the same as has been previously reported.[11] This method calculates the dynamic response of the first wall panels by multiplying the static values by a dynamic load factor which is a time-dependent function that includes the effects of material properties and the geometry of the panels. Figures 3 and 4 show the flexural stresses at the inside edge of a panel made of Al 6061 which is 7 cm and 1 cm thick, respectively. In both cases, the dimensions of the panel are 2 meters by 0.47 meters. The panels are assumed to be held fixed on the edges and are solid plates. Notice that the thin panel has a much larger maximum stress and a much lower frequency of oscillation.

The maximum flexural stress has been calculated for several different materials and for plate thicknesses ranging from 1 cm to 7 cm. The dimensions of the panels for all cases are 2 meters by 0.47 meters and they are always solid plates that are held fixed on the edges. In Figs. 5 through 9 the maximum flexural stress has been plotted against plate thickness for Al 6061, 304 stainless steel, HT-9, Ti-6Al-4V, and Cu-Be C17200, respectively. There are

Figure 2 Heat flux and shock overpressure on a 3 meter radius first wall resulting from a 200 MJ microexplosion in a 70 torr gas of xenon with 0.5% cesium.

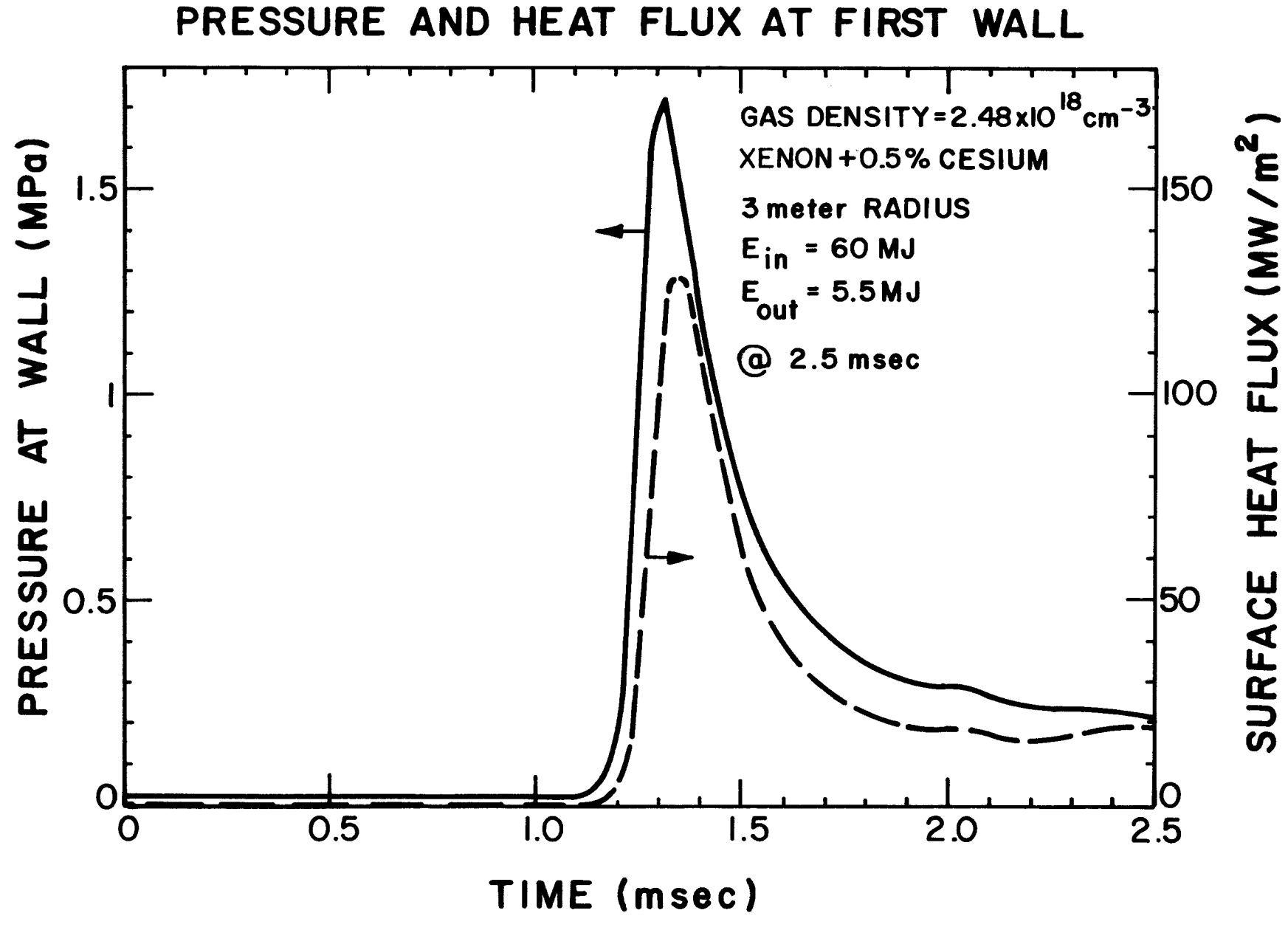

Figure 3 Flexural stress in a 7 cm thick plate of Al 6061 for the pressure pulse shown in Fig. 2.

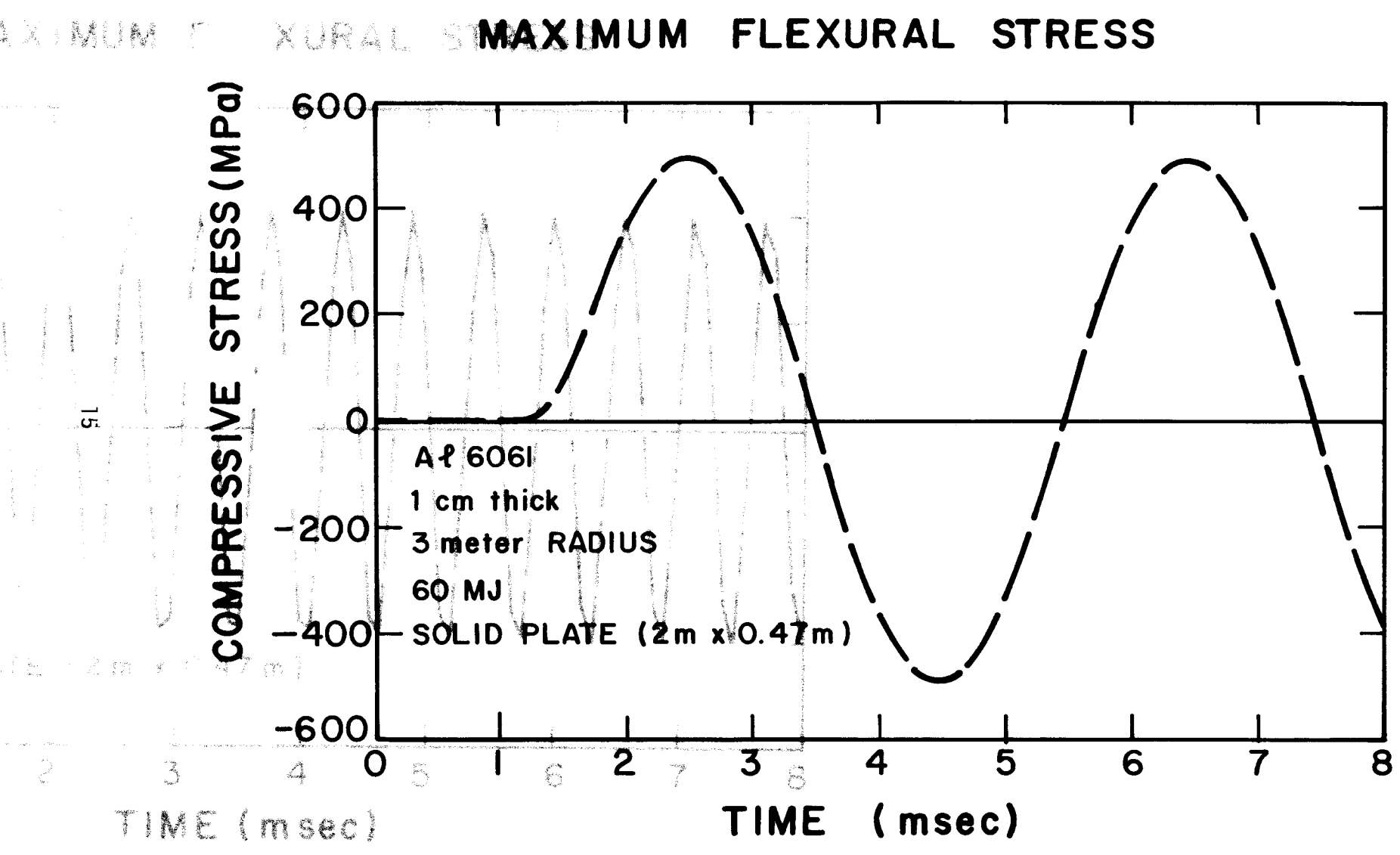

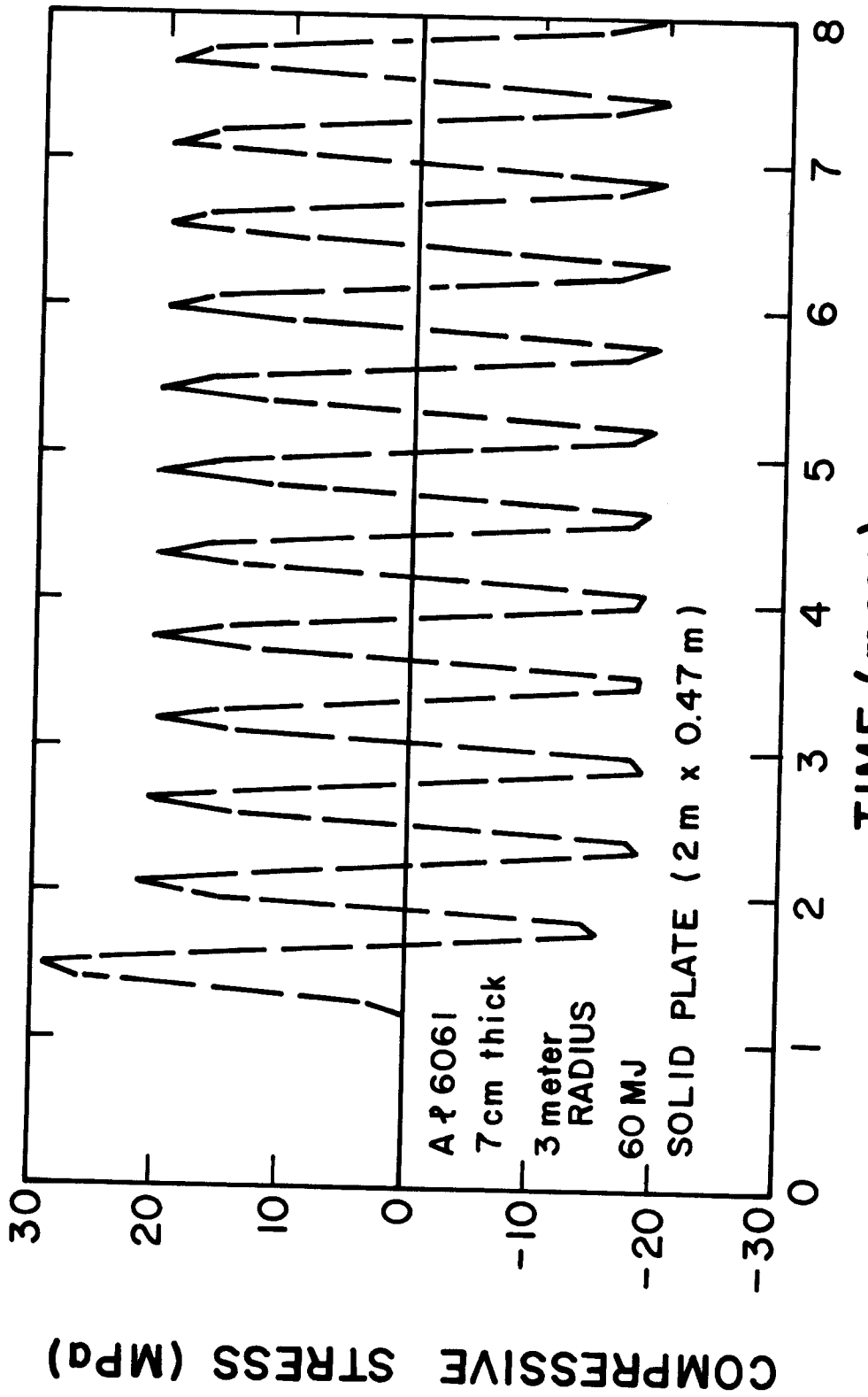

Figure 4 Flexure stress in a 1 cm thick plate of Al 6061 for the pressure pulse shown in Fig. 2.

Fig. 5.

Maximum flexural stresses in a plate of Al 6061 versus plate thickness for the pressure pulse shown in Fig. 2.

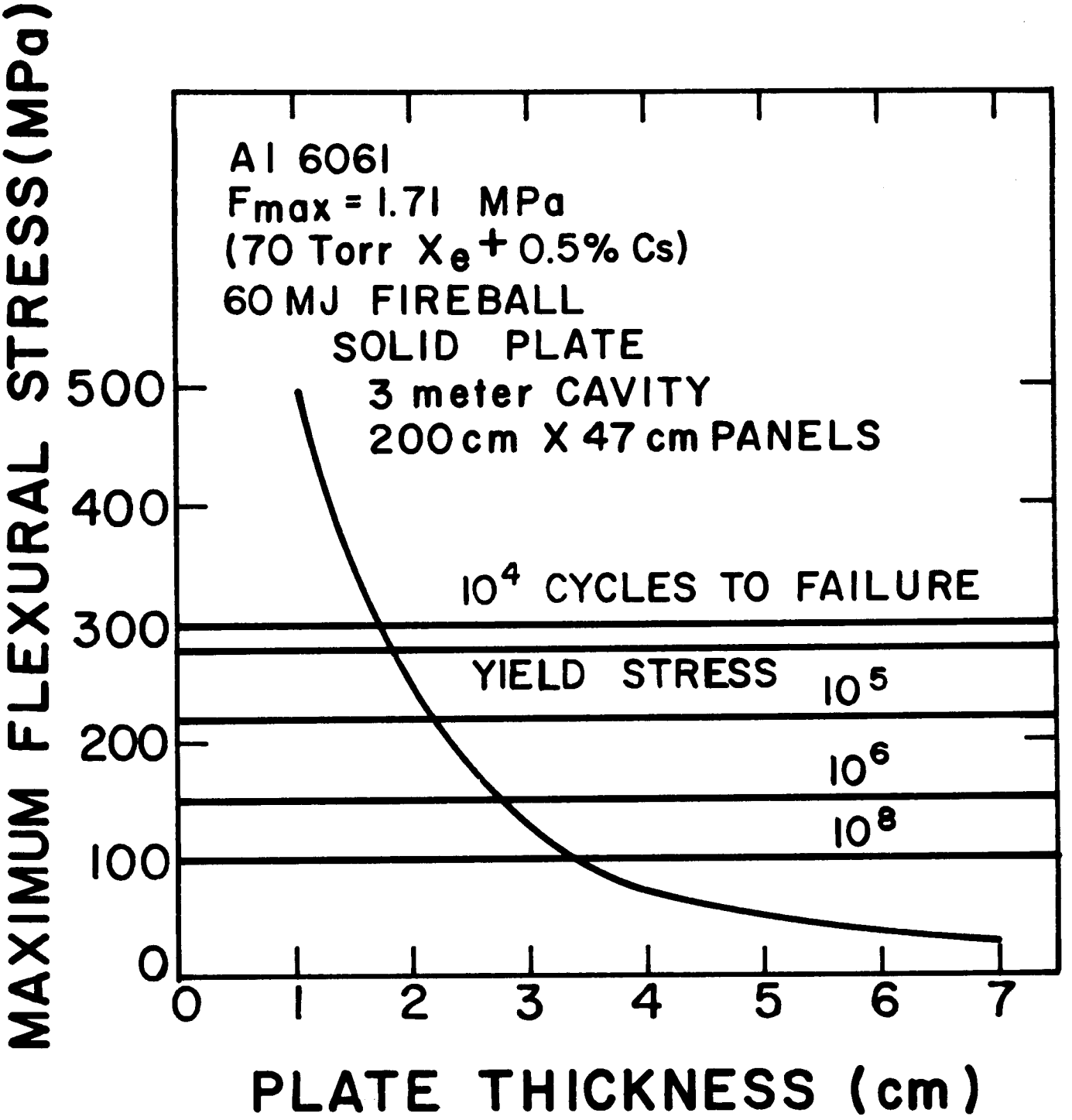

Fig. 6.

Maximum flexural stresses in a plate of 304 stainless steel versus plate thickness for the pressure pulse shown in Fig. 2.

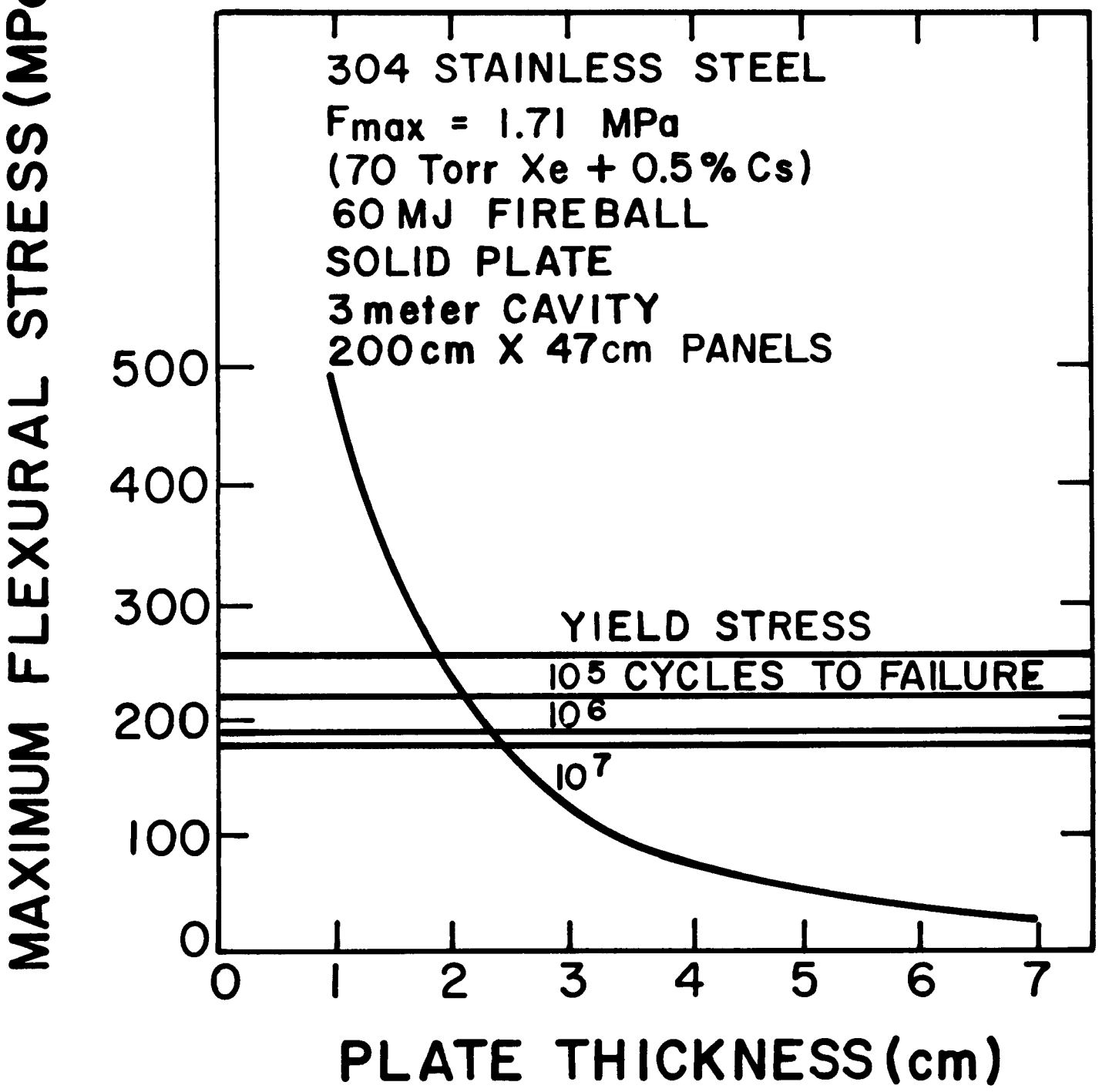

Fig. 7.

Maximum flexural stresses in a plate of HT-9 versus plate thickness for the pressure pulse shown in Fig. 2.

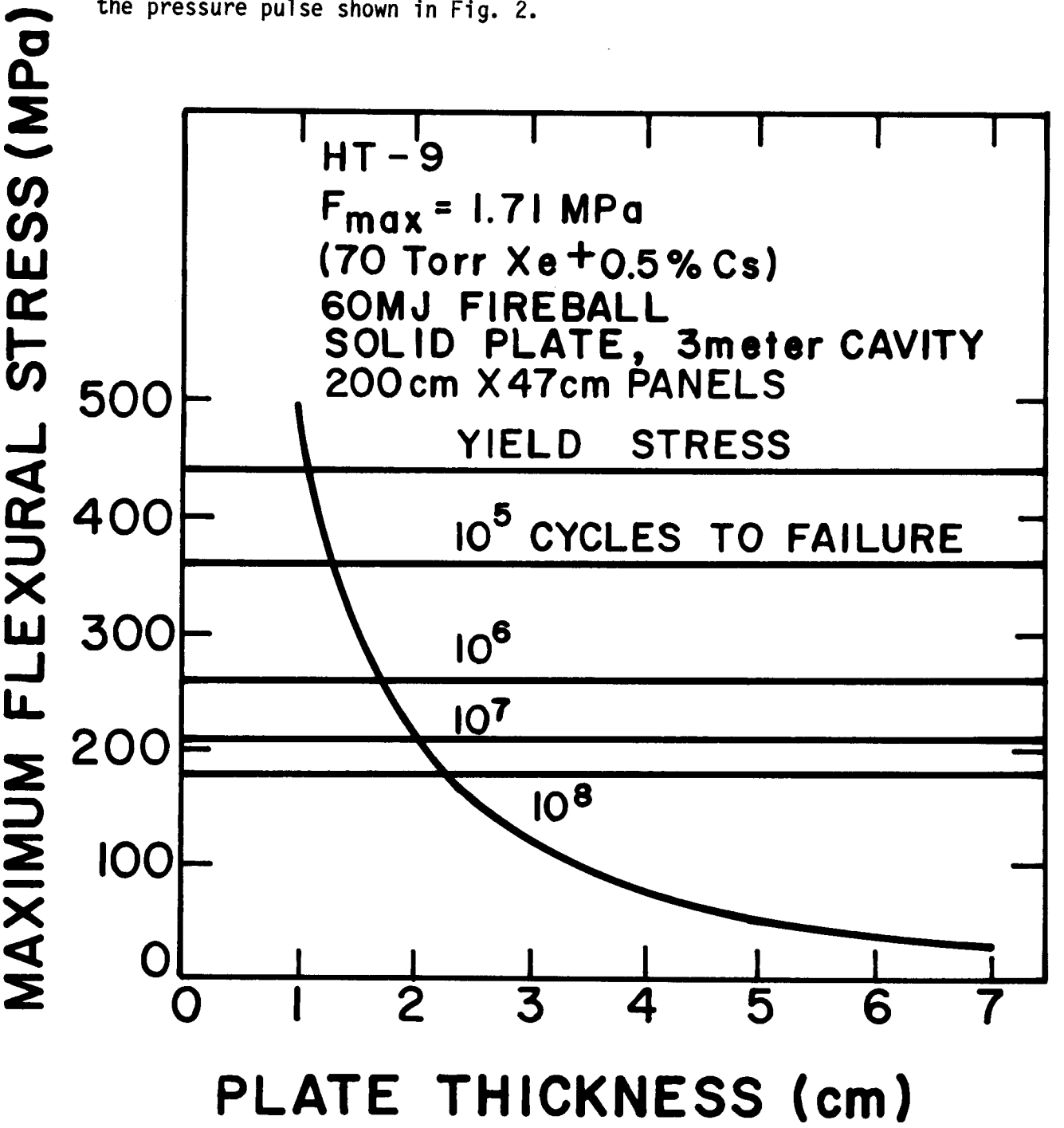

Fig. 8.

Maximum flexural stresses in a plate of Ti-6Al-4V versus plate thickness for the pressure pulse shown in Fig. 2.

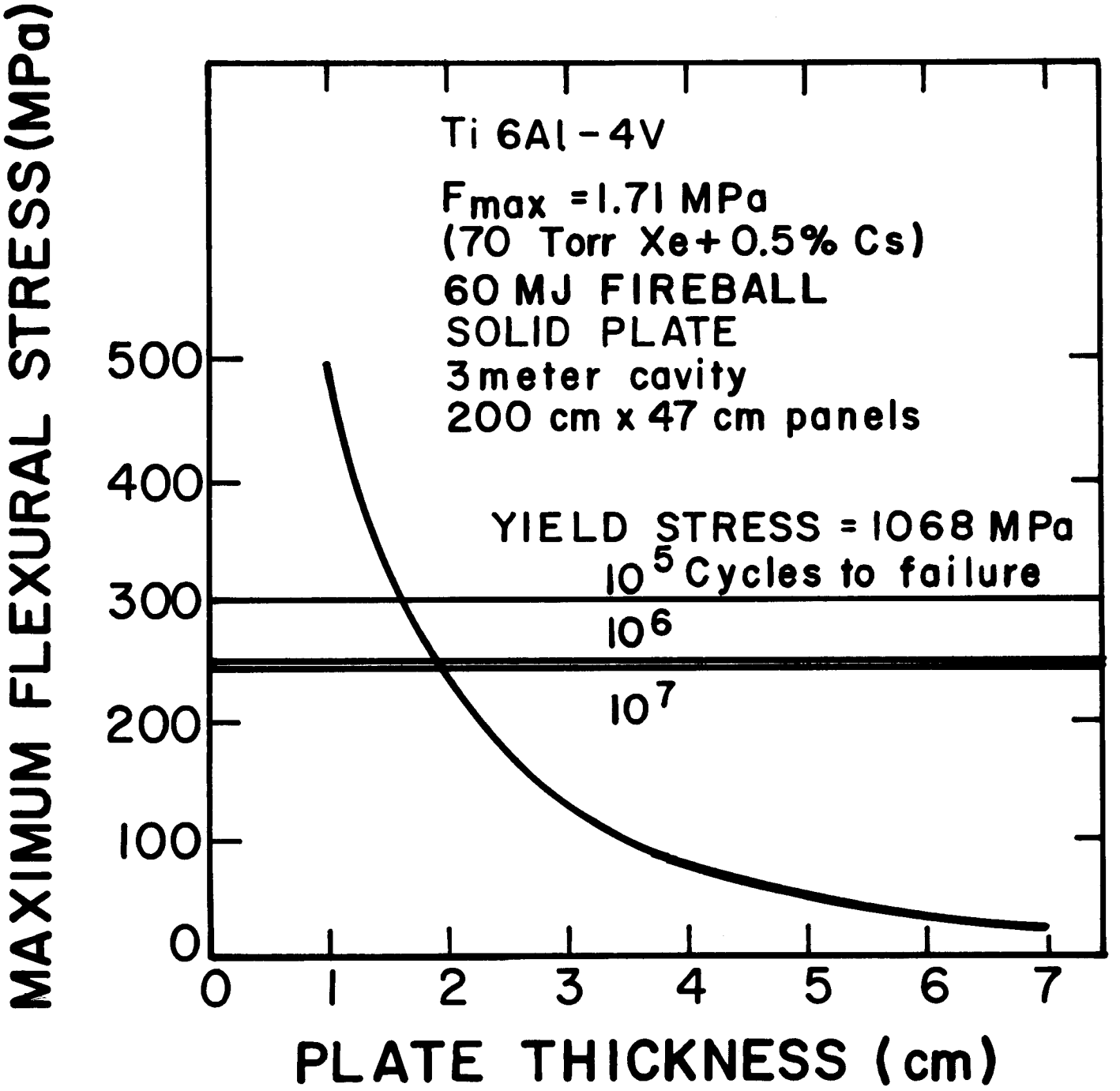

Fig. 9.

Maximum flexural stresses in a plate of Cu-Be C17200 versus plate thickness for the pressure pulse shown in Fig. 2.

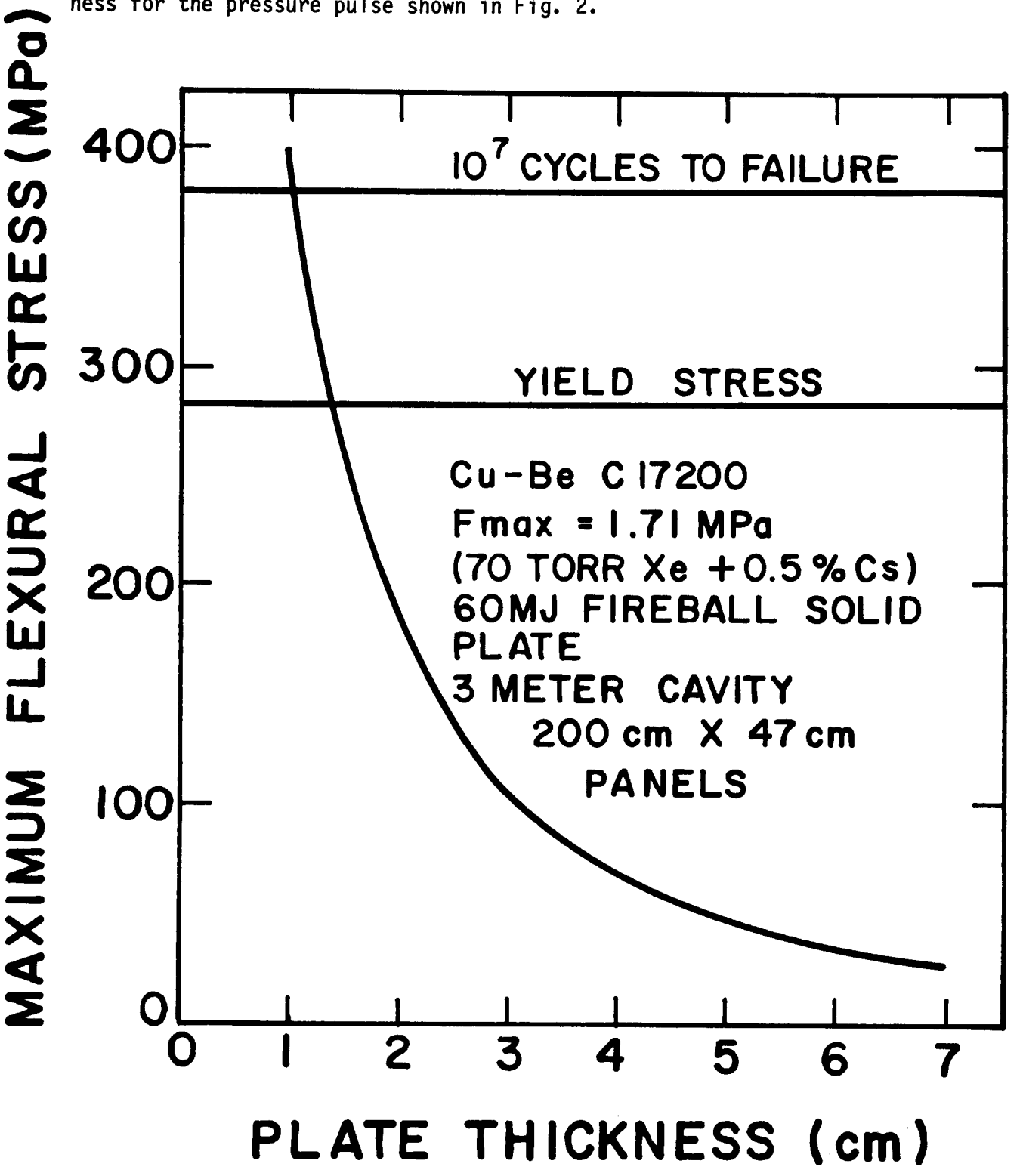

comparable plots for Al 5086 and Cu-Be C17600, but they are very similar to Al 6061 and Cu-Be C17200 and are not shown. Also shown in Figs. 5 through 9 are the stresses corresponding to fatigue failure after a given number of flexures[8] and the tensile yield stresses.

With the results in these figures, the plate thickness required for each material may be determined. The thickness is the maximum of the value corresponding to 10^7 cycles to failure and the value corresponding to the yield stress. Only Cu-Be C17200 and Cu-Be C17600 have their thickness determined by the yield stress. The required thicknesses of all of the materials are given in Table V.

IV. Thermal Response of the First Wall

The second important consideration in first wall design is the thermal response of the wall panels. It is possible that a large fraction of the 60 MJ of non-neutronic target yield may be deposited on the first wall in a fraction of a millisecond. Under such conditions the first wall material may melt or experience large thermal stresses which can cause inelastic deformations or creep. The philosophy used here is to assume the largest possible surface heat flux and analyze the behavior of the innermost layer of the material which undergoes these effects. As long as the effects of heating remain in this layer, e.g., there is no significant growth of cracks, the layer may be treated separately from the remainder of the plate. The load of the shock overpressure is carried by the part of the plate behind the thermally stressed and melted layer and the thickness of the load bearing region is that determined from yield stress and fatigue considerations in Section III.

The heat flux used in the analysis of the thermal response is that which results from a fireball simulation[12] of 60 MJ of non-neutronic target energy

Table V. Thickness Required to Avoid Excessive Flexural Stresses

Material	Thickness (cm)
Al 6061	3.0
Al 5086	3.0
304 SS	2.4
HT-9	2.0
Ti-6Al-4V	1.95
Cu-Be C17200	1.1
Cu-Be C17600	2.15

propagating through a 5 torr xenon gas with a 0.5% impurity of cesium. The heat flux at the first wall of a 3 meter target chamber is shown in Fig. 10. Notice that in this case roughly 90% of the fireball energy is radiated to the first wall in less than a millisecond.

The temperature profile in the first wall is calculated using the heat flux shown in Fig. 10 by using a simple temperature diffusion computer code with constant heat transfer coefficients. An example of this type of calculation for Al 6061 is shown in Fig. 11. The temperature of the first wall is plotted against the distance into the wall for different times. Also shown are the melting temperature of the material, one half of the melting temperature and the temperature causing a 0.1% deformation in the material. A material hotter than one half of the melting temperature may be assumed to creep and any deformation greater than or equal to 0.1% may be taken as inelastic. From plots like Fig. 11, the duration and width of the layer of melted material may be deduced. The duration of the melt layer in Al 6061 is estimated to be 4.7×10^{-4} seconds.

This temperature diffusion code nelgects the heat of fusion and thus overestimates the temperature in the melted layers. A*THERMAL, a more sophisticated temperature diffusion code[13] which includes the effects of heat of fusion has been used to do the same calculation as shown in Fig. 11 and gives the result shown in Fig. 12. Here the surface temperature is plotted against time. Notice that the discontinuity in the heating of the wall surface through the melting temperature is very small, which means that the heat of fusion uses only a small fraction of energy radiated to the wall. Also notice that the film of molten material resolidifies in 4×10^{-4} seconds, which agrees well with 4.7×10^{-4} seconds predicted by the less sophisticated

Fig. 10

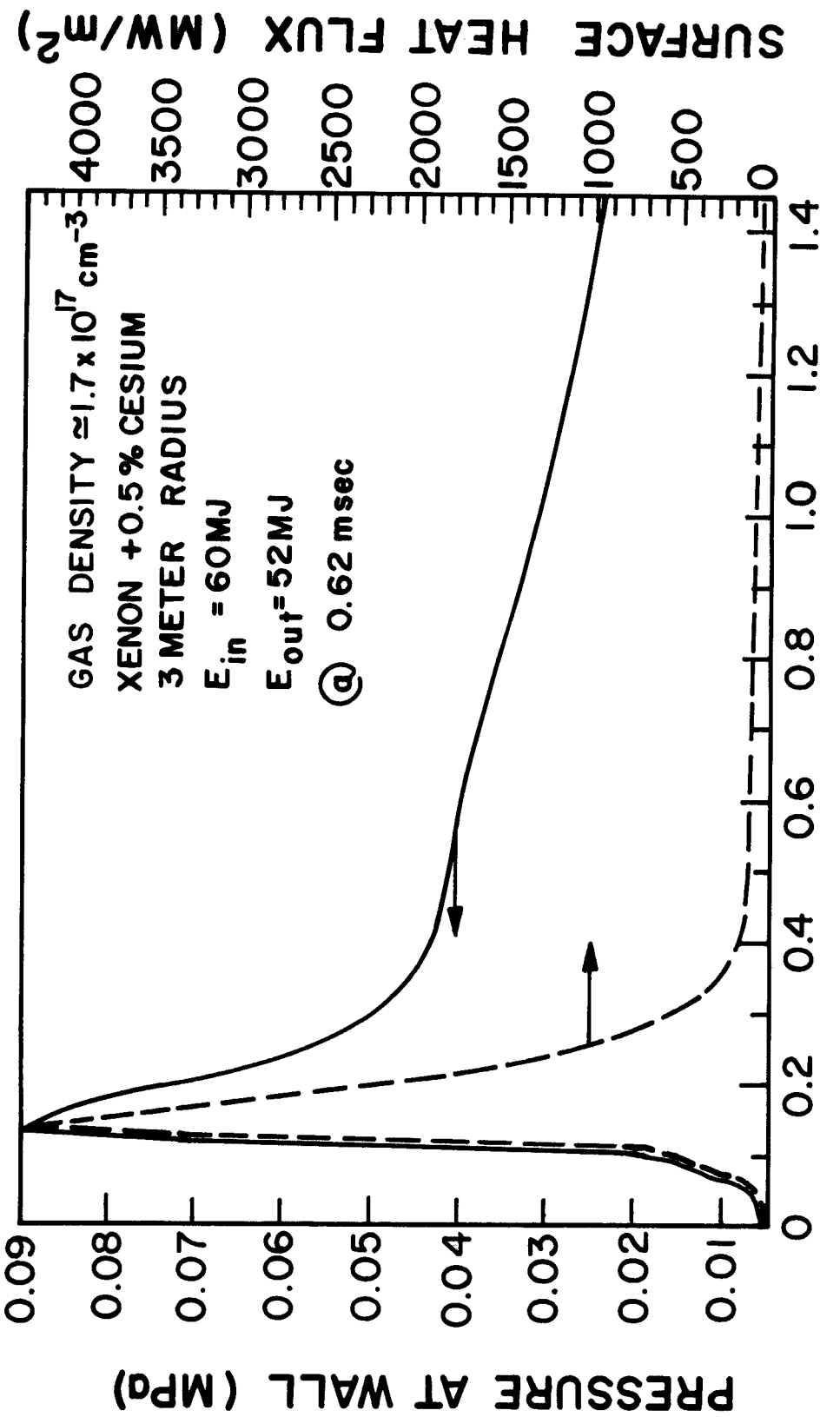

Heat flux and shock overpressure on a 3 meter radius first wall resulting from a 200 MJ microexplosion in a 5 Torr gas of xenon with 0.5% cesium.

Fig. 11

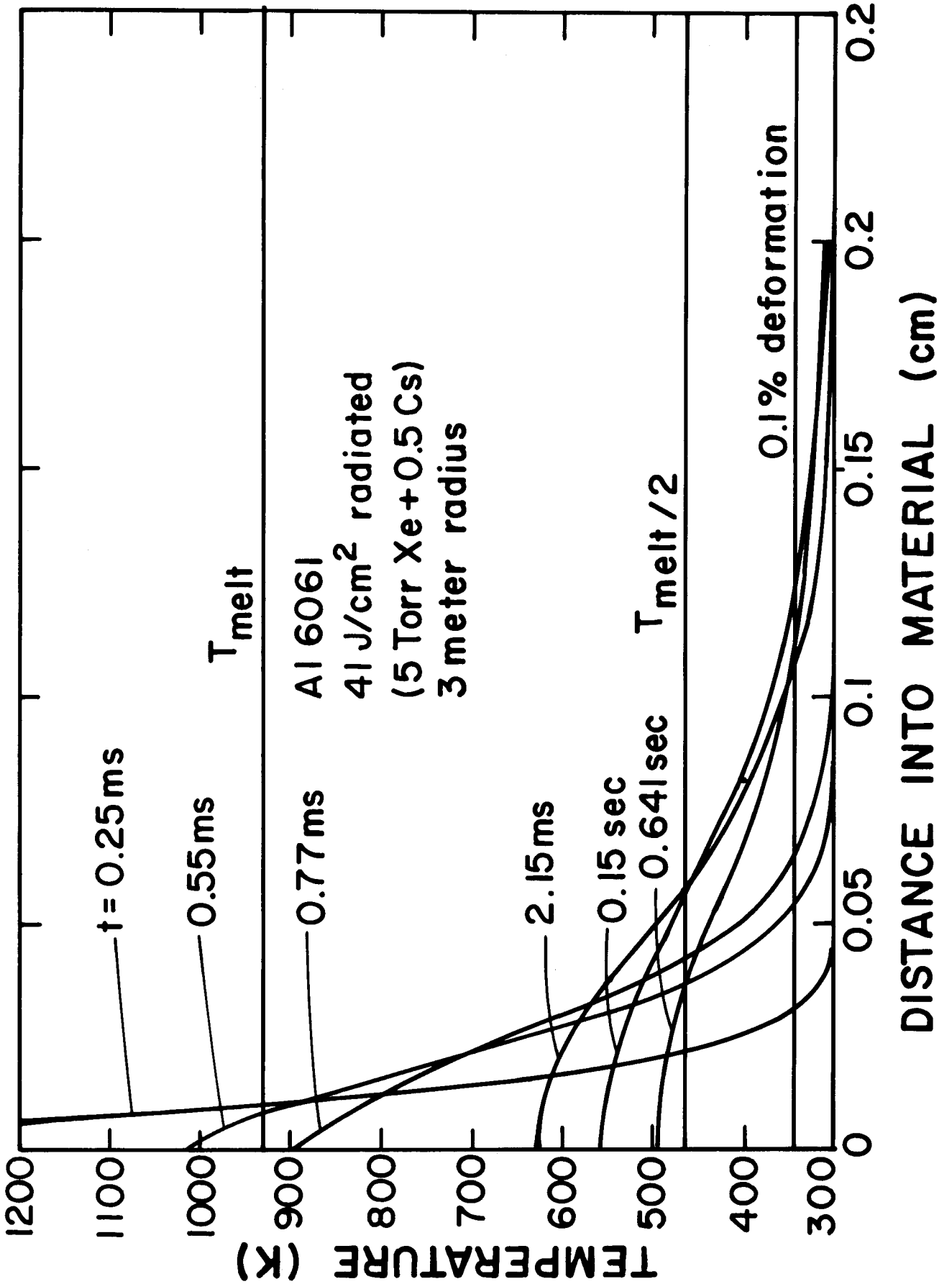

Temperature profiles in an Al 6061 plate versus distance into plate for the heat flux shown in Fig. 10.

Fig. 12

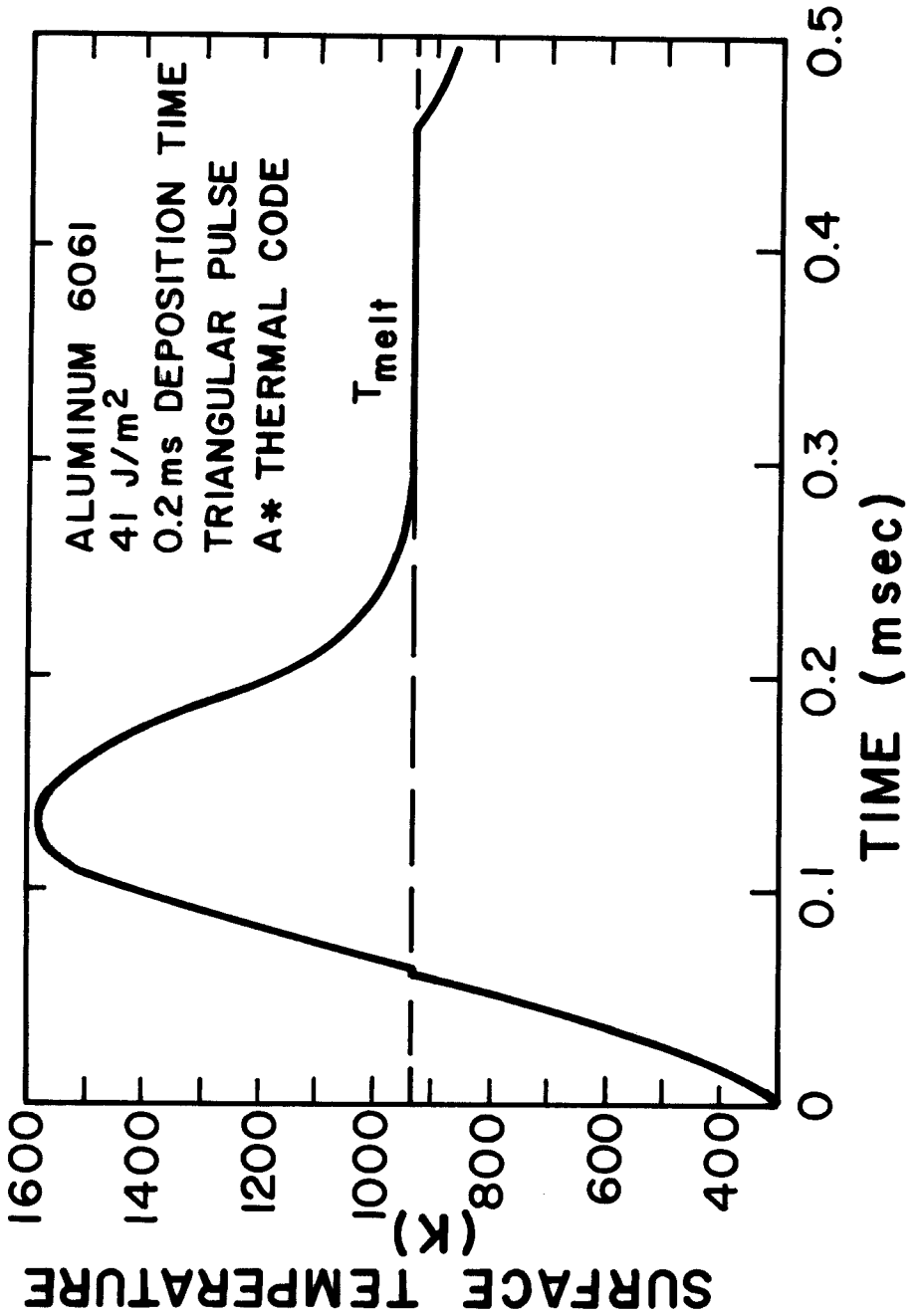

Surface temperature in an Al 6061 plate versus time for the heat flux shown in Fig. 10 as calculated with A*THERMAL.

analysis. This agreement between the two calculations allows the neglect of the heat of fusion in all of the following calculations.

In Figs. 13 through 18 temperature profiles for various times are plotted for Al 5086, 304 stainless steel, HT-9, Ti-6Al-4V, Cu-Be C17200, and Cu-Be C17600, respectively. The calculations leading to these plots have neglected the effects of heat of fusion. The thermal properties of the materials were taken from Table III. It may be noted that the materials with high thermal conductivities, namely the Cu-Be and Al alloys, have low and broad temperature profiles, as one would expect. Conversely, those materials with low thermal conductivities (304 stainless steel, HT-9, and Ti-6Al-4V) have high and narrow temperature profiles. Also shown in these plots are the melting temperatures, one half of that temperature, and the temperature needed for 0.1% deformation.

Using the temperature profiles and the melting temperatures and temperatures for 0.1% deformation shown in Figs. 11 and 13 through 18, the duration and thickness of the layers of melted material and the thicknesses of the inelastically deformed regions can be determined. The purpose of this is to find the thickness of that region which is not able to support the load of the shock overpressure because of the combined effects of melting and thermal stresses. The thicknesses of the layers dedicated to bearing the effects of the thermal pulse are given for each material in Table VI. Also given in Table VI are the thicknesses needed to support the mechanical load and the total thickness for each material. The material which requires the thinnest plate is Cu-Be C17200 because it has a high thermal conductivity, a moderate melting temperature, a moderate Young's modulus and good fatigue resistance. The material which requires the thickest plate is Al 6061 because, even though it has a high thermal conductivity, the melting temperature is low so that it

Fig. 13

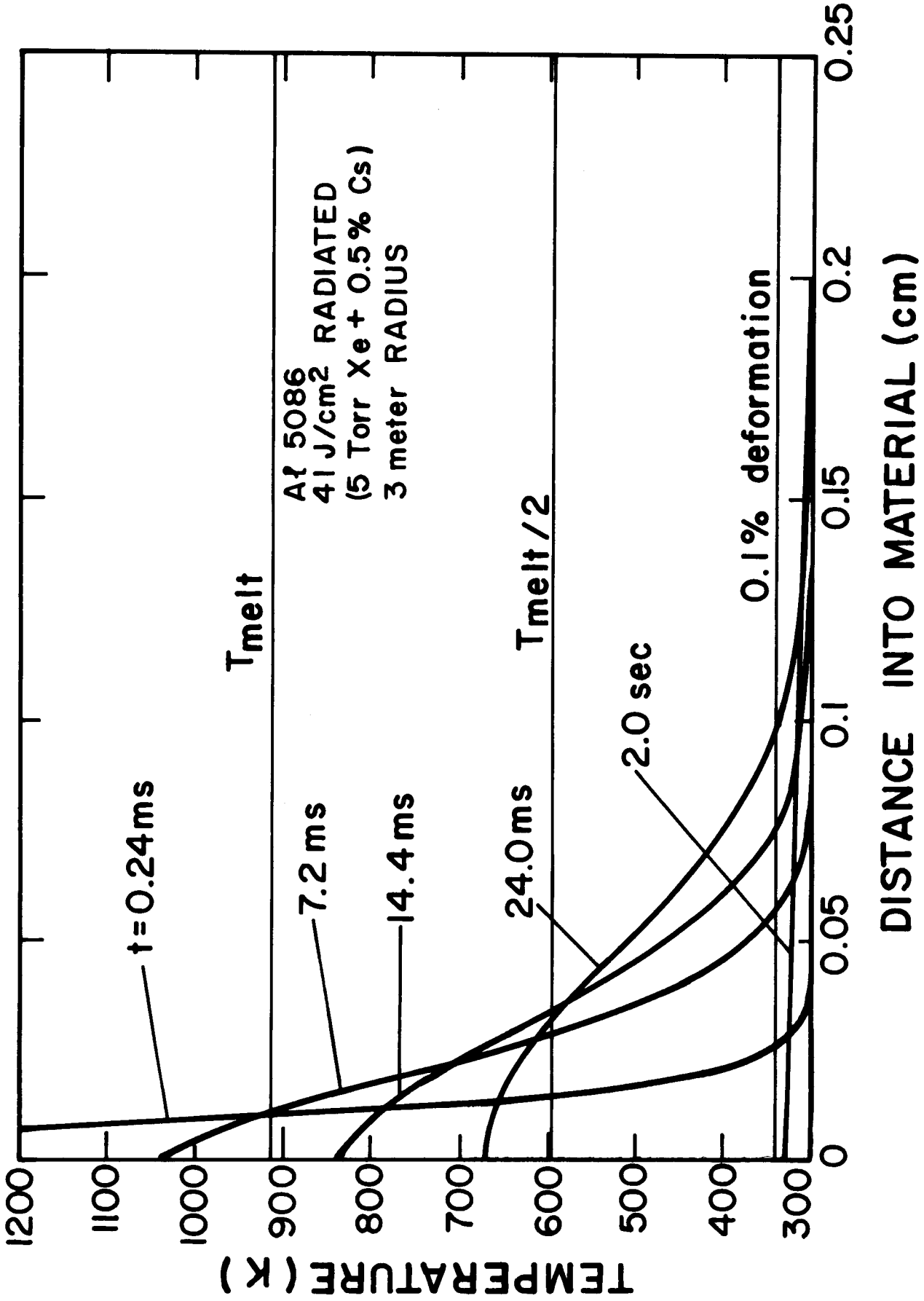

Temperature profiles in an Al 5086 plate versus distance into plate for the heat flux shown in Fig. 10.

Fig. 14

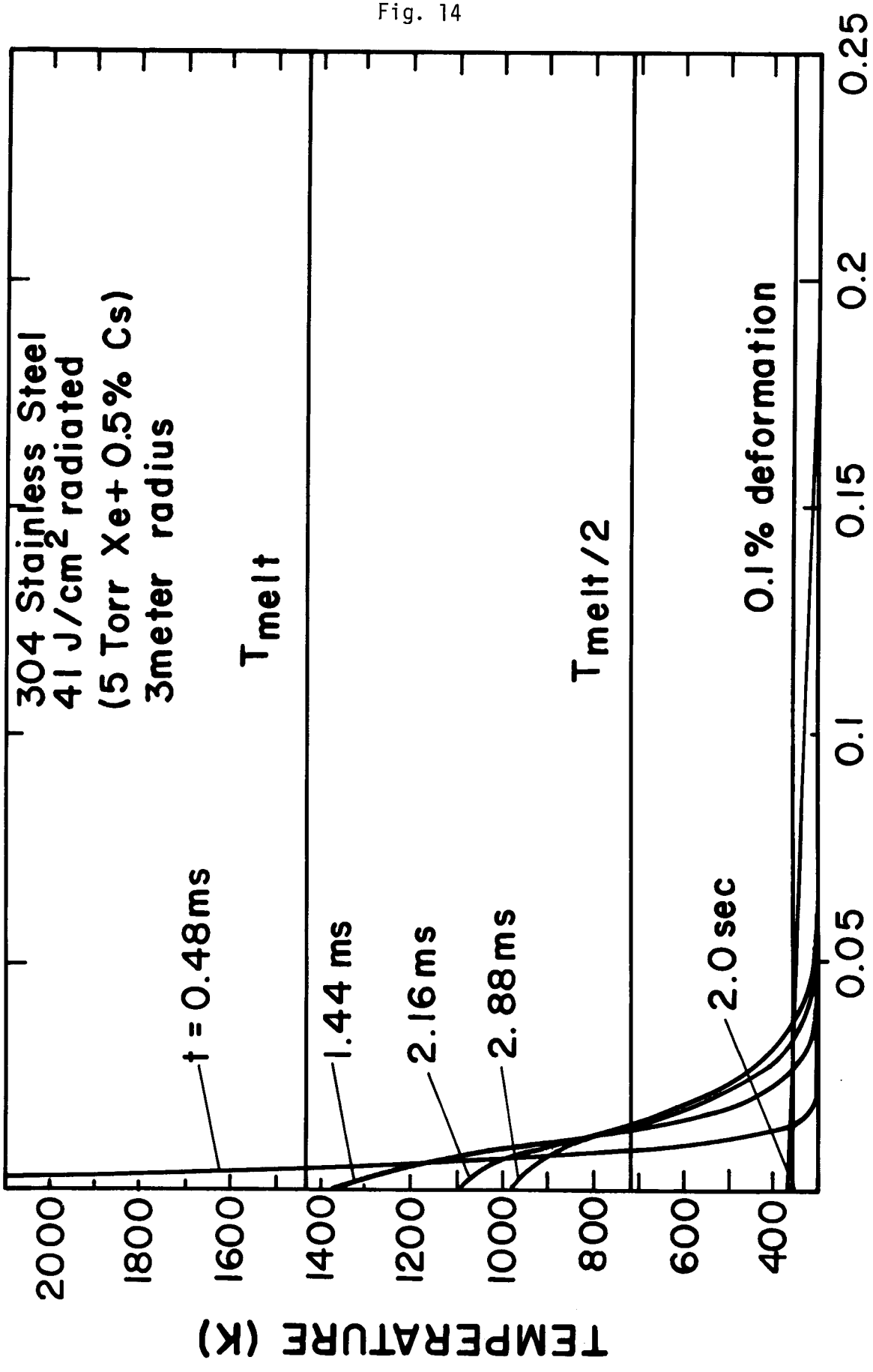

Temperature profiles in a 304 stainless steel plate versus distance into plate for the heat flux shown in Fig. 10.

Fig. 15

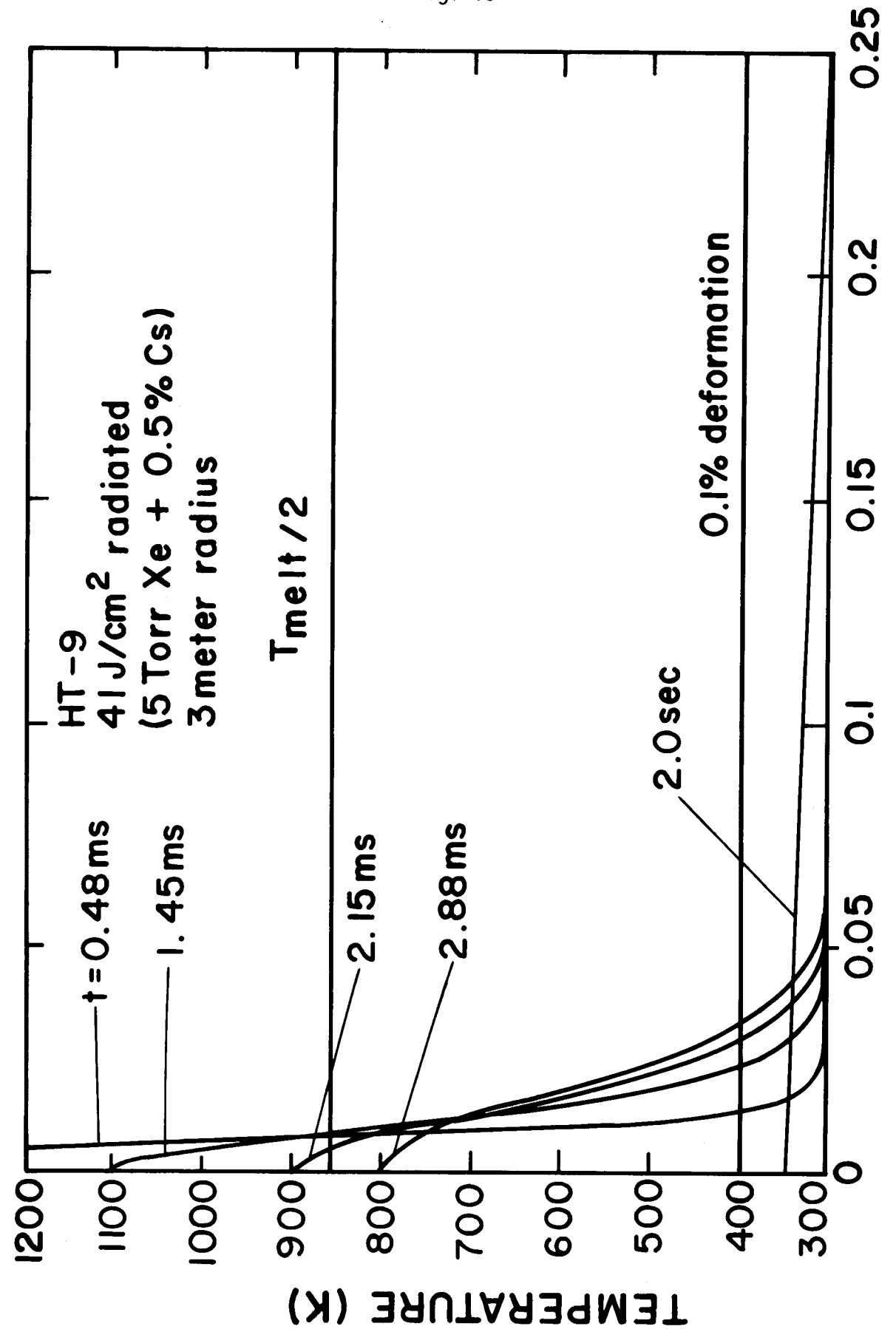

Temperature profiles in a HT-9 plate versus distance into plate for the heat flux shown in Fig. 10.

Fig. 16

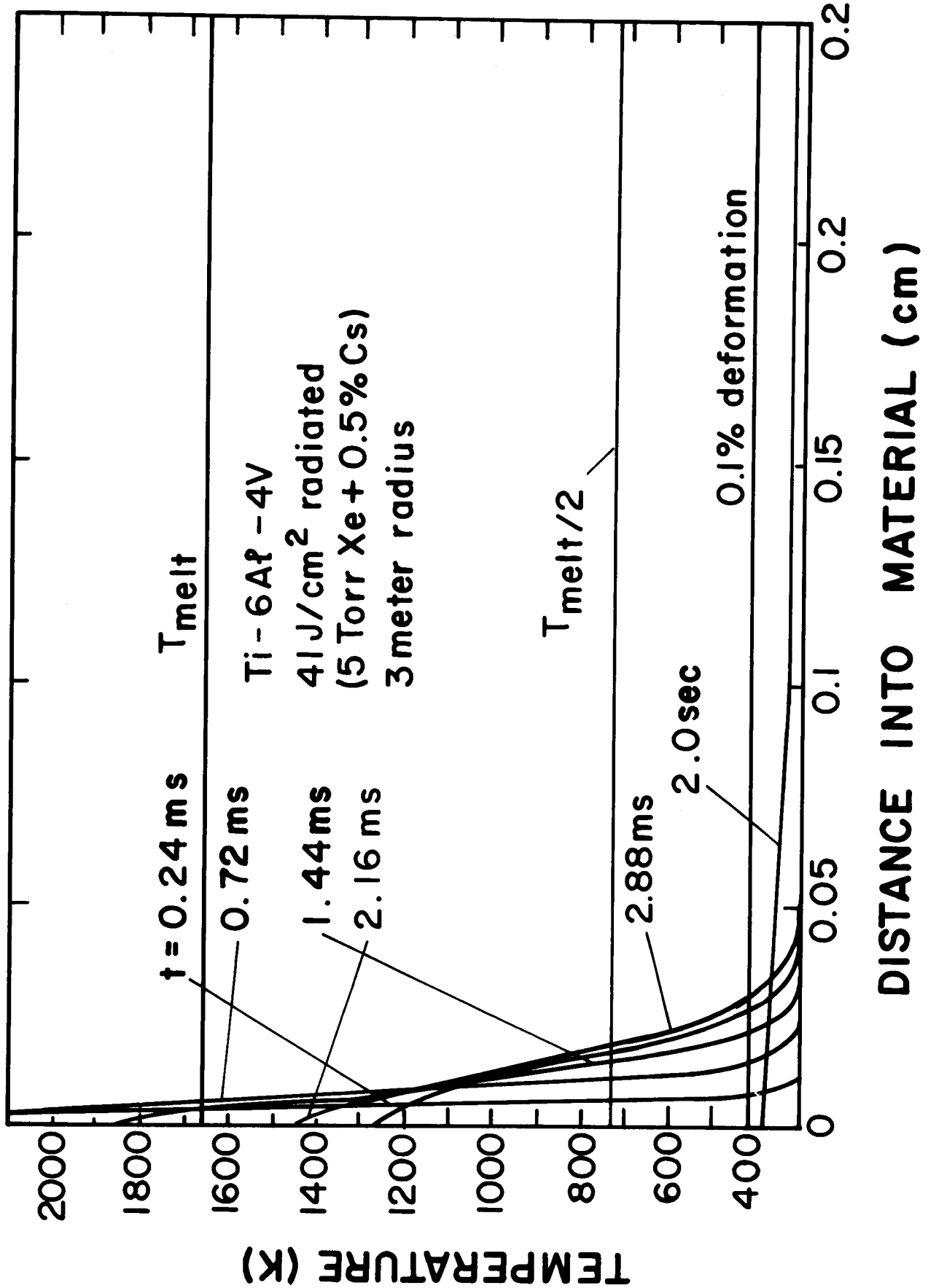

Temperature profiles in a Ti-6Al-4V plate versus distance into plate for the heat flux shown in Fig. 10.

Fig. 17

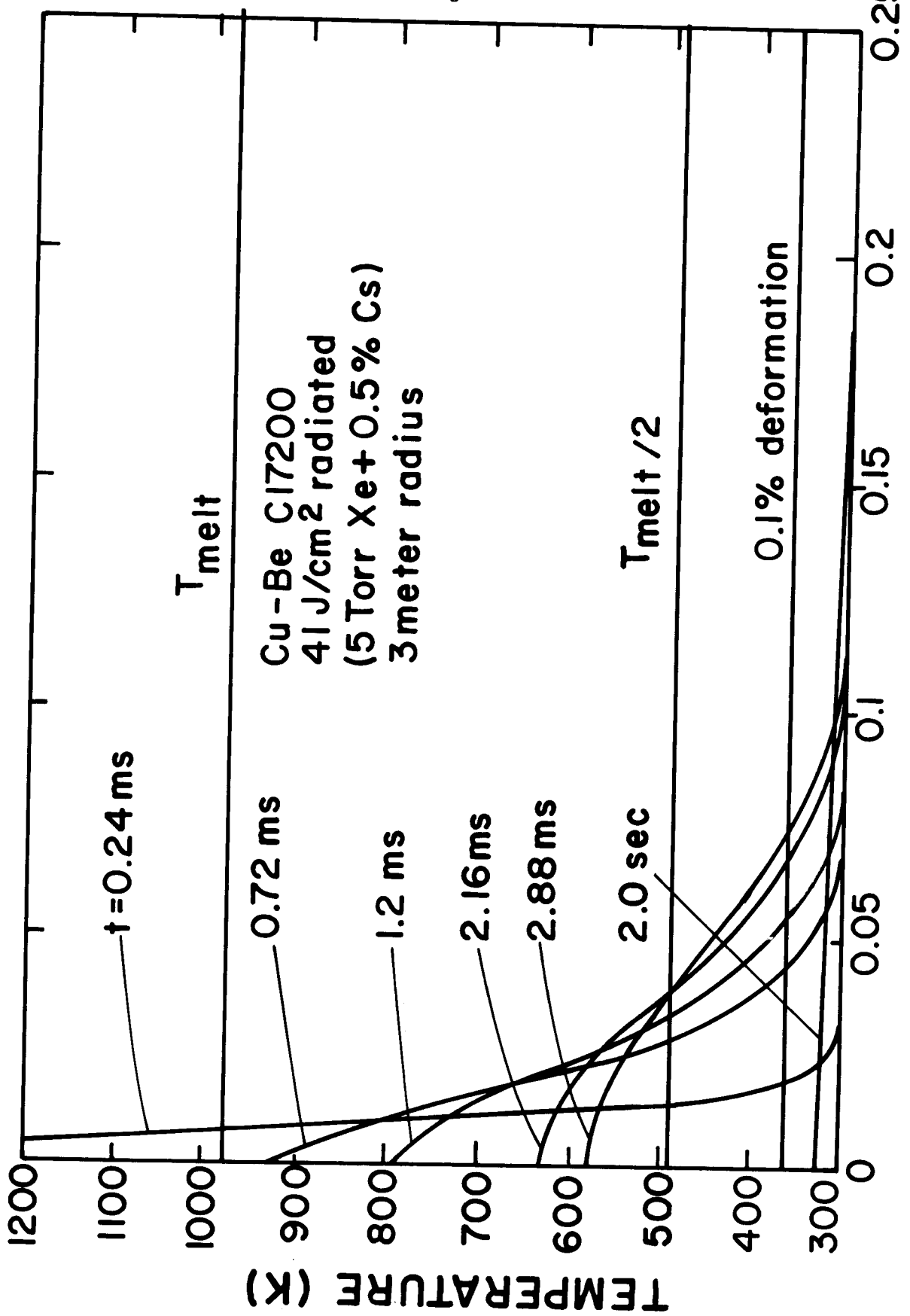

Temperature profiles in a Cu-Be C17200 plate versus distance into plate for the heat flux shown in Fig. 10.

Fig. 18

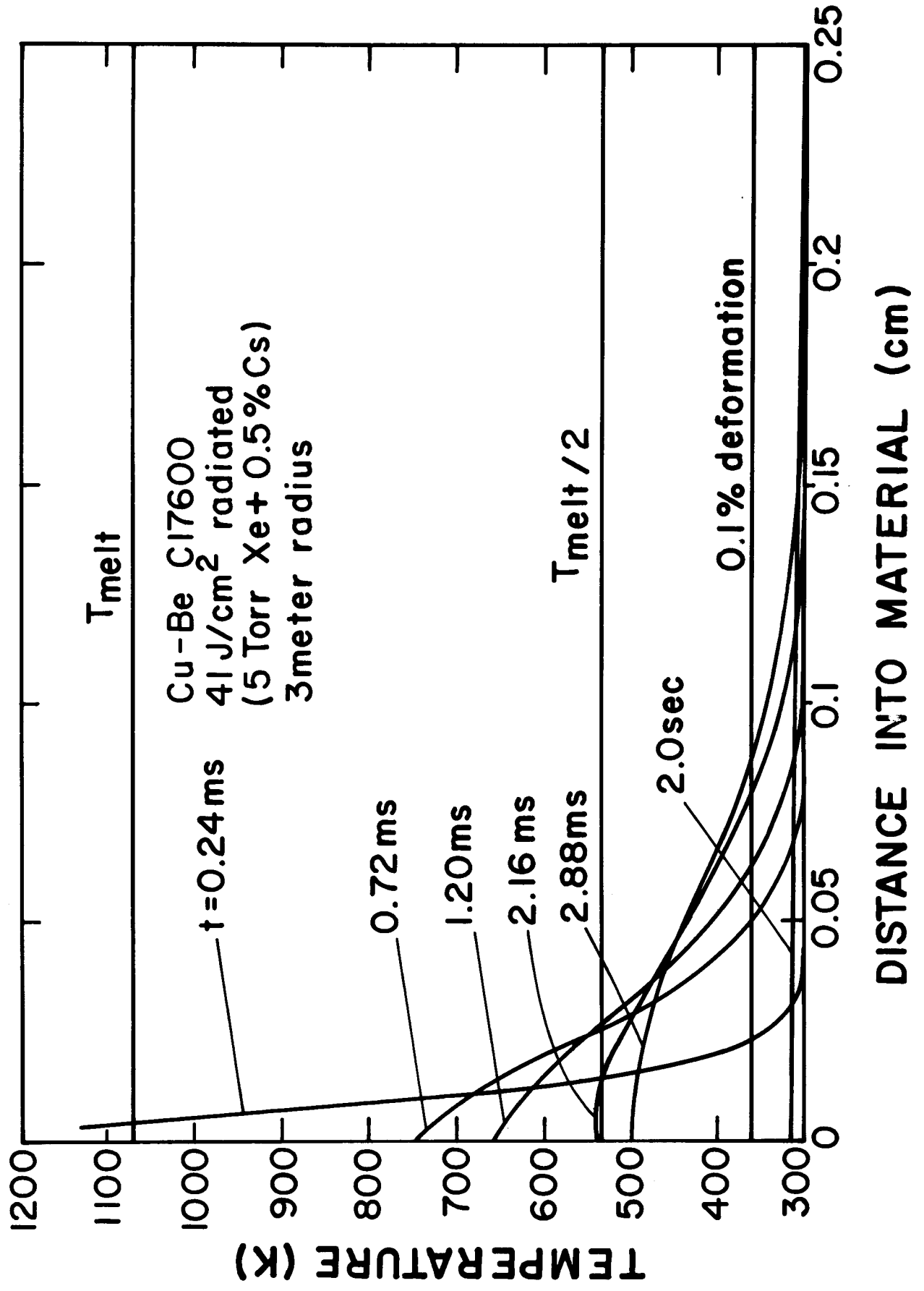

Temperature profiles in a Cu-Be C17600 plate versus distance into plate for the heat flux shown in Fig. 10.

Table VI. First Wall Thermal and Mechanical Response

Material	Melt Layer (cm)	Duration (s)	Deformed Layer (cm)	Fatigue* Width (cm)	Total Plate Thickness (cm)
Al 6061	0.010	4.7×10^{-4}	0.140	3.00	3.140
Al 5086	0.011	4.7×10^{-4}	0.11	3.00	3.11
304 SS	0.0055	2.7×10^{-4}	0.035	2.40	2.44
HT-9	0.0035	7×10^{-4}	0.040	2.0	2.04
Ti-6Al-4V	0.005	2×10^{-3}	0.030	1.95	1.98
Cu-Be C17200	0.007	7×10^{-4}	0.075	1.10	1.16
Cu-Be C17600	0.004	3×10^{-4}	0.086	2.15	2.23

*10^7 cycles or yield stress

has the thickest molten layer. It also has poor fatigue resistance which means that the thickness needed for the mechanical load is large. All materials need thicknesses between 1.16 cm and 3.14 cm, values that are reasonable for construction purposes. In Section V, these plate thicknesses will allow the costs of the materials needed in each case to be determined.

In the above analysis, there are a few assumptions which should be discussed. One such assumption is that cracks generated in the regions undergoing thermal creep will not propagate into the mechanical load bearing regions. This is a reasonable premise because the thickness of the regions where the temperature is between T_{melt} and $T_{melt}/2$ is always small compared with the thickness of the load bearing regions. The crack tips will quickly move into an area where tensile stresses are always small. Another premise is that molten material does not flow before it resolidifies. This is reasonable because the melted layers are always thin, so cohesion with the solid layer is large, the duration of the molten layer is short and the only force parallel to the plane of the plate is gravity. Thus flow of molten material (if any) is not expected to be a problem.

A final point to be made is that the calculations of the temperature profiles predict that 304 stainless steel, HT-9 and Ti-6Al-4V are vaporized to a small degree. The latent heat of vaporization and heat of fusion are neglected so that it is not certain if any vaporization in fact would take place. Also, the heat flux used in these calculations represents the worst case. However, there does remain the possibility that a wall made of one of these materials may be eroded by vaporization.

V. Material Costs

The costs of the materials used in constructing a first wall can be obtained from the wall thicknesses determined in Section IV. The costs of construction are much more difficult to obtain and are not considered here. To a first approximation, the construction costs should be independent of choice of material and should be added to the cost of the materials to find the total cost of the cavity. The costs of the materials themselves are variable, depending on the forms of the materials, the purities needed from radioactivity considerations, etc. The purpose here is not to provide absolute numbers for the material costs but to provide relative costs that will show how the thicknesses of the materials are balanced by the different unit costs of the materials.

The material costs are given in Table VII. The unit costs ($/kg) were obtained from a common source[14] with the exception of HT-9.[15] The masses shown are the total of the 3 meter radius 6 meter high cylindrical cavity, plus the mass of the hemispherical top and bottom. The supporting frame may be assumed to weigh 1.5 times the weight of the wall and the top and bottom, but it is not included in the masses in Table VII.

The cost analysis shows that even though the aluminum walls are the thickest, the material used is the cheapest of all materials considered. Conversely, one of the thinnest walls is made of Ti-6Al-4V but it also has the largest materials cost. In any event, none of these costs appear to be prohibitively large.

VI. Radioactivity

The radioactivity induced in the first wall and supporting structure by 14 MeV fusion neutrons can cause troublesome maintenance and operating

Table VII. First Wall Panel Materials Costs (Unfabricated)

Material	Unit Cost ($/kg)	Mass (kg)	Cost ($)
Al 6061	1.8	1.92×10^4	3.5×10^4
Al 5086	1.8	1.89×10^4	3.4×10^4
304 SS	1.26	4.42×10^4	5.56×10^4
HT-9	18.	3.58×10^4	6.44×10^5
Ti-6Al-4V	27.8	1.98×10^4	5.5×10^5
Cu-Be C17200	8.35	2.16×10^4	1.8×10^5
Cu-Be C17600	8.35	4.72×10^4	4.0×10^5

problems for the Target Development Facility. We anticipate that the radioactive inventory will not pose a disposal problem so we have concentrated on the resultant dose from this radioactive structure. We assume that there are ten full yield 200 MJ shots per day. This represents an average fusion power level of 23 kW. We assume that 70% of the energy is in neutrons. Hence, the neutron power is 16 kW. At such low power levels, in comparison to our fusion reactor designs for instance, we would expect that there may be non-saturation effects in the decay chains. For this reason we have computed the dose for one week and for one year of operating time at 16 kW. These calculations have thus far been done for three of our candidate wall materials: Al 6061, HT-9, and 304 stainless steel. The isotopic compositions of these materials are given in Table VIII. The radiation doses experienced at the surface of the first wall and from the operating floor, 8 meters away, are given in Tables IX and X. In Table IX we show the dose at these two locations as a function of time after shutdown after operating for one year. We see that for Al 6061, we could enter the target chamber at one week after shutdown without experiencing excessive doses. For the ferritic and stainless steels we would see a substantial dose at the first wall even after one week. It is interesting to note that the Al 6061 is much hotter at shutdown than the steels, but it decays much more quickly. If remote handling were acceptable then the steels would allow manipulation from the operating floor while remaining within tolerable radiation levels. This scenario of course assumes that access to the target chamber will be very infrequent.

In Table X we give the results of calculations assuming only one week of operation before shutdown. Again, the Al 6061 is very hot at first and then quickly decays. The steels reach nearly the same dose levels at shutdown, but

Table VIII. Isotopic Composition of 304 SS, HT-9, and Al 6061 (cm^{-3})

304 SS

Si-28	7.3×10^{20}	Si-29	3.72×10^{19}	Si-30	2.38×19^{19}
Cr-50	6.94×10^{20}	Cr-52	1.35×10^{22}	Cr-53	1.54×10^{21}
Cr-54	3.83×10^{20}	Mn-55	1.01×10^{21}	Fe-54	3.48×10^{21}
Fe-56	5.48×10^{22}	Fe-57	1.31×19^{21}	Fe-58	1.97×10^{20}
Ni-58	5.09×10^{21}	Ni-60	1.97×10^{21}	Ni-61	8.92×10^{19}
Ni-62	2.74×10^{20}	Ni-64	8.10×10^{19}	Cu-63	1.03×10^{20}
Cu-64	4.60×10^{19}	Mo-92	2.58×10^{19}	Mo-94	1.47×10^{19}
Mo-95	2.56×10^{19}	Mo-96	2.69×10^{19}	Mo-97	1.54×10^{19}
Mo-98	3.88×10^{19}	Mo-100	1.57×10^{19}		

HT-9

Si-28	3.9×10^{20}	Si-30	1.2×10^{19}	V-50	2.75×10^{20}
Cr-50	4.47×10^{20}	Cr-52	8.7×10^{21}	Cr-53	9.91×10^{20}
Cr-54	2.47×10^{20}	Mn-55	4.27×10^{20}	Fe-54	4.17×10^{21}
Fe-56	6.56×10^{22}	Fe-57	1.57×10^{21}	Fe-58	2.36×10^{20}
Ni-58	2.71×10^{20}	Ni-60	1.04×10^{20}	Ni-62	1.46×10^{19}
Ni-64	4.3×10^{17}	Mo-92	7.75×10^{19}	Mo-95	7.7×10^{19}
Mo-96	8.1×10^{19}	Mo-97	4.6×10^{19}	Mo-98	1.16×10^{20}
Mo-100	4.7×10^{19}	W-174	2.0×10^{17}	W-182	3.4×10^{19}
W-183	1.8×10^{19}	W-184	3.9×10^{19}	W-186	3.6×10^{19}

Al 6061

Mg-24	4.74×10^{20}	Mg-25	6.11×10^{19}	Mg-26	6.73×10^{19}
Al-27	5.82×10^{22}	Si-28	3.20×10^{20}	Si-29	1.63×10^{19}
Si-30	1.07×10^{19}	Cr-50	4.04×10^{18}	Cr-52	7.86×10^{19}
Cr-53	8.96×10^{18}	Cr-54	2.23×10^{18}	Mn-55	4.44×10^{19}
Fe-54	1.19×10^{19}	Fe-56	1.87×10^{20}	Fe-57	4.46×10^{18}
Fe-58	6.73×10^{17}	Cu-63	5.30×10^{19}	Cu-65	2.37×10^{19}

Table IX. Dose Calculations for LIB-TDF

One Year Operating Time @ 16 kW

Time After Shutdown	Dose At First Wall (mr/hr)	Dose At Operating Floor (mr/hr)
	Al 6061	
0	2.1×10^3	230
1d	2.6×10^2	28
1w	1.65	0.18
	HT-9	
0	489	55
1d	114	13
1w	101	11
	SS 304	
0	481	54
1d	109	12
1w	105	12

Table X. Dose Calculations for LIB-TDF

One Week Operating Time @ 16 kW

Time After Shutdown	Dose At First Wall (mr/hr)	Dose At Operating Floor (mr/hr)
	Al 6061	
0	2.1×10^3	2.3×10^2
1d	264.	28.
1w	0.4	4×10^{-2}
	HT-9	
0	369.	42.8
1d	13.9	1.56
1w	2.58	0.23
	SS 304	
0	373.	43.3
1d	5.8	0.66
1w	3.6	0.42

their longer-lived radionuclides have not saturated, hence the dose at one week after shutdown is tolerable. However, this dose will build up over time so that in one year it will be nearly the same as in the previous scenario.

We see that the radiation fields associated with an aluminum wall and structure are initially more intense than for steel. But they decay much more quickly so that one week after shutdown, the dose is low enough to allow hands-on access to the target chamber. This is not the case for the steels. However, remote access from the operating floor is possible after one week for the steel structure.

An important element of this analysis that has not been addressed is the problem of radioactive target debris and tritium. The target ablator and pusher will experience very intense neutron fields which will lead to some radioactive inventory. The mass transport of the material within the gas filled target chamber is a complex problem that has not been addressed in this study. Although tritium is a benign radioactive isotope, it will be present in copious amounts. Hence any adsorption or absorption of tritium in the target chamber will lead to radioactive hazards that have not been addressed.

From the analysis that has been done thus far, the best choice from a radioactivity standpoint is aluminum. It should be mentioned that high purity aluminum is available if dose levels from impurities pose a serious problem. However, from our current results we conclude that this additional expense is not necessary.

VII. Conclusions

The choice of first wall material has been investigated for the TDF. Mechanical and thermal properties have been accumulated for the materials considered. Mechanical responses have been predicted for the largest credible

shock overpressure and thermal responses have been determined for the largest heat flux on the first wall. Induced radioactivity has been calculated for walls made of some of the materials. Required thicknesses and material costs are finally found for the materials.

It has been found that Al 6061 is a good choice of material for the TDF first wall. Calculations show that one week after shutdown, the radioactivity is low enough for hands-on maintenance. Cost estimates also show that the aluminum alloys are the cheapest of those materials considered. The thicknesses needed for these alloys are reasonable for construction. The major problem with aluminum is its incompatibility with Na and Cs. Recall that these impurities in the cavity gas are present to enhance channel breakdown by laser beams. This leads us to suggest that other cavity gas candidates be investigated for the TDF. With this qualification Al 6061 is suggested for serious consideration as the first wall material.

Acknowledgment

This work was supported by Sandia National Laboratories under contract DE-AS08-81DP40161.

References

1. Lawrence Livermore Laboratory Laser Fusion Annual Report - 1978, UCRL-50021-78.

2. R.W. Conn et al., "SOLASE - A Conceptual Laser Fusion Reactor Design," University of Wisconsin Fusion Engineering Program Report UWFDM-220 (Dec. 1977).

3. E.W. Sucov, "Inertial Confinement Fusion Central Station Electrical Power Generation Plant," DOE/DP/40086-1 (Feb. 1981).

4. B. Badger et al., "HIBALL - A Conceptual Heavy Ion Beam Driven Fusion Reactor Study," University of Wisconsin Fusion Engineering Program Preliminary Report UWFDM-450/KfK-3202 (June 1981).

5. D.L. Cook et al., "Light Ion Driven Inertial Fusion Reactor Concepts," Proc. of the 4th Topical Mtg. on the Technology of Controlled Nuclear Fusion, King of Prussia, PA, Oct. 14-17, 1980, pp. 1386-1394.

6. G.A. Moses and R.R. Peterson, "FIRE - A Computer Code to Simulate Cavity Gas Response to Inertial Confinement Target Explosions," University of Wisconsin Fusion Engineering Program Report UWFDM-336 (Jan. 1980); also, T.J. McCarville, R.R. Peterson, and G.A. Moses, "Improvements in the FIRE Code for Simulating the Response of a Cavity Gas to Inertial Confinement Fusion Target Explosions," University of Wisconsin Fusion Engineering Program Report UWFDM-407 (June 1981).

7. "Aerospace Structural Metals Handbook," Mechanical Properties Data Center, Belfour Stalen, Inc., Traverse City, MI, (1975, 1981).

8. "Metals Handbook," 9th Ed., American Society for Metals, Metals Park, OH, (1979).

9. "Structural Alloys Handbook," Battelle Columbus Laboratories, Columbus, OH, (1981).

10. C.C. Baker et al., "STARFIRE - A Commercial Tokamak Fusion Power Plant Study," Argonne National Laboratory ANL/FPP-80-1 (1980).

11. E.G. Lovell, R.R. Peterson, R.L. Engelstad, and G.A. Moses, "Transient Elastic Stresses in ICF Reactor First Wall Structural Systems," University of Wisconsin Fusion Engineering Program Report UWFDM-421 (Aug. 1981), presented at the 2nd Topical Meeting on Fusion Reactor Materials, 9-12 August 1981, Seattle, WA.

12. R.R. Peterson, K.J. Lee, and G.A. Moses, "Low Density Cavity Gas Fireball Dynamics in the Light Ion Beam Target Development Facility," University of Wisconsin Fusion Engineering Program Report UWFDM-442 (Oct. 1981), presented at 9th Symposium of Engineering Problems of Fusion Research, 26-29 October 1981, Chicago, IL.

13. A.M. Hassanein and G.L. Kulcinski, "A*THERMAL Code Description," University of Wisconsin Fusion Engineering Program Report (in preparation).

14. Materials in Design Engineering, Materials Selector Issue.

15. "Fusion Reactor Design Studies: Standard Cost Estimating Rules," Battelle Pacific Northwest Laboratories PNL-2987.

3. STRUCTURAL FRAME DESIGN

3.1 Introduction

Considerable progress has been made in the development of procedures for the analysis and design of first wall panels to withstand thermal and mechanical loadings [3.1, 3.2]. Typical results are presented in other sections of this report. The panels were assumed to be supported by a framework that was essentially rigid. The overall view of the proposed Target Development Facility shows the chamber wall with a system of axial stringers and circumferential ribs. This structural frame must also be designed to carry the dynamic mechanical loads.

In the analysis which follows, the frame is modeled as a system of beams in which the curvature and hoop force capacity of the ribs are not included. In addition, as far as the frame is concerned, the plates are assumed to transmit the full strength of the overpressure, without resistance from circumferential tensile stresses. This approach will lead to an extremely conservative design. However future efforts will focus on refinements in this modeling.

3.2 Frame Analysis

The dynamic overpressure is taken as uniform over the plates and partitioned to the ribs and stringers as shown in Figure 3.1. The tributary areas will produce uniformly varying line loads with maximum values pa and pb for stringers and ribs, respectively, where p denotes the maximum overpressure from the shock. The rib and stringer analysis involves a procedure which is very similar to that used for the plates. The static response is first determined. This is subsequently modified by means of a Dynamic Load Factor (DLF) to account for dynamic effects [3.3]. In this case, rib and stringer lengths have been chosen a priori. The design effort primarily

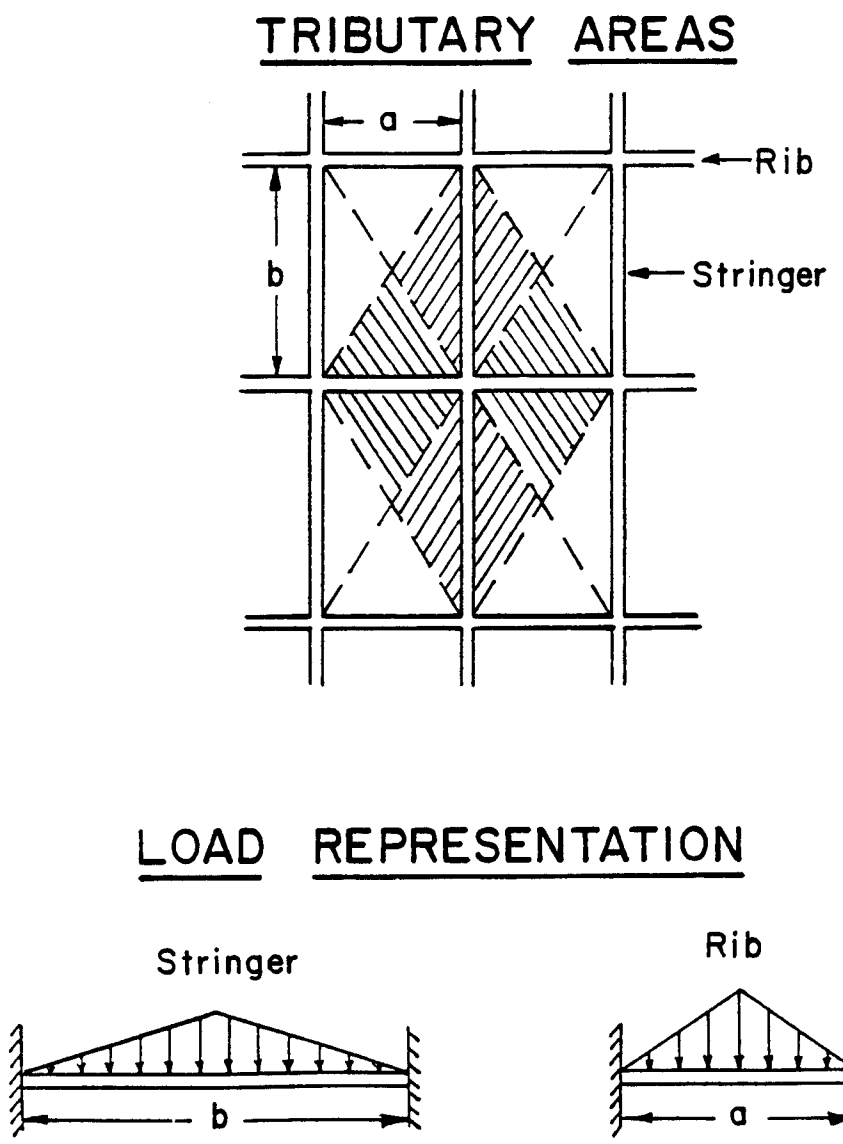
TRIBUTARY AREAS
a
b
Rib
Stringer
LOAD REPRESENTATION
Stringer
b
Rib
a

Figure 3.1

involves the determination of cross section characteristics such that the mechanical stresses are within design limits and deflections are not excessive.

The analytical details (equations, etc.) will not be included in this summary but will be presented later in a final report. The analysis uses a prismatic beam element with uniform mass per unit length under a time-dependent loading which may be arbitrarily distributed but is eventually specialized to the profile shown in Fig. 3.1. End conditions are characterized as "fixed," i.e., having negligible rotation. The effects of shear deformation, rotary inertia and damping are not included. It is necessary to calculate the natural frequencies and corresponding spatial mode shapes. These are used in a modal superposition method to determine the forced response. The deflection results are also used to compute the flexural moment (also a function of position and time) and thus the dynamic flexural stress.

3.3 Quantitative Results

A number of materials have been proposed for the wall panels and it would be practical to use the same alloy for the ribs and stringers. Since these components are completely immersed in the shield water, the material properties used correspond to 25°C. The numerical values are listed in Table (2.3).

The dependence of rib and stringer fundamental frequencies on cross sectional radius of gyration is shown in Figure 3.2. It can be seen that the natural frequencies of ribs are approximately an order of magnitude greater than those of the stringers. This is an important design consideration since dynamic load factors are strongly influenced by the flexural frequency magnitudes. The dynamic load factors also depend upon the ramp time (t_r) and the exponential decay coefficient (k).

The panel analysis was based on a specific case which, for consistency, will be used for the frame as well. This corresponds to Xenon cavity gas seeded with 0.5% Cs with a resulting maximum overpressure of 1.71 MPa at 1.32 ms. The coefficients t_r and k were determined to be 0.14 ms and 3432/sec, respectively. With these, numerical computations were carried out to obtain the maximum DLF as a function of fundamental vibration frequency and is shown in Figure 3.3. Because of the relatively low frequencies of the stringers, the DLF will generally be less than unity but the rib DLF's will be substantially larger. These results have been used to develop design curves for dynamic flexural stress as a function of cross section modulus for both stringers and ribs. The overpressures cover a range of values and include the specific case of 1.71 MPa as shown in Figures 3.4 and 3.5. It should be noted that the stress graphs can be used for any elastic material under the given conditions. The design stress would be based upon both the yield characteristics of the material and the DLF. With this, the section modulus can be determined and thus the beam properties are established. In addition, deflections can be evaluated by using Figures 3.6 - 3.15 in which displacement is shown as a function of cross section moment of inertia for stringers and ribs for the various materials under consideration.

3.4 Numerical Example

A specific case is presented here to outline the procedure. The material selected is aluminum 6061 with a yield stress of 276 MPa. Cavity gas is Xenon with 0.5% Cs and an overpressure of 1.71 MPa as indicated earlier. In the work which follows, the following notation is used:

I = major axis moment of inertia

S = major axis section modulus

r = major axis radius of gyration

ω = fundamental flexural frequency

σ = flexural stress

y = maximum transverse displacement

The various steps in the design procedure are summarized in Table 3.1. It can be seen that the AISC manual has first been used to select four different sizes of rectangular structural tubing. For each of these, the relevant cross section parameters are listed. Next, the fundamental frequency is determined and consequently the DLF is established. Using the cross section modulus (S) and moment of inertia, the static stress and deflection (σ_s and y_s) for each are found from the appropriate design curves. These in turn must be amplified by the DLF to give the corresponding dynamic response (σ_d and y_d). Finally, each dynamic result must be compared with the design limits.

From the sample calculations in the table it is observed that the stresses in the 8 inch tubing are below yield with acceptable deflections for both stringers and ribs. With these dimensions a section of the wall and frame has been drawn in proportion and is shown in Figure 3.16.

This specific example is intended to identify the details of the design procedure. Different aspect ratios for the stringer and rib spacings can be used. As well, different geometries for the stringer and rib cross sections can be considered.

Finally it should be emphasized that the analysis upon which the design procedure is based is extremely conservative. Refinements will lead to a design in which stringers and ribs are both lighter and not as closely spaced.

FUNDAMENTAL FREQUENCY vs. CROSS SECTION RADIUS OF GYRATION

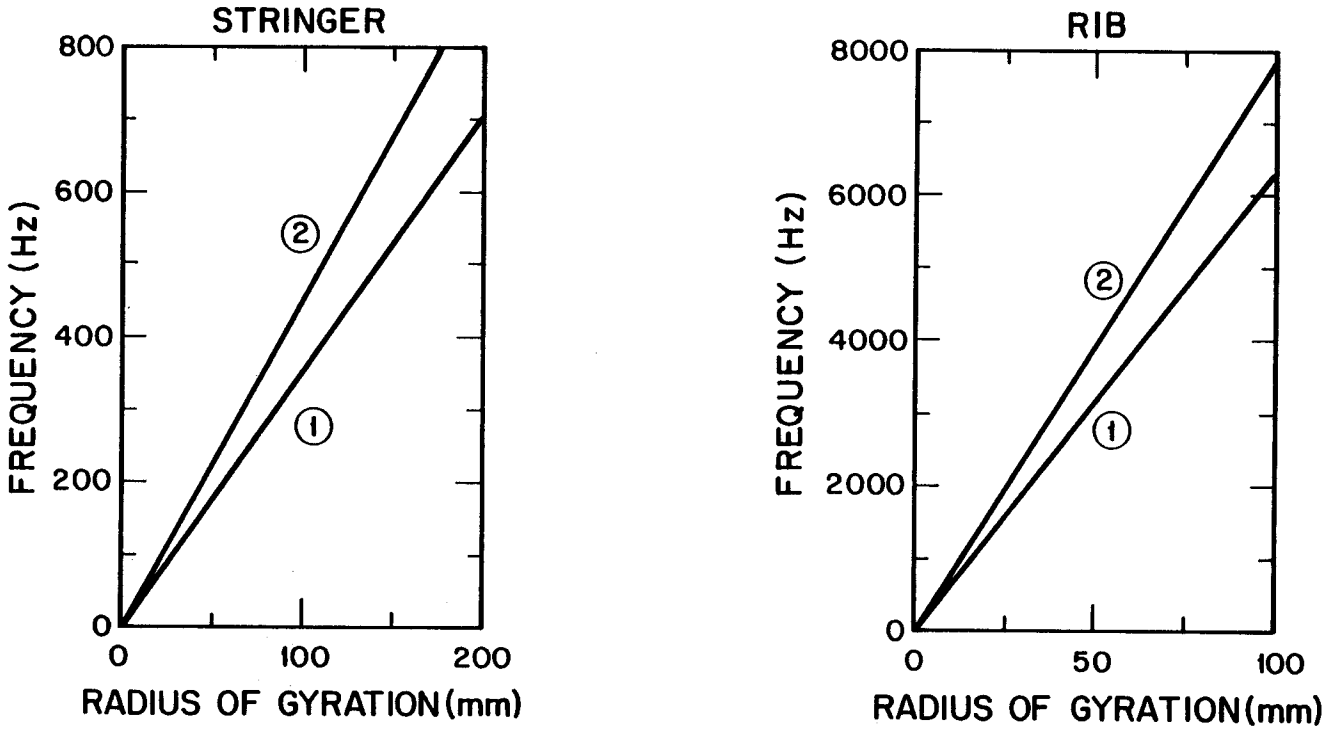

① Cu-Be
② Al 6061/5086, 304 SS, HT-9, Ti-6Al-4V

Figure 3.2

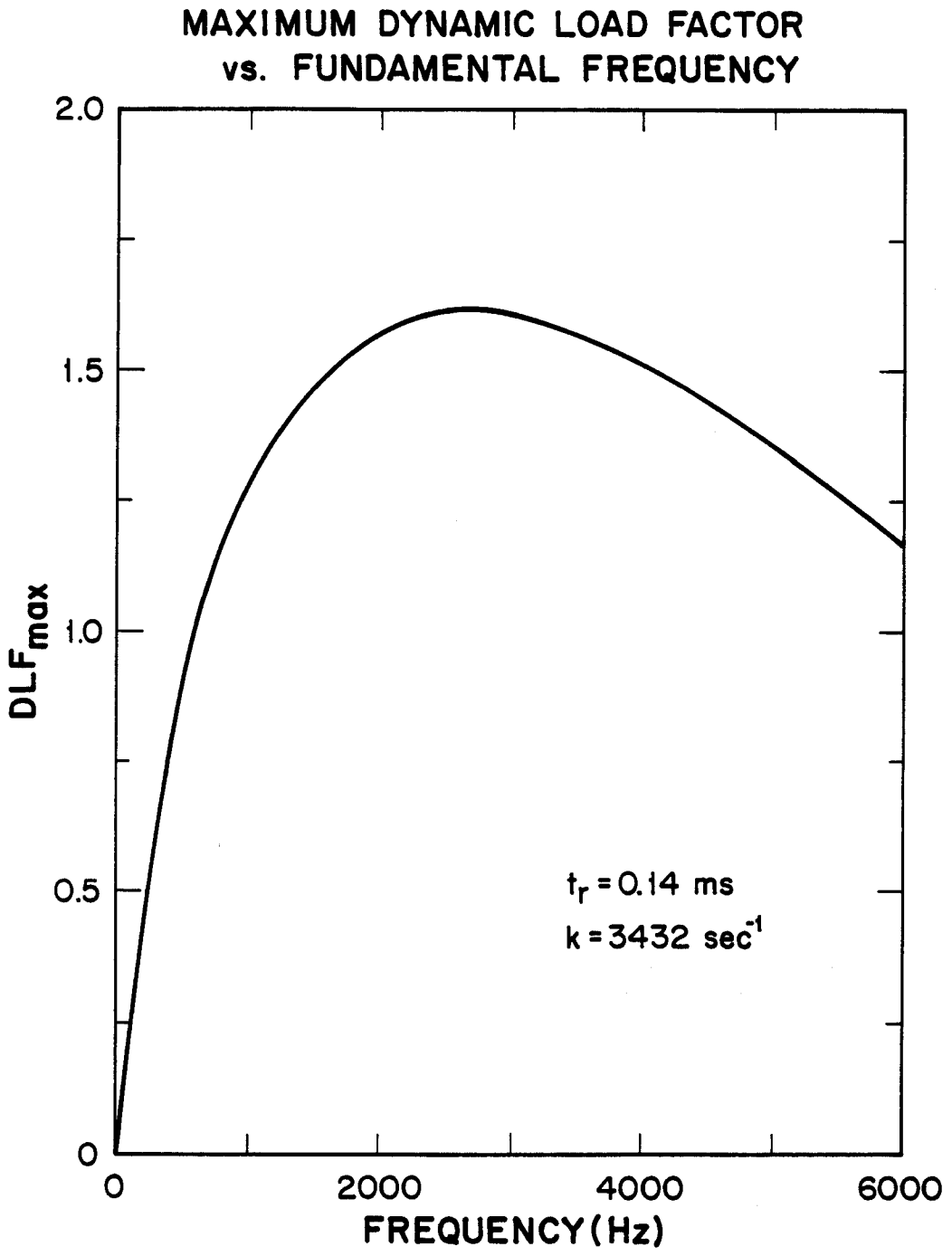
MAXIMUM DYNAMIC LOAD FACTOR
vs. FUNDAMENTAL FREQUENCY
2.0
1.5
1.0
0.5
0
DLF max
0
2000
4000
6000
FREQUENCY (Hz)
t_r = 0.14 ms
k = 3432 sec^{-1}

Figure 3.3

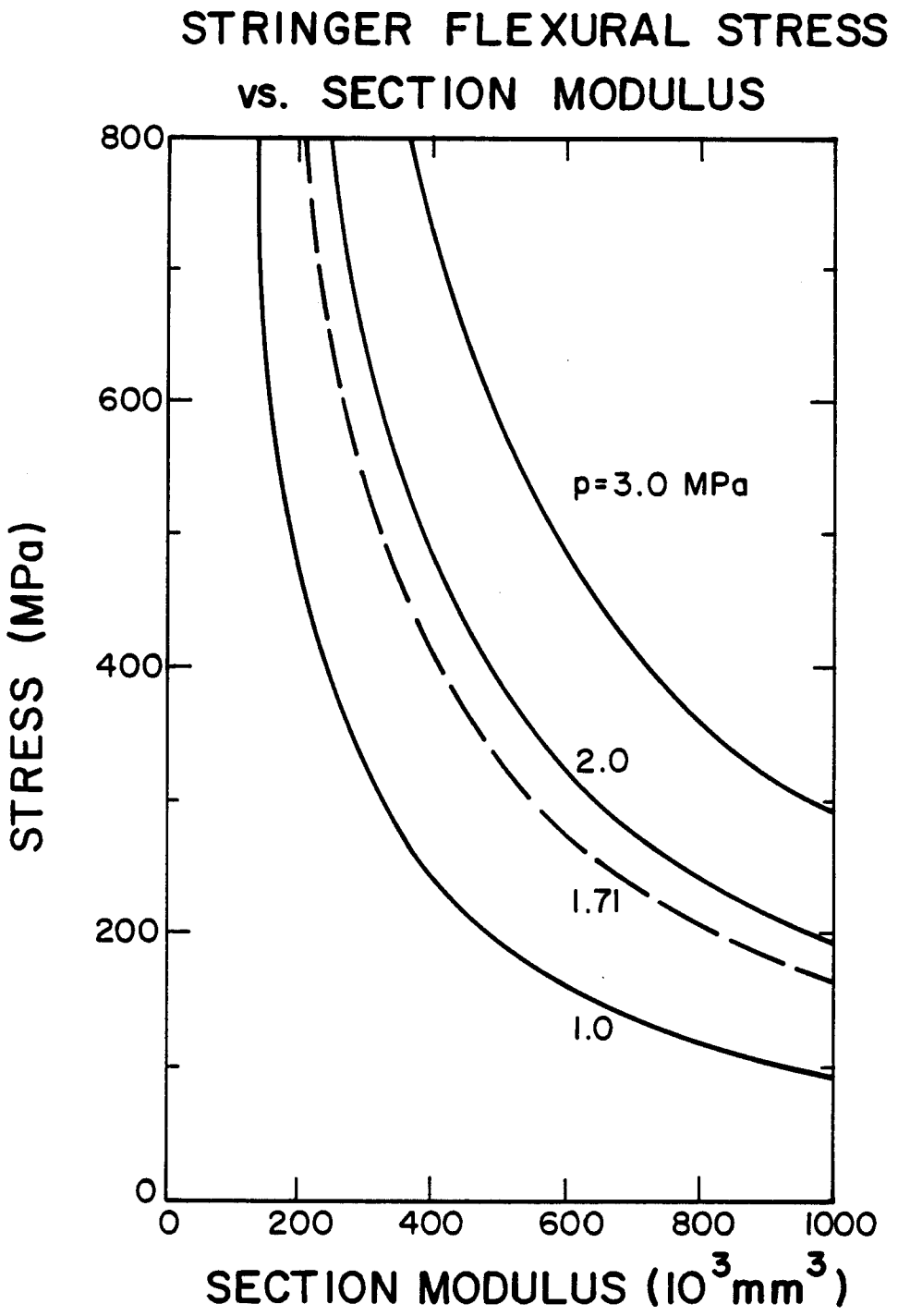
STRINGER FLEXURAL STRESS
vs. SECTION MODULUS
STRESS (MPa)
800
600
400
200
0
0
200
400
600
800
1000
SECTION MODULUS ($10^3 mm^3$)
p=3.0 MPa
2.0
1.71
1.0

Figure 3.4

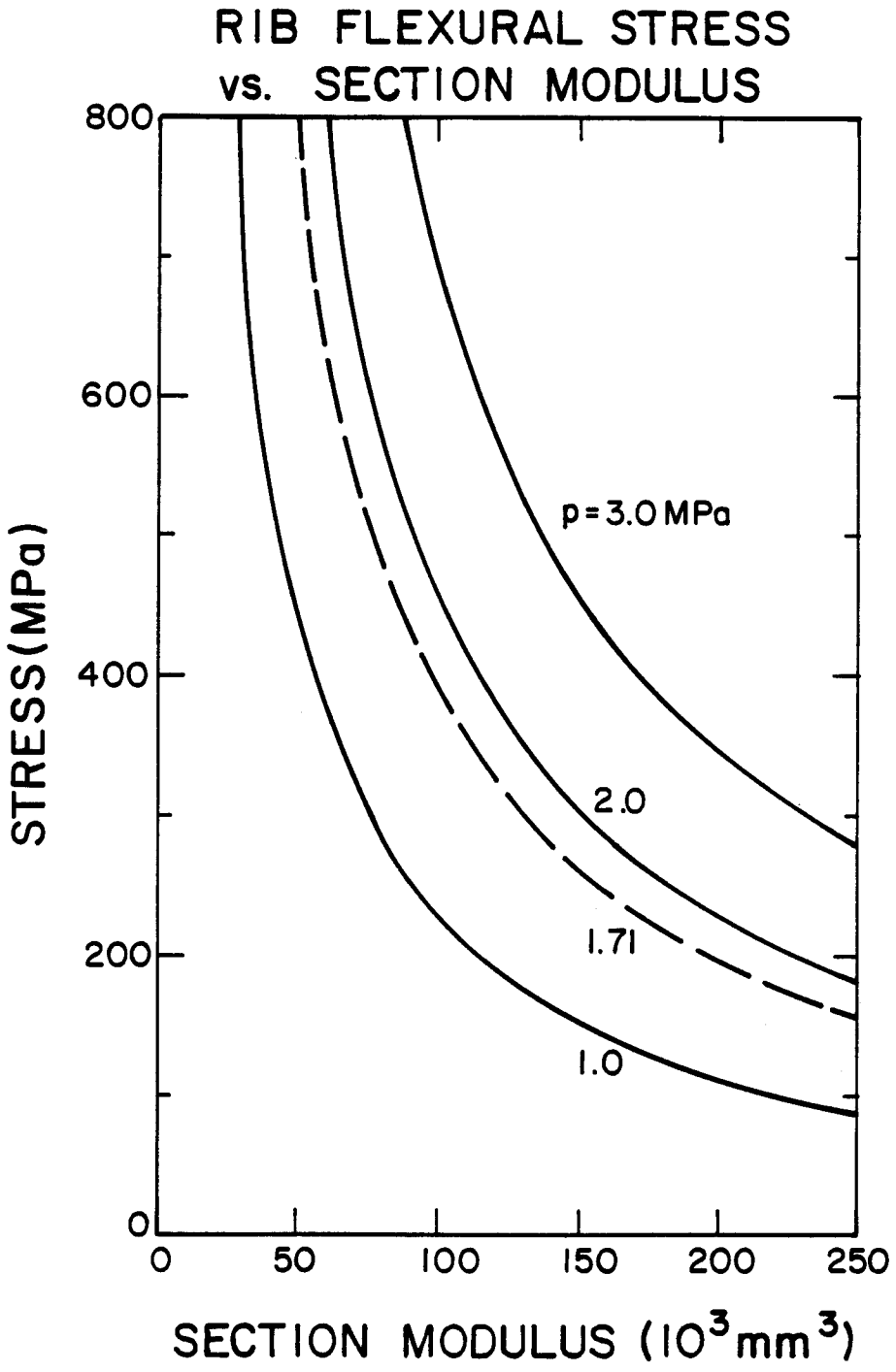
RIB FLEXURAL STRESS
vs. SECTION MODULUS
800
600
400
200
0
STRESS(MPa)
p=3.0 MPa
2.0
1.71
1.0
0
50
100
150
200
250
SECTION MODULUS ($10^3 mm^3$)

Figure 3.5

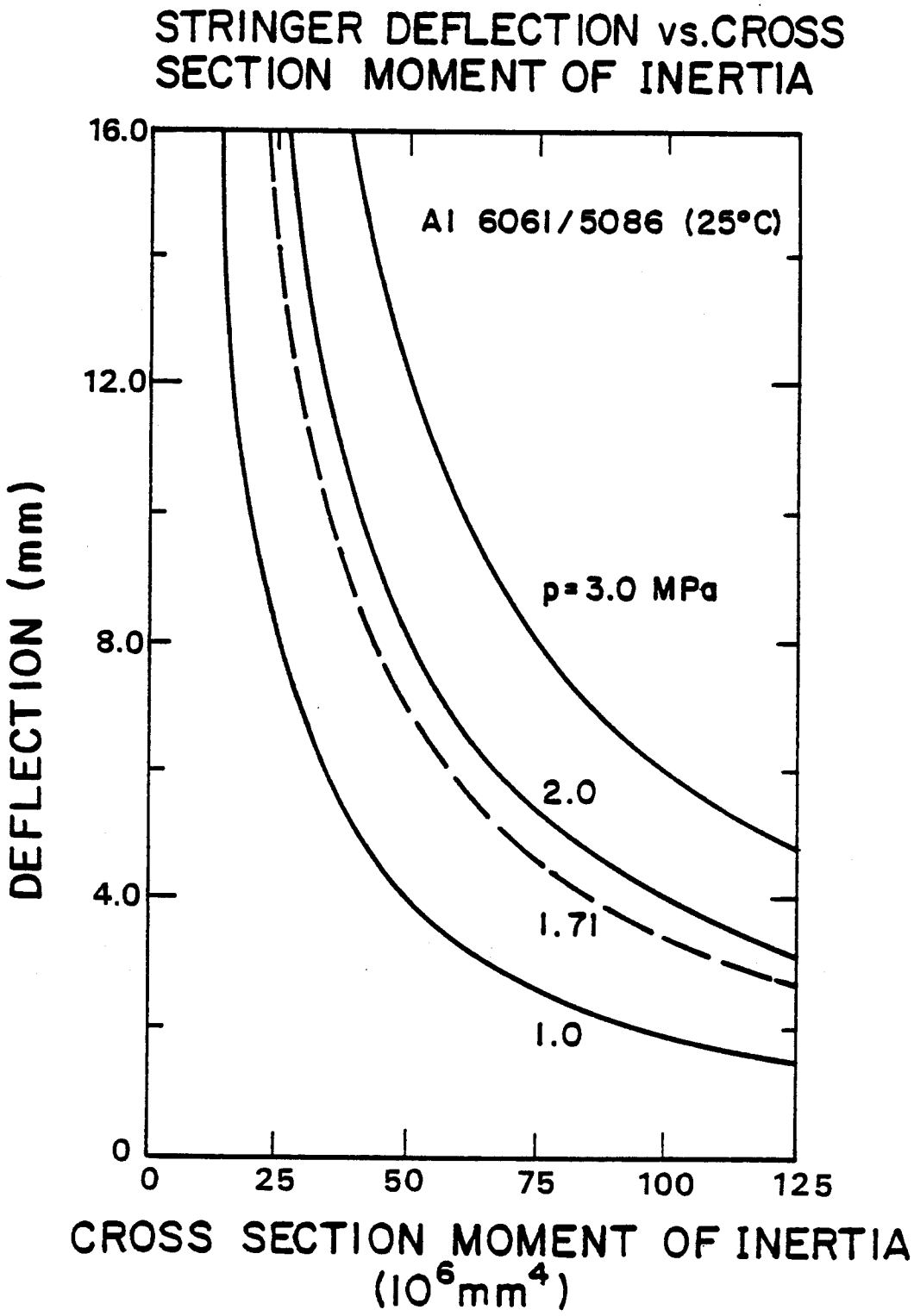
STRINGER DEFLECTION vs.CROSS SECTION MOMENT OF INERTIA
Al 6061/5086 (25°C)
p=3.0 MPa
2.0
1.71
1.0
DEFLECTION (mm)
16.0
12.0
8.0
4.0
0
0
25
50
75
100
125
CROSS SECTION MOMENT OF INERTIA
(10^6 mm^4)

Figure 3.6

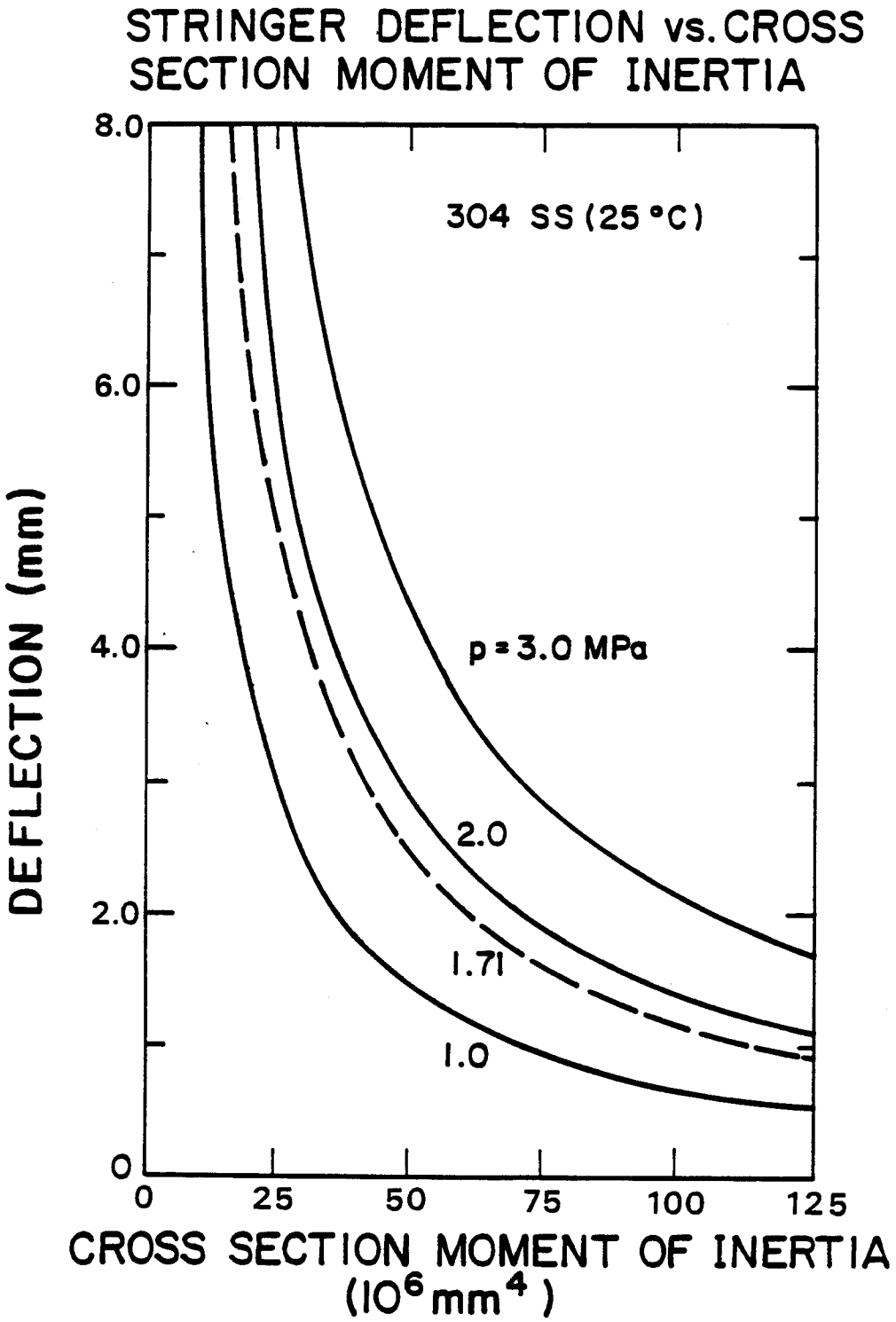
STRINGER DEFLECTION vs. CROSS SECTION MOMENT OF INERTIA
304 SS (25 °C)
p = 3.0 MPa
2.0
1.71
1.0
DEFLECTION (mm)
8.0
6.0
4.0
2.0
0
0
25
50
75
100
125
CROSS SECTION MOMENT OF INERTIA
(10⁶ mm⁴)

Figure 3.7

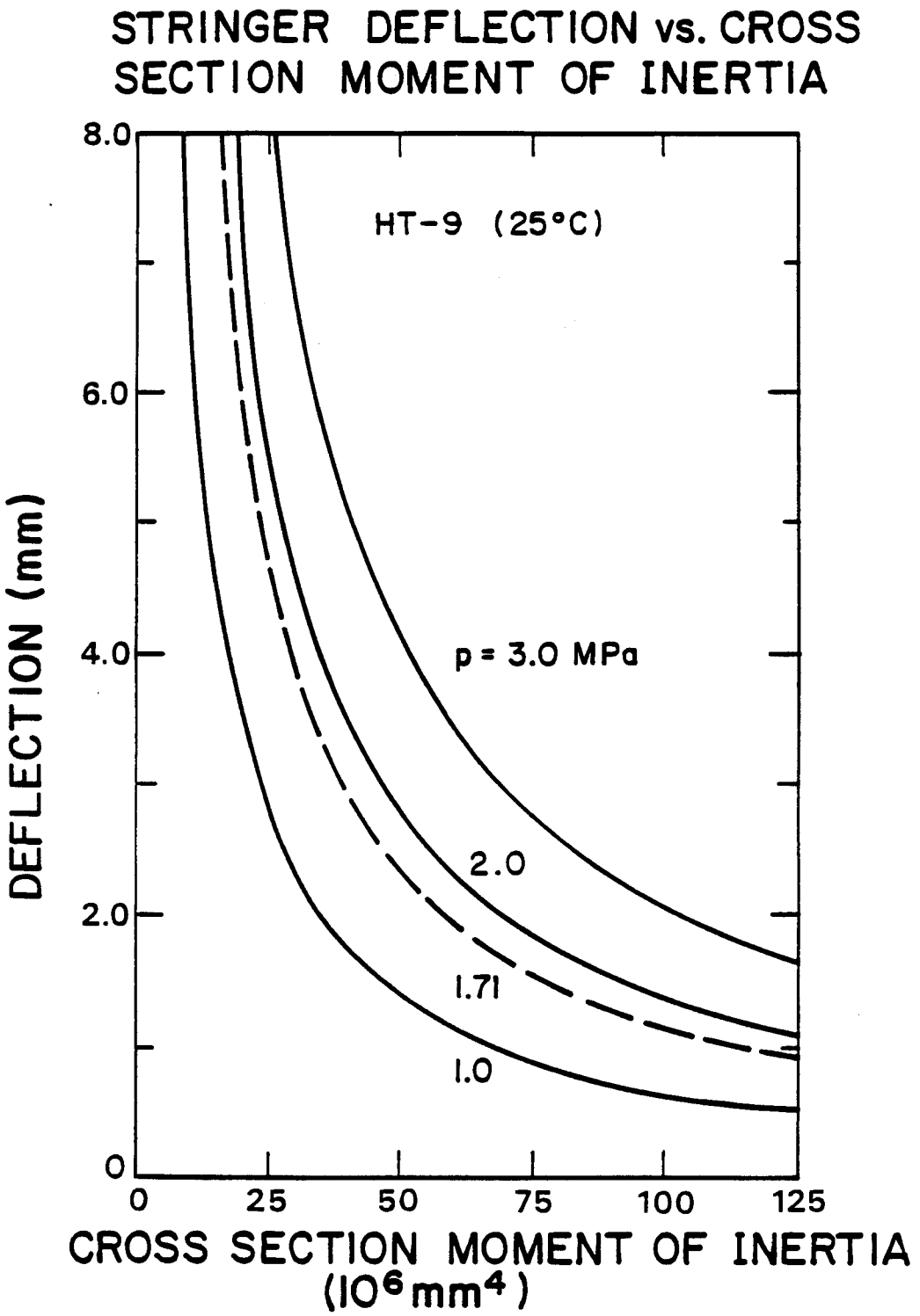
STRINGER DEFLECTION vs. CROSS SECTION MOMENT OF INERTIA
HT-9 (25°C)
p = 3.0 MPa
2.0
1.71
1.0
DEFLECTION (mm)
8.0
6.0
4.0
2.0
0
0
25
50
75
100
125
CROSS SECTION MOMENT OF INERTIA
(10⁶mm⁴)

Figure 3.8

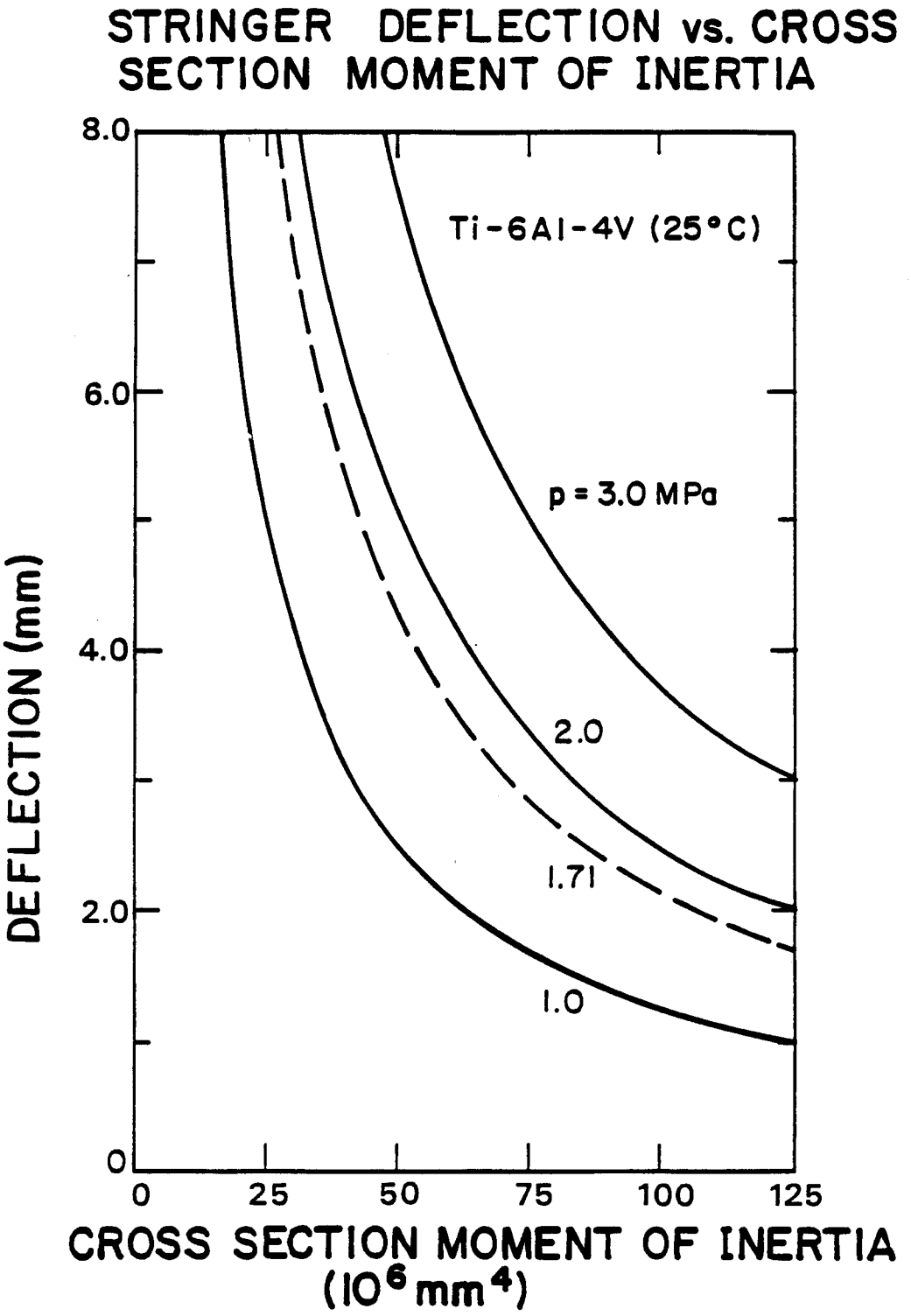
STRINGER DEFLECTION vs. CROSS SECTION MOMENT OF INERTIA
Ti-6Al-4V (25°C)
p = 3.0 MPa
2.0
1.71
1.0
DEFLECTION (mm)
8.0
6.0
4.0
2.0
0
0
25
50
75
100
125
CROSS SECTION MOMENT OF INERTIA
(10⁶ mm⁴)

Figure 3.9

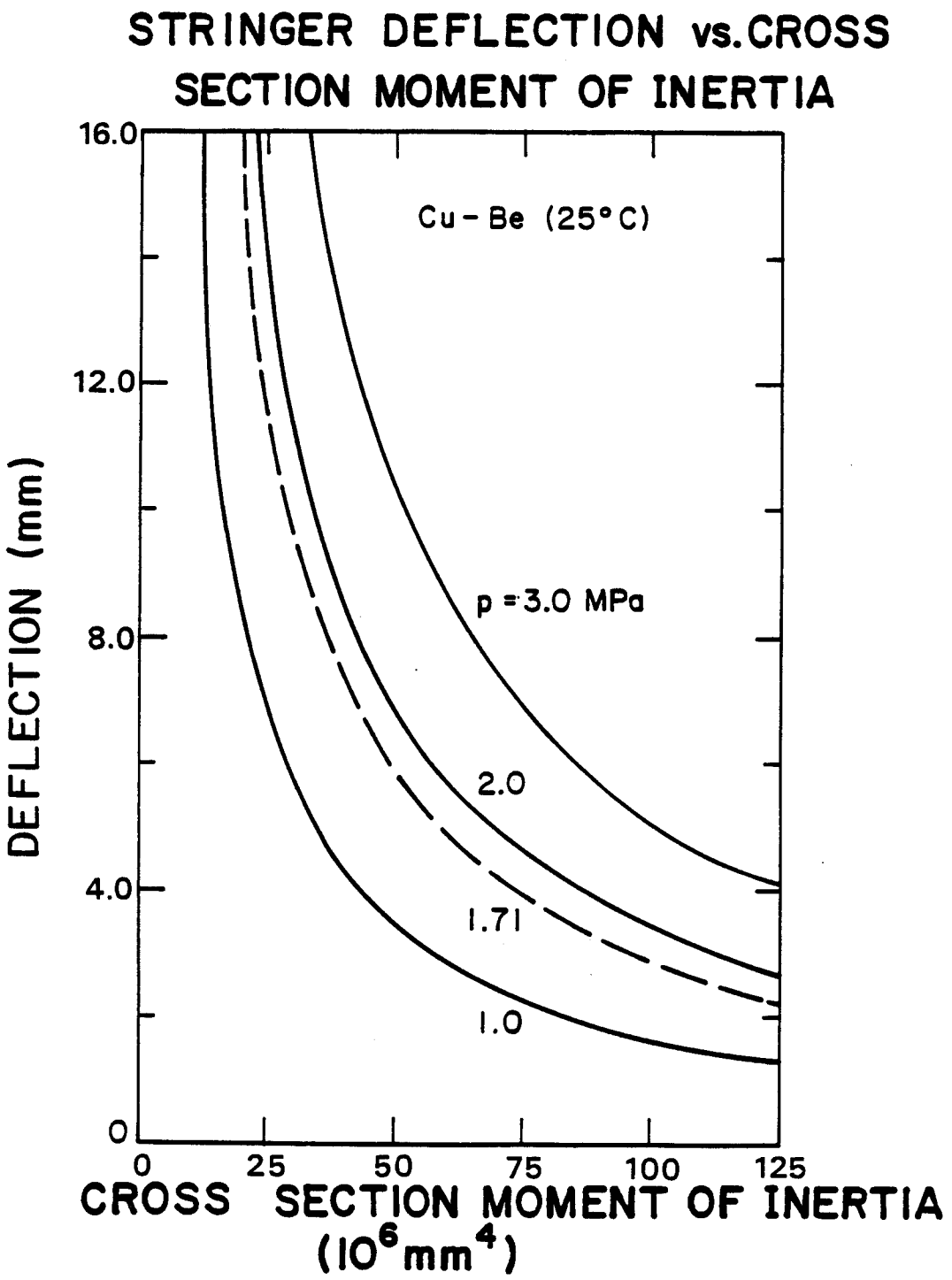
STRINGER DEFLECTION vs.CROSS SECTION MOMENT OF INERTIA
Cu - Be (25°C)
p = 3.0 MPa
2.0
1.71
1.0
DEFLECTION (mm)
16.0
12.0
8.0
4.0
0
0
25
50
75
100
125
CROSS SECTION MOMENT OF INERTIA
(10^6 mm^4)

Figure 3.10

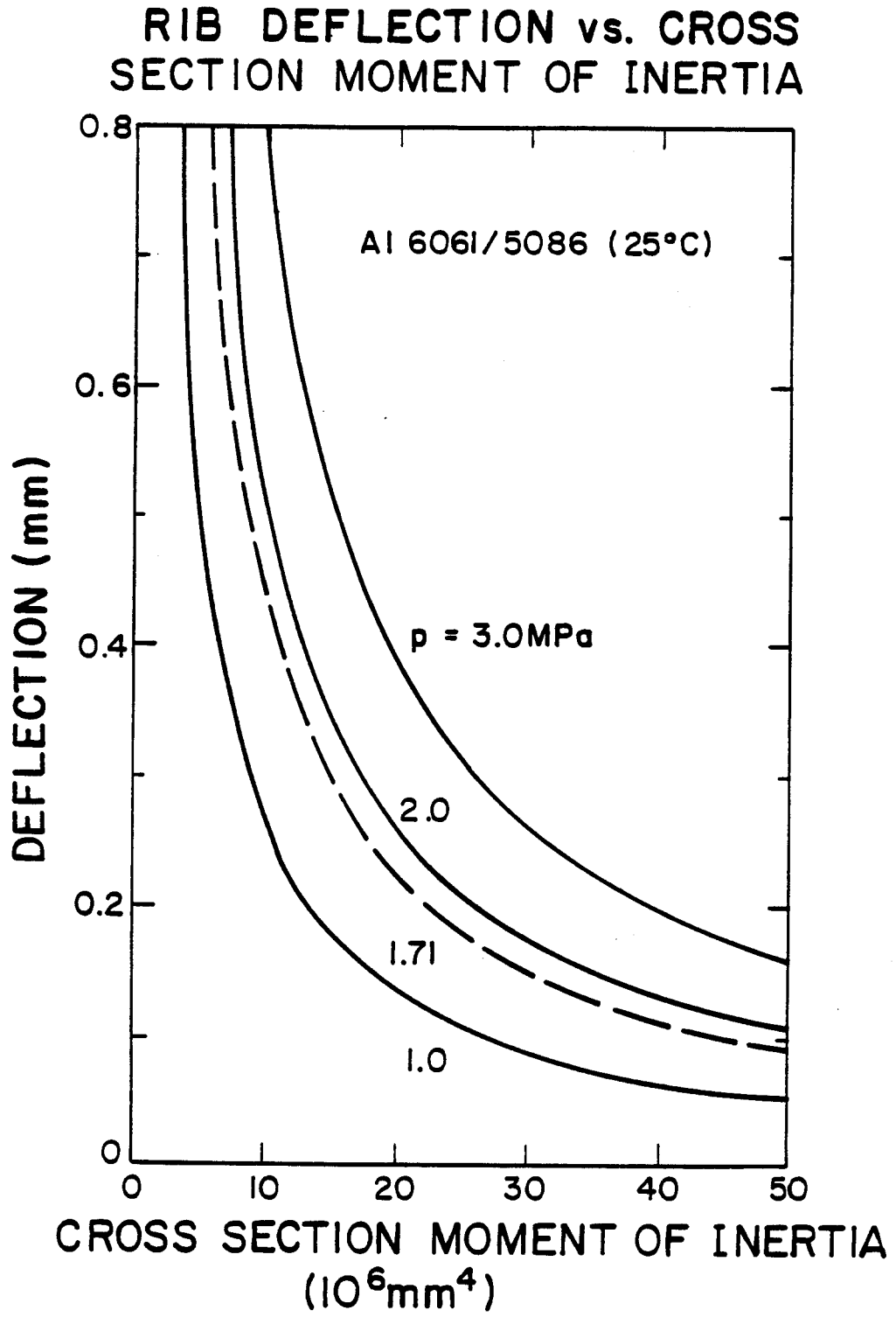
RIB DEFLECTION vs. CROSS SECTION MOMENT OF INERTIA
Al 6061/5086 (25°C)
p = 3.0MPa
2.0
1.71
1.0
DEFLECTION (mm)
0.8
0.6
0.4
0.2
0
0
10
20
30
40
50
CROSS SECTION MOMENT OF INERTIA
(10⁶mm⁴)

Figure 3.11

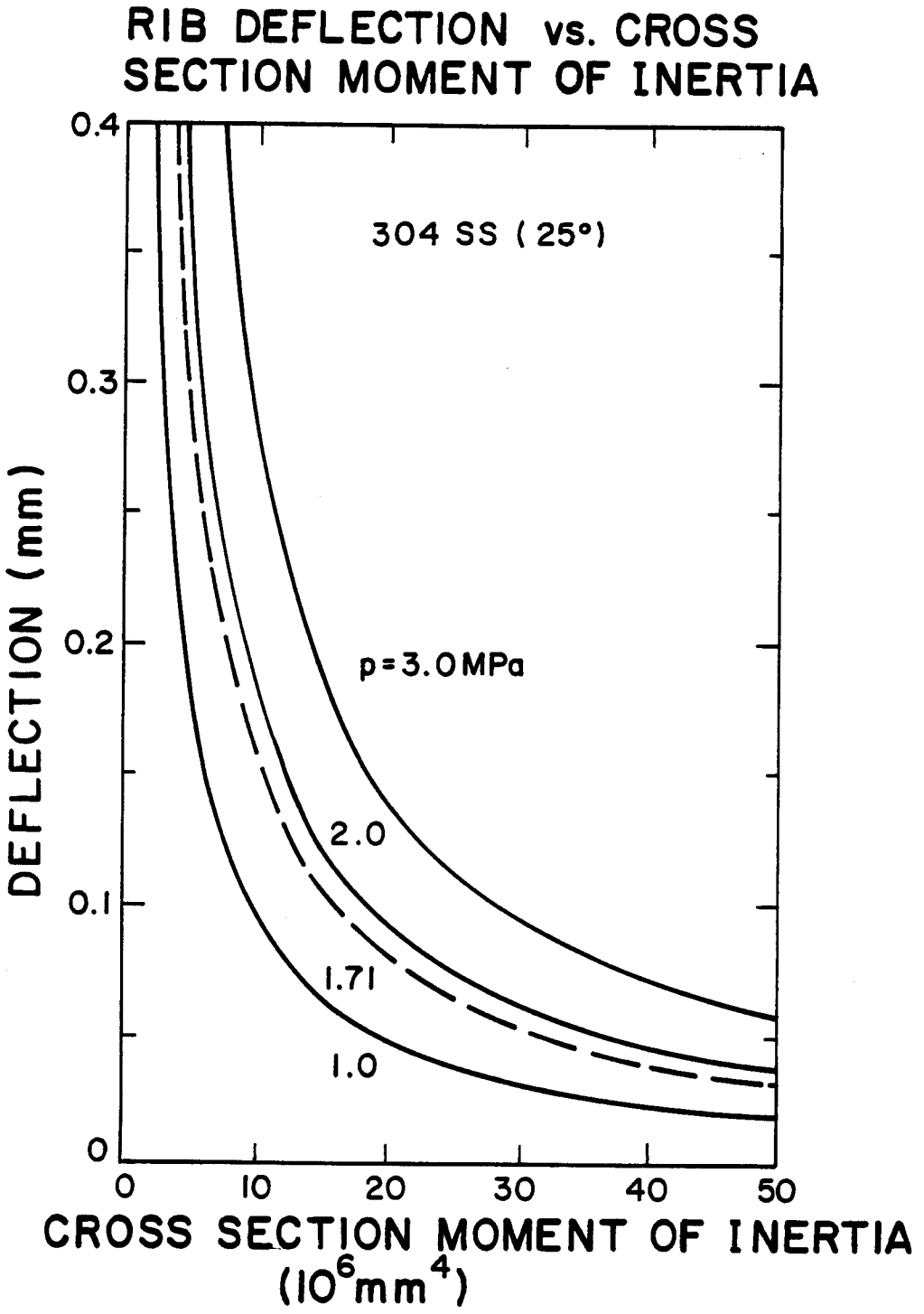
RIB DEFLECTION vs. CROSS SECTION MOMENT OF INERTIA
304 SS (25°)
p=3.0MPa
2.0
1.71
1.0
DEFLECTION (mm)
0.4
0.3
0.2
0.1
0
0
10
20
30
40
50
CROSS SECTION MOMENT OF INERTIA
(10^6mm^4)

Figure 3.12

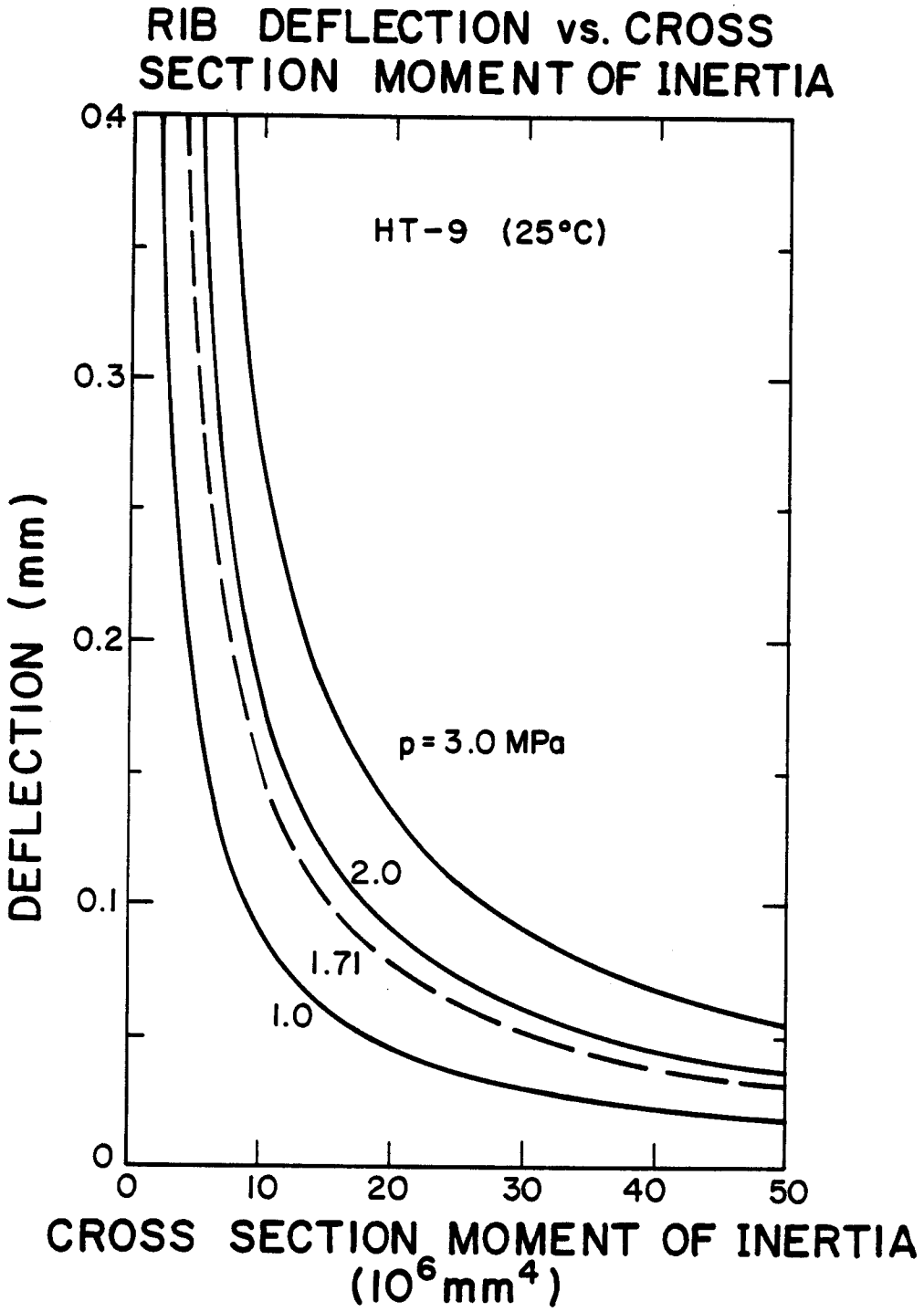
RIB DEFLECTION vs. CROSS SECTION MOMENT OF INERTIA
HT-9 (25°C)
p = 3.0 MPa
2.0
1.71
1.0
DEFLECTION (mm)
0.4
0.3
0.2
0.1
0
0
10
20
30
40
50
CROSS SECTION MOMENT OF INERTIA
(10^6 mm^4)

Figure 3.13

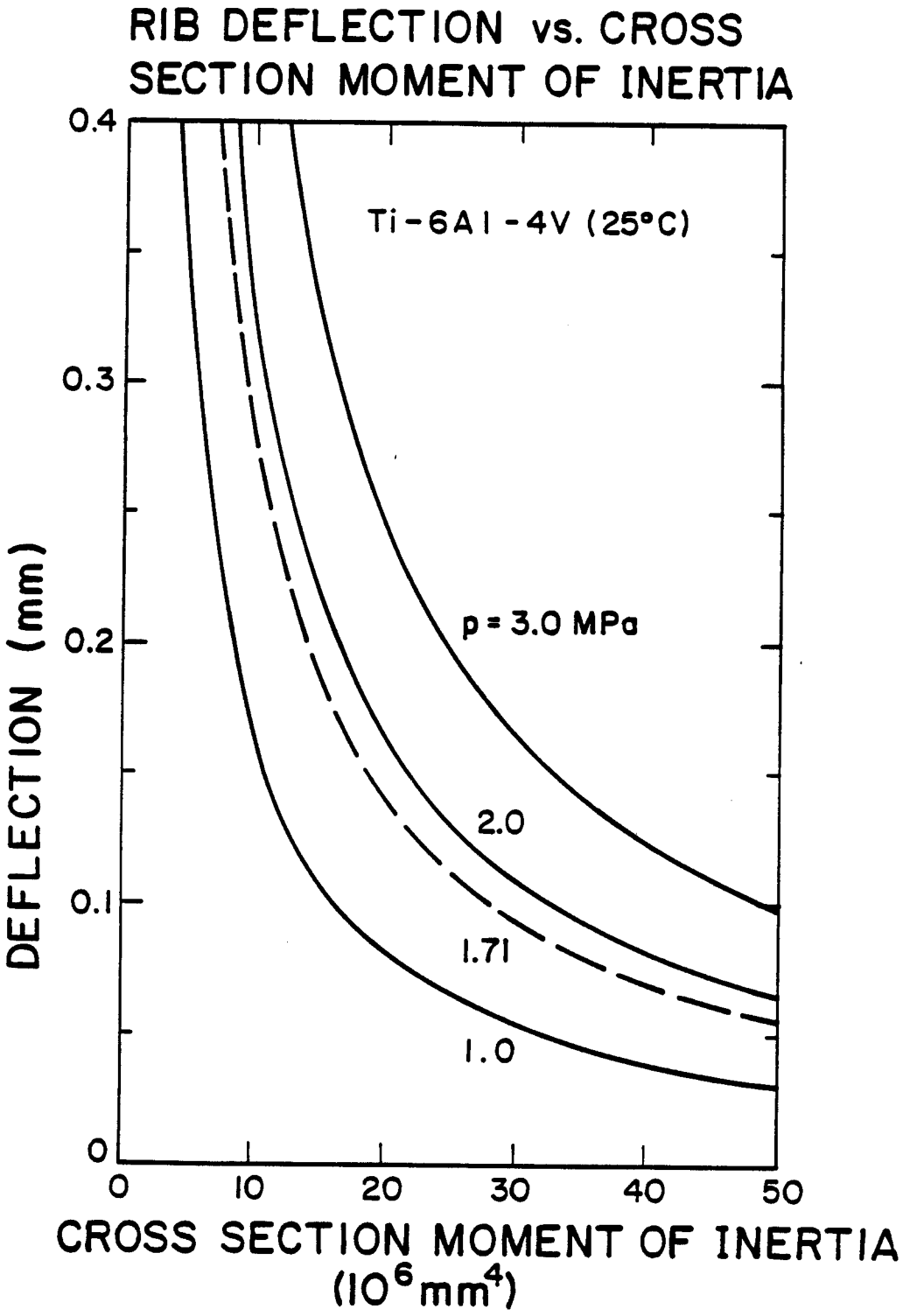
RIB DEFLECTION vs. CROSS SECTION MOMENT OF INERTIA
Ti-6Al-4V (25°C)
p = 3.0 MPa
2.0
1.71
1.0
DEFLECTION (mm)
0.4
0.3
0.2
0.1
0
0
10
20
30
40
50
CROSS SECTION MOMENT OF INERTIA
(10^6 mm^4)

Figure 3.14

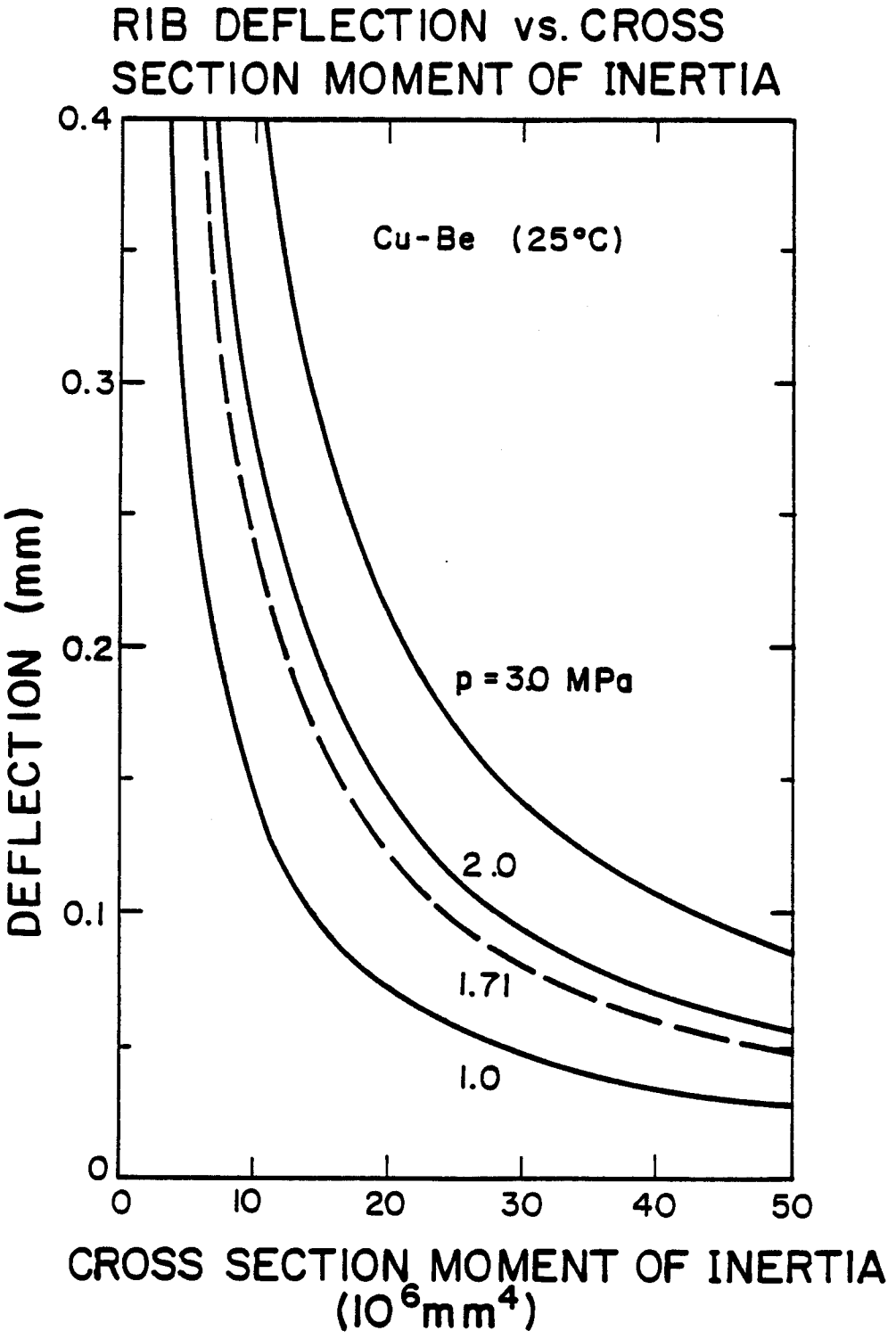
RIB DEFLECTION vs. CROSS SECTION MOMENT OF INERTIA
Cu-Be (25°C)
p = 3.0 MPa
2.0
1.71
1.0
DEFLECTION (mm)
0.4
0.3
0.2
0.1
0
0
10
20
30
40
50
CROSS SECTION MOMENT OF INERTIA
(10⁶mm⁴)

Figure 3.15

TABLE 3.1 Structural Frame Design Example
Aℓ6061; Overpressure 1.71 MPa

		STRINGER		RIB	
1. Structural Tubing Dimensions from AISC Manual (in.)		8x6x1/2	7x5x1/2	8x3x3/8	7x4x3/8
2. Cross Section Parameters from AISC Manual	I-in^4 (10^6mm^4)	103.0 (42.9)	63.5 (26.4)	51.0 (21.2)	44.0 (18.3)
	S-in^3 (10^3mm^3)	25.8 (422.8)	18.1 (296.6)	12.7 (208.1)	12.6 (206.5)
	r-in. (mm)	2.89 (73.4)	2.48 (63.0)	2.64 (67.0)	2.45 (62.2)
3. Static Response from Design Curves	ω-Hz	330	284	5465	5073
	DLF	0.65	0.58	1.27	1.34
	σ_s-MPa	391	558	187	189
	y_s-mm	7.94	12.9	0.21	0.24
4. Dynamic Response	σ_d-MPa	254	324	238	253
	O.K.?	Yes	No	Yes	Yes
	y_d-mm	5.16	7.5	0.27	0.32
	O.K.?	Yes	Yes	Yes	Yes

CONCEPTUAL FIRST WALL
STRUCTURAL SYSTEM

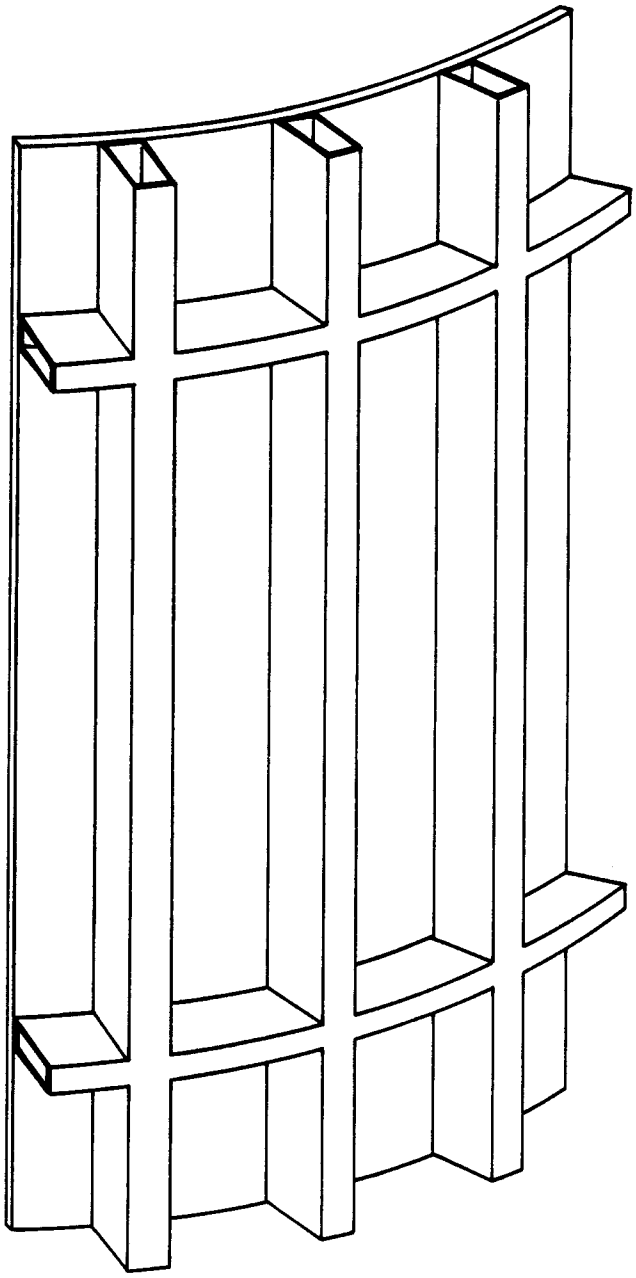

Figure 3.16

3.5 References

1. Moses, G. A., et al., Target Development Facility Progress Report to Sandia National Laboratories (November 1980).
2. Lovell, G. A., et al., "Transient Elastic Stresses in ICF Reactor First Wall Structural Systems," UWFDM-421, University of Wisconsin (August 1981).
3. Engelstad, R. L. and Lovell, E. G., "First Wall Mechanical Design for Light Ion Beam Fusion Reactors," UWFDM-322, University of Wisconsin (December 1979).

Section 4

A. Low Density Cavity Gas Fireball Dynamics in the Light Ion Beam Target Development Facility

In this section we have reproduced UWFDM-442 -- which is the paper presented at the 9th Symp. on Engin. Problems of Fusion Research, October 1981, Chicago, IL -- on our low pressure cavity gas fireball calculations. These calculations serve as input to the first wall mechanical and thermal response.

LOW DENSITY CAVITY GAS FIREBALL DYNAMICS IN THE LIGHT ION BEAM TARGET DEVELOPMENT FACILITY

R.R. Peterson, K.J. Lee, G.A. Moses
University of Wisconsin
1500 Johnson Drive
Madison, WI 53706

First wall survivability is a critical problem in the design of Inertial Confinement Fusion reactor cavities. Previous studies have shown that in a Light Ion Beam Fusion Reactor scenario, a bare, actively cooled ferritic steel first wall protected by a 50 Torr argon and sodium cavity gas will not experience excessively large stresses and could survive for the lifetime of the reactor. A Target Development Facility to be completed in the late 1980's would have higher target yields and less gas protection than the LIFR.

Recent calculations of wall stresses show that in a TDF, thermal stresses are much larger than mechanical stresses and that the maximum total stress is considerably larger than the yield stress for the ferritic steel. It is proposed that a graphite fabric liner be inserted on the inside edge of the cavity wall to reduce the total stresses in the wall to below the yield stress.

Introduction

First wall survivability has been an important concern in Inertial Confinement Fusion (ICF) reactor designs.[1-4] Designs of Light Ion Beam Fusion Reactors (LIFR)[5] can be different from other fusion reactor designs in that the reactor cavities are most probably filled with a gas at a pressure of between 5 and 50 Torr (when measured at 0°C). In such designs, this gas serves as a medium for the formation of plasma discharge channels which form renewable electrical connections for guiding the ion beams from the pulsed power drivers to the fusion target. This gas, if its atomic number is larger than 10, stops the soft component ($h\nu \lesssim 1$ keV) of the target generated X-rays and all of the ion debris. Only the hard X-rays directly reach the first wall but they should not cause serious damage because their deposition lengths are long. The fraction of the non-neutronic target energy absorbed by the gas will, however, heat the gas and generate a fireball. This fireball can propagate to the first wall, depositing a shock overpressure and a radiant heat flux. Critical problems in the analysis of LIFR designs are the determination of this overpressure and heat flux and the calculation of the resulting mechanical and thermal stresses in the first wall structures.

Specifically, in a study conducted by Sandia Labs and the University of Wisconsin, the survivability of a bare, actively cooled, ferritic steel first wall in a LIFR has been considered.[6] The gas, xenon or argon with an alkali metal vapor impurity, is chosen to permit laser guided formation of beam plasma channels and adequate protection of the reactor first wall. First wall stresses have been found to be acceptably low for 100 MJ target explosions in a 50 Torr argon gas in a 4 meter radius right circular cylindrical cavity.

The Target Development Facility (TDF), having many features in common with a LIFR, has been proposed to follow PBFA II and would begin operations in the late 1980's. Being a machine to be used in experiments, the number of explosions expected in its lifetime is much lower than in the LIFR ($\sim 10^4$ compared with 10^9). The radius of the cavity has been lowered to 3 meters in view of the reduced number of explosions. Also, the expected target yield has been increased to 200 MJ and the argon gas densities of most interest have been changed to 10 and 20 Torr. Additionally, xenon has been included as a possible cavity gas.

The heat fluxes, overpressures and the resulting stresses on the first wall of such a TDF are calculated with methods given in the following section. The results of these calculations for the TDF wall are presented for 10, 20 and 50 Torr of argon with a 0.2% sodium impurity and for 5 to 50 Torr of xenon with a 0.5% cesium impurity. The stresses on the walls are larger than in the LIFR and a change in the design of the TDF is proposed as a solution to the problem.

Analysis of Fireball and Stresses

To calculate the dynamics of the fireball and the overpressure and heat flux on the first wall of the TDF, it is necessary to first determine the opacity and the Equation of State (EOS) of the cavity gas. This is done with the MIXER computer code.[7] The atomic physics of a monatomic gas is modeled by assuming either that the average ionization state follows the Saha formalism and that the six most populous ionization states have densities spread about the average in a Gaussian or that the ionization follows the Coronal model where the densities of ionization states obey Boltzmann statistics. The choice of model is made on the basis of which recombination mechanisms are important at the given gas temperature and density. The first 20 atomic energy levels are included where their populations are assumed to obey Boltzmann's law. Once the EOS of the gas has been calculated, the Rosseland and Planck opacities are calculated considering photo-ionization, inverse Bremsstrahlung, atomic line absorption and Thompson scattering as photon stopping mechanisms.[8]

This analysis shows that, as long as one considers photons with energies greater than the first ionization potential, photo-ionization is the dominant mechanism of photon stopping. When the photon energy drops below this energy, the absorption coefficient drops by several orders of magnitude so that the gas is relatively transparent to low energy photons. An inert gas like argon with a high value for the first ionization energy will be transparent to much higher energy photons than an alkali metal vapor like sodium. Thus, the addition of a small amount of sodium will not significantly change the opacity of the gas to higher energy photons but will greatly increase the opacity to low energy photons. Thus, when the photons are of low energy, increasing amounts of alkali metal vapor rapidly increase the photon stopping ability of gas.

Once the optical properties of the gas are known, the physics of the fireball propagation may be studied.[9] The argon or xenon will absorb target generated X-rays and ion debris in a small volume, creating a hot fireball at the center of the cavity which is surrounded by cold gas. Initially, the radiation mean free paths are long in the fireball but short in the cold gas so that a wave of heat moves into the cold gas by successive warming of layers of gas near the fireball. Initially, this heating wave, whose speed decreases with decreasing fireball temperature,

propagates more rapidly than the sound speed. As the fireball expands and cools, the speed of the heating wave drops to the speed of sound and a shock wave is formed which breaks away from the fireball. The fireball continues expanding and cooling until the mean free paths for fireball radiation in the cold gas are longer than the distance to the first wall, at which time the fireball begins radiating its energy to the wall. This continues until the fireball cools to the point where the emission of photons by the gas sharply decreases and the flow of radiant energy ceases. The effect of decreasing the mean free paths to low energy photons in the cold gas is to slow the propagation of the radiation to the wall. Thus, by adjusting the opacity through the variations in the alkali metal concentration, one may control the total amount of heat radiated to the wall per explosion and the rate at which this heat reaches the wall.

A hydrodynamic radiative transfer computer code, FIRE, has been used to simulate this behavior in fireballs.[10] FIRE is a one-dimensional hydrodynamics code that calculates the dynamics of two fluids; the plasma at its own temperature and the radiation at its own temperature. The transport of the radiation fluid is flux limited and upstream averaged. The equation of state of the plasma and mean free paths of radiation in the gas are read from tables of data provided by the atomic physics code MIXER.

Once the heat fluxes and overpressures have been found, the thermal and mechanical stresses are calculated. A simple temperature diffusion computer code is used to find the temperature profiles in the first wall at various times. These temperature profiles are put into the transient stress code TSTRESS[11] to calculate the thermal stresses in the wall. The mechanical stresses, due to the shock overpressure induced flexures in the first wall structures, are then calculated analytically and combined with the thermal stresses.[12]

Results

Using the FIRE radiation hydrodynamics code, the heat flux and overpressure on a first wall 3 meters from a 200 MJ exploding pellet are calculated. Cavity gases of argon with 0.2% by volume of sodium and of xenon with 0.5% by volume of cesium are considered. The calculations are started by assuming that 60 MJ of the 200 MJ target yield is in soft X-rays and ions which are stopped in a small sphere of gas surrounding the target. A typical heat flux and overpressure are shown in Fig. 1, which is the case of a 20 Torr argon cavity gas. Previously reported calculations have shown how the heat flux and overpressure are dependent on the fractions of alkali metal vapor[6], but here we will vary the gas density only.

A temperature diffusion code and the transient stress code TSTRESS have been used to calculate thermal stresses in the wall. With the analytically calculated flexural mechanical stress, the thermal stress and the total stress are plotted in Fig. 2 for a 20 Torr argon and sodium cavity gas. In this figure, positive stresses are compressive. Here, the wall is a system of HT-9 panels 47 centimeters wide, 2 meters high and 5 centimeters thick, which are rigidly supported by a frame at the edges of the panels. Also shown in Fig. 2 is the yield stress for HT-9.[13] Notice that, because of the large thermal stress, the total stress is larger than the yield stress. This means the material may deform before reaching this stress.

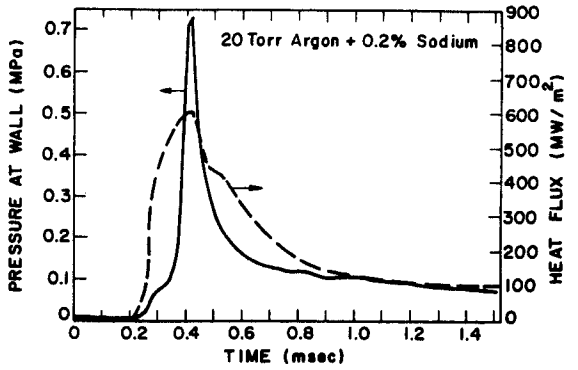

Figure 1 Heat flux and overpressure at first wall versus time. The wall is 3 meters from the target.

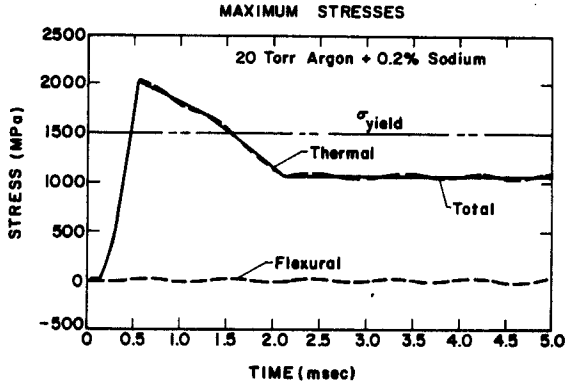

Figure 2 Maximum stresses in 5 cm thick HT-9 wall panel versus time. The wall panel is 2 meters high and 47 cm wide.

Calculations like those described above have been carried out for both argon with sodium and xenon with cesium cavity gases for gas pressures between 5 and 50 Torr (when measured at 0°C). The results of these calculations are tabulated in Table 1. The maximum shock overpressure on the first wall is plotted against gas pressure in Fig. 3. There is little difference between argon and xenon. Also on Fig. 3, these values are compared with the overpressure predicted by strong shock theory.[8] The overpressures are much below the strong shock values because a large fraction of the fireball energy is radiated out of the blast wave to the first wall. The overpressure decreases with decreasing gas density because the amount of radiated energy is higher at low gas densities. Figure 4 shows the energy radiated to the wall per unit area per target explosion plotted against gas density. The values are normalized to the total initial fireball energy divided by the wall surface area, 53 J/cm^2, which is what would occur if there was no cavity gas. Naturally, the amount of radiated energy decreases as

Table 1. Results of Computer Calculations

Wall Radius = 3 m
Initial Energy of Fireball = 60 MJ
Wall Material = HT-9

Panel Thickness = 5 cm
Panel Height = 2 m
Panel Span = 47 cm

Type of Gas	Argon			Xenon			
Gas Pressure (Torr)	10	20	50	5	10	20	50
Max. Overpressure at First Wall (MPa)	0.25	0.79	1.16	0.089	0.18	0.69	1.33
Max. Heat Flux at First Wall (kW/cm^2)	135	53	30	422	177	92	19
Energy Density Radiated to First Wall (J/cm^2)	28.93	24.62	21.18	41.04	34.28	25.75	18.9
Max. Temperature Rise at First Wall (°C)	1321	716	407	2430	1498	640	232
Max. Total Stress at First Wall (MPa)	3236	2050	1207	6262	4368	1919	691

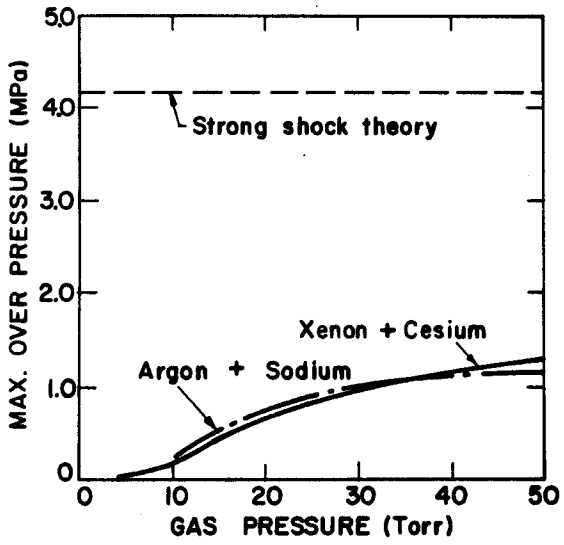

Figure 3 Maximum overpressure versus gas density compared with strong shock over pressure.

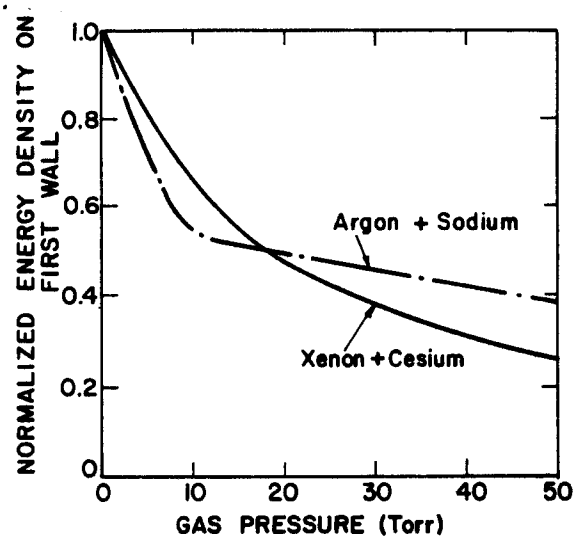

Figure 4 Energy density on first wall versus gas density. The energy density is normalized to 53 J/cm^2, the non-neutronic target yield divided by the first wall surface area.

more gas is put in between the target and the first wall. Figure 5 shows the maximum stress plotted against gas density and the yield stress for HT-9. Notice that only when the gas density is higher than 30 Torr for xenon or 35 Torr for argon does the stress remain below the yield stress.

Conclusions

We have found, because of the reduction in gas protection, that the heat fluxes on the first wall of the proposed TDF are large enough to cause large thermal stresses in a bare HT-9 first wall. These stresses are often larger than the yield stress of HT-9 and make the determination of the lifetime of the first wall difficult. On the one hand, since the maximum stresses are compressive, it might be argued that the stresses actually impede crack growth and lengthen the lifetime. On the other hand, with the stresses being larger than the yield stress, the material under compression may deform to reduce those stresses but leave the wall under tension when the heat flux is removed. This could lead to accelerated crack growth and a reduced wall lifetime.

We propose avoiding this uncertainty in the wall lifetime by changing the design of the first wall. We could suggest that the cavity gas density be increased but the beam channels may not be possible if the gas is

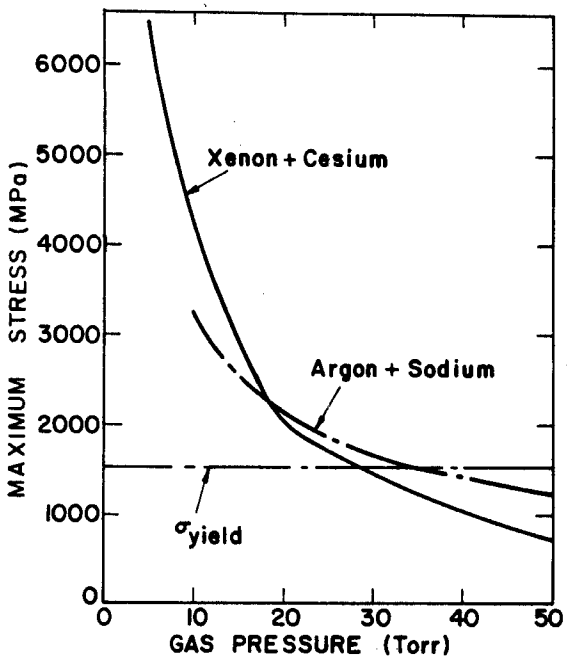

Figure 5 Maximum first wall stress versus gas density compared with yield stress.

dense enough to protect the wall. Since the shock overpressure is not large, we feel that a graphite liner supported by the HT-9 wall could survive the mechanical effects and would protect the HT-9 from the large thermal stresses. The liner would absorb the radiant heat flux and radiate the energy to the steel wall over a long period of time, generating only small thermal stresses in the HT-9. The liner would be constructed of a graphite fabric that would rest against and transmit the mechanical impulse of the shock to the steel wall. We feel that, since the mechanical stresses are so much lower than the thermal stresses, and since this design does not depend upon complicated calculations of the behavior of the first wall material, this is a better choice for the first wall construction of the TDF than the bare steel wall.

Acknowledgement

This work was supported by Sandia Laboratory under contract DE-AS08-81DP40161.

References

1. Lawrence Livermore Laboratory Laser Fusion Annual Report - 1978, UCRL-50021-78.

2. R.W. Conn et al., "SOLASE - A Conceptual Laser Fusion Reactor Design," University of Wisconsin Fusion Engineering Program Report UWFDM-220 (December 1977).

3. E.W. Sucov, "Inertial Confinement Fusion Central Station Electrical Power Generating Plant," DOE/DP/40086-1 (Feb. 1981).

4. B. Badger et al., "HIBALL - A Conceptual Heavy Ion Beam Driven Fusion Reactor Study," University of Wisconsin Fusion Engineering Program Preliminary Report UWFDM-450 (June 1981).

5. D.L. Cook et al., "Light Ion Driven Inertial Fusion Reactor Concepts," Proc. of the 4th Topical Mtg. on the Technology of Controlled Nuclear Fusion, King of Prussia, PA, Oct. 14-17, 1980, pp. 1386-1394.

6. R.R. Peterson, G.A. Moses, and G.W. Cooper, "Cavity Gas Analysis for Light Ion Beam Fusion Reactors," Nuclear Technology/Fusion 1, 377 (July 1981).

7. R.R. Peterson and G.A. Moses, "MIXER - A Multi-Species Optical Data and Equation of State Computer Code," University of Wisconsin Fusion Engineering Program Report UWFDM-372 (Sept. 1980).

8. Ya. B. Zeldovich and Yu. P. Raizer, Physics of Shock Waves and High Temperature Hydrodynamic Phenomena (Academic Press, New York, 1967).

9. Detailed discussion of the physics of fireballs may be found in G.A. Moses and R.R. Peterson, "First Wall Protection in Particle Beam Fusion Reactors by Inert Cavity Gases," Nuclear Fusion 20, 849 (1980).

10. G.A. Moses and R.R. Peterson, "FIRE - A Computer Code to Simulate Cavity Gas Response to Inertial Confinement Target Explosions," University of Wisconsin Fusion Engineering Program Report UWFDM-336 (Jan. 1980).

11. R.R. Peterson, R.D. Watson, W.G. Wolfer, and G.A. Moses, "TSTRESS - A Transient Stress Computer Code," University of Wisconsin Fusion Engineering Program Report UWFDM-382 (Dec. 1980).

12. E.G. Lovell, R.R. Peterson, R.L. Engelstad, and G.A. Moses, "Transient Elastic Stresses in ICF Reactor First Wall Structural Systems," 2nd Topical Mtg. on Fusion Reactor Materials, August 9-12, 1981, Seattle, WA.

13. T.A. Lechtenberg, "The Effects of Microstructure on the Mechanical Properties of a Commercial 12 Cr-1 Mo Steel (HT-9)," General Atomic Company Report GA-A16389 (August 1981).

B. Model Development

In this section we describe the FIRE computer code including the modifications made by Tom McCarville. We have added the capability of target x-ray attenuation in the cavity gas and calculation of the resultant temperature distribution. We can also model the stopping of target ions in the gas and simultaneously compute the response of the gas. The ion stopping is included as source terms in the conservation of momentum and energy equations.

The description is the first part of UWFDM-407, which is a code description and user's manual. The detailed user's information has not been included in this progress report.

Improvements in the FIRE Code for Simulating the Response of a Cavity Gas to Inertial Confinement Fusion Target Explosions

T.J. McCarville

R.R. Peterson

G.A. Moses

Fusion Engineering Program
Nuclear Engineering Department
University of Wisconsin
Madison, WI 53706

June 1981

(Revised February 1982)

UWFDM-407

Table of Contents

FIRE - A CODE FOR COMPUTING THE RESPONSE OF AN INERTIAL CONFINEMENT FUSION CAVITY GAS TO A TARGET EXPLOSION

Thomas J. McCarville, Robert R. Peterson, and Gregory A. Moses
Department of Nuclear Engineering, University of Wisconsin, Madison, WI, USA

PROGRAM SUMMARY

Title of program: FIRE

Catalogue number:

Program obtainable from: CPC Program Library, Queen's University of Belfast, Northern Ireland (see application form in this issue)

Computer: Univac 1110; **Installation:** MACC, University of Wisconsin, Madison, Wisconsin

Operating System: Univac 1110 EXEC VIII

Programming language used: FORTRAN

High speed storage required: 60,045 words

No. of bits in a word: 36

Overlay structure: none

No. of magnetic tapes required: none

Other peripherals used: line printer, up to ten mass storage files or magnetic tapes

No. of cards in combined program and test deck:

Card punching code: EBCDIC

Keywords: inertial confinement fusion reactor design, gas protection concept, deposition of target x-rays, deposition of target debris, cavity gas response

Nature of the physical problem:
One of the methods that has been suggested for protecting the first wall of a commercial inertial confinement fusion (ICF) reactor from the x-rays and ions emitted by an exploding target is to fill the cavity with a gas [1]. The FIRE code described in this article simulates the interaction of the target x-rays and ions with the gas, and computes the response of the gas to a target explosion. The results computed by the FIRE code are useful for analyzing the thermal and mechanical response of a first wall that is protected with a cavity gas.

Method of solution:
The deposition of target x-rays into the gas is computed with an exponential attenuation model. A table of x-ray attenuation coefficients for atoms with

atomic numbers ranging from 1 to 100 and x-ray energies ranging from 0.01 keV to 1 MeV are supplied with this version of the code [2]. The initial x-rays that are absorbed ionize the gas near the target, and reduce the photoelectric attenuation coefficient for subsequent x-rays. The x-ray deposition model used by the FIRE code accounts for the reduction in the attenuation coefficient with increasing ionization [3].

The internal energy and momentum transferred from the target debris to the gas is computed from the results of an ion transport code. The results of the ion transport code are fit to analytic functions, and these analytic functions are used to estimate the rates that internal energy and momentum are deposited as a function of time and space [3].

The FIRE code simulates the response of a cavity gas to the deposition of target x-rays and ions by solving differential equations of energy and momentum conservation. These equations are solved in the Lagrangian reference frame by finite difference methods. A tabulated equation of state and tabulated Planck and Rosseland mean free paths are needed to compute the response of the gas. The MIXER code [4] has been developed to compute this data for the FIRE code. The TSTRESS code [5] then uses the heat fluxes and overpressures at the first wall computed by FIRE to analyze the response of the first wall.

Restrictions on the complexity of the problem:
The FIRE code assumes one-dimensional symmetry in computing the interaction of the target x-rays and ions with the gas, and also in computing the gas response. The cavity gas can be divided into a maximum of 97 Lagrangian zones, and either planar, cylindrical, or spherical geometry can be assumed.

The gas is assumed to be composed of only one atomic number in computing the x-ray deposition. At present, the model for computing the reduction in the photoelectric attenuation coefficient with increasing ionization is only used if the gas is neon, argon, or xenon. To compute the reduction in the attenuation coefficient for additional gases, the energy of the K, L, and M shells of the neutral gas and the number of electrons in each shell must be added to the subroutine EDATA.

Typical running time:
The CPU time required to compute the deposition of target x-rays and ions into the gas is minimal compared to the time required to compute the gas response. On the Univac 1110, the CPU time required to compute the gas response is about 2×10^{-3} s/zone/cycle.

Unusual features of the program:
The FIRE code is written in standard FORTRAN except for the manner in which the COMMON blocks are used. The COMMON blocks are listed only at the beginning of the program, where they are equated to INCLUDE statements. Thereafter, the INCLUDE statements are used to represent the COMMON blocks. The use of INCLUDE statements abbreviates the listing of a program that uses the same COMMON blocks in many subroutines, because an INCLUDE statement occupies only one line, whereas a COMMON block might occupy many lines. INCLUDE statements only have meaning to a Univac compiler, so the user may wish to replace them with the respective COMMON blocks.

References:

[1] R.W. Conn et al., "SOLASE: A Conceptual Laser Fusion Reactor Design," University of Wisconsin Fusion Engineering Program Report UWFDM-220 (Dec. 1977).

[2] K.G. Adams and F. Biggs, "Efficient Computer Access to Sandia Photon Cross Sections," Sandia Lab., SC-RR-72-0683, Albuquerque, NM (Dec. 1973).

[3] T.J. McCarville, G.A. Moses, and G.L. Kulcinski, "A Model for Depositing Inertial Confinement Fusion X-Rays and Pellet Debris into a Cavity Gas," University of Wisconsin Fusion Engineering Program Report UWFDM-406 (April 1981).

[4] R.R. Peterson and G.A. Moses, "MIXER - A Multi-Species Optical Data and Equation of State Computer Code," (see this issue).

[5] R.R. Peterson, R.D. Watson, W.G. Wolfer, and G.A. Moses, "TSTRESS - A Transient Stress Computer Code," (see this issue).

I. Introduction

One of the methods that has been suggested for protecting the first wall of a commercial inertial confinement fusion reactor from the x-rays and ions emitted by an exploding target is to fill the cavity with a gas [1]. The x-ray and ion energy is attenuated by the gas and converted to hydrodynamic and internal energy, whereas the neutrons emitted by the target are unaffected by the gas. The energy of the gas can then be transferred through heat exchangers to a working fluid.

If the gas protection concept is to be a viable method of protecting the first wall from target x-rays and ions, then the gas must be dense enough to attenuate the target x-rays and ions without degrading driver beam propagation, and the first wall must be capable of withstanding the response of the gas. The FIRE code has been developed to help determine whether these criteria can be met. The code simulates the interaction of the target x-rays and ions with the gas, as well as the gas response. The output of the code can be used to compute the thermal response of the first wall to blackbody radiation emitted by the gas and unattenuated target x-rays and ions. The results can also be used to compute the mechanical response of the first wall to gas motion [2]. The thermal and mechanical response of the first wall can then be used to estimate the first wall lifetime.

This documentation describes the equations solved by the FIRE code and the numerical methods used to solve these equations. Some of the physical models used by the code are unique, such as the two temperature radiation diffusion model, but the development of these models has been documented elsewhere and will not be repeated here.

II. Target X-Ray Deposition

The time required for the deposition of target x-rays into the cavity gas ($\sim 10^{-8}$ s) is much shorter than the hydrodynamic response time, so the gas is stationary as the x-rays are deposited. Hence, the thermodynamic state of the gas after x-ray deposition can be used as an initial condition in computing the gas response to the exploding target. The code assumes exponential x-ray attenuation, which should be adequate for most target x-ray spectra [3]. As the code is presently written, gases composed of only one element can be used to attenuate the x-rays. A table of attenuation coefficients for elements with atomic numbers ranging from 1 to 100 and x-ray energies ranging from 0.01 to 1000 keV are provided with the FIRE code [4].

The initial x-rays that are photoabsorbed by the gas reduce the number of bound electrons available to interact with subsequent x-rays, so the attenuation coefficient decreases as x-rays are deposited. A method of modifying the photoelectric attenuation coefficient of the gas to account for increasing ionization has been developed for the FIRE code [3]. By counting the number of electrons ejected from each electron shell as the x-rays are deposited, the contribution to the photoelectric attenuation coefficient from each shell can be reduced by an amount proportional to the number of missing electrons. Although simple, this model does at least give the correct attenuation for the limiting cases of a completely neutral and completely ionized atom. The accuracy of this model at intermediate levels of ionization has not been determined. In this version of the FIRE code, the model for computing the reduction in photoelectric absorption can only be used with neon, argon or xenon gas. To extend the model to other gases, the number of electrons in each

shell of the neutral atom and the energies of the K, L, and M shells must be added to the EDATA subroutine.

The x-ray spectrum emitted by the target can be assumed to be Planckian, or an arbitrary histogram can be input. In either case, the code divides the x-ray spectrum into energy groups, giving each group a constant energy width. The x-rays in each group are then attenuated as if they were monoenergetic.

III. The Equation of Motion

THe equations solved by the FIRE code are written in the Lagrangian coordinate system, meaning the equations describe a point that moves with the local fluid velocity. The advantage of this coordinate system is that the mass flux is zero, so the conservation equations are simplified considerably. The FIRE code automatically chooses a suitable Lagrangian mesh from the cavity geometry and dimensions input by the user. Either planar, cylindrical, or spherical coordinates can be assumed. The units used by the FIRE code are

length	- cm
time	- second
mass	- gram
speed	- cm/s
energy	- Joule
temperature	- eV
pressure	- J/cm^3
charge	- esu

Figure 1 illustrates the index system used to denote spatial boundaries. The Lagrangian mass of each zone, $m_{o_{j-1/2}}$, is defined by integrating

$$\partial m_o = \rho(r)\, r^{\delta-1}\, dr \qquad (1)$$

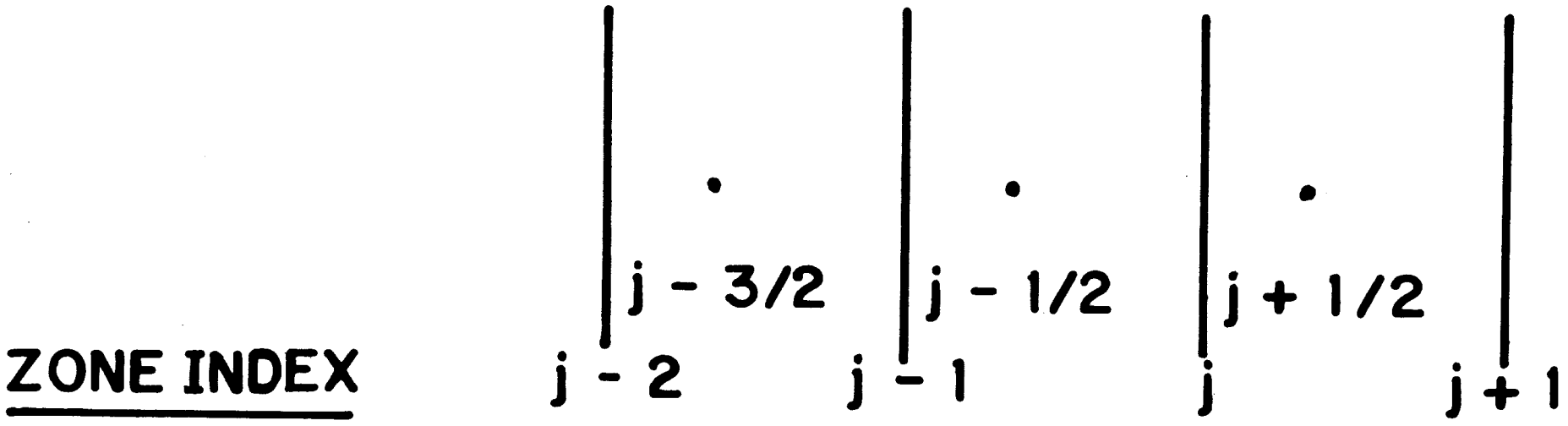

Figure 1. The index system used to denote spatial boundaries.

from boundary j to j+1, where ρ is the mass density and r is the spatial coordinate. The symbol δ denotes planar (δ=1), cylindrical (δ=2), or spherical coordinates (δ=3). The Lagrangian mass is a constant for each zone, so it is a convenient replacement for the product $\rho(r)r^{\delta-1}dr$ when writing the conservation equations in finite difference form. The average Lagrangian mass of two zones, m_{o_j}, will appear in the finite difference form of the equation of motion, and is defined as

$$m_{o_j} = \frac{(m_{o_{j+1/2}} + m_{o_{j-1/2}})}{2} \quad . \tag{2}$$

In Lagrangian coordinates, the equation of motion is

$$\frac{\partial u}{\partial t} = -V \frac{\partial}{\partial r}(P + q) - \frac{V}{V_d}\frac{\partial u_{dr}}{\partial t} \quad , \tag{3}$$

where: V is the specific volume of the gas,

V_d is the specific volume of the debris,

u is the radial velocity of the gas,

u_{dr} is the radial velocity of the debris,

P is the sum of the gas and radiation pressure,

q is the artificial viscosity [5].

The explicit, finite difference form of Eq. (3) that is solved by the FIRE code is

$$\frac{u_j^{n+1/2} - u_j^{n-1/2}}{\Delta t^n} = -\frac{(r_j^n)^{\delta-1}[\Delta P_j^n + \Delta q_j^{n-1/2}]}{\Delta m_{o_j}} - \frac{1}{G\Delta m_{o_j}}\frac{\Delta MOM_j^n}{\Delta t^n} \quad , \tag{4}$$

where: G = 1 for δ=1 (planar coordinates),

$G = 2\pi$ for $\delta=2$ (cylindrical coordinates),

$G = 4\pi$ for $\delta=3$ (spherical coordinates),

and ΔMOM_j^n is the momentum lost by the debris during Δt^n.

The superscript n is the time index. The terms in brackets are defined as

$$\Delta P_j^n = P_{j+1/2}^n - P_{j-1/2}^n \quad \text{and} \quad \Delta q_j^{n-1/2} = q_{j+1/2}^{n-1/2} - q_{j-1/2}^{n-1/2} \; . \tag{5}$$

The artificial viscosity is a function of the zone specific volume, so to make Eq. (4) explicit, Δq_j is evaluated at $t^{n-1/2}$. The artificial viscosity used in the FIRE code is

$$\begin{aligned} q_{j-1/2}^{n-1/2} &= 0 && \text{for } \dot{V}_{j-1/2}^{n-1/2} > 0 \; , \\ &= \frac{\sqrt{2}\,(u_j^{n-1/2} - u_{j-1}^{n-1/2})}{V_{j-1/2}^{n-1/2}} && \text{for } \dot{V}_{j-1/2}^{n-1/2} < 0 \; . \end{aligned} \tag{6}$$

The quantity $\dot{V}$ is the time rate of change of the specific volume.

The gas pressure, P_p, is computed from the perfect gas law,

$$P_{P_{j\pm1/2}}^n = 1.602 \times 10^{-19} \, (1 + Z_{j\pm1/2}^n) * n_{P_{j\pm1/2}}^n * T_{P_{j\pm1/2}}^n \; , \tag{7}$$

where: Z is the charge state of the gas,

n_p is the number density of gas atoms,

T_p is the gas temperature.

The radiation pressure, P_R, is computed from the radiation energy density, E_R, by

$$P^n_{R_{j\pm1/2}} = \frac{1}{3}\left(\frac{E_R}{V}\right)^n_{j\pm1/2} \quad , \tag{8}$$

where the radiation energy density has been assumed to be isotropic. Although in some instances the radiation field may not be isotropic, the radiation pressure is very small compared to the gas pressure for the temperature and densities of interest here, so the assumption of an isotropic radiation field does not affect the gas motion.

After solving Eq. (4) for $u_j^{n+1/2}$, the new radii are computed from

$$r_j^{n+1} = r_j^n + u_j^{n+1/2}\ \Delta t^{n+1/2} \quad . \tag{9}$$

New specific volumes and other quantities are then computed in preparation for the next time step.

To evaluate the momentum imparted by the target debris, the debris is assumed to consist of only one element. The initial energy spectrum can be assumed to be Maxwellian or Gaussian, or an arbitrary histogram can be input. The code divides the initial energy spectrum into energy groups that have equally spaced increments in velocity, and assigns an equal fraction of the debris mass to each group. The total momentum deposited into a gas zone is the sum of the contributions from each group. However, to simplify the notation in the equations that follow, the index denoting the energy group will be omitted. The momentum imparted by the debris, in finite difference form, is

$$\Delta MOM^n_j = \Delta m^n_{d_{j-1/2}}\ (u^{n+1/2}_{dr} - u^{n-1/2}_{dr}) \quad . \tag{10}$$

The quantity $\Delta m^n_{d_{j-1/2}}$ is the debris mass in zone j-1/2, and is evaluated from analytic functions that are programmed into the FIRE code [3]. The analytic functions simulate ion transport in the gas. The quantities $u^{n\pm1/2}_{dr}$ are the average radial speed of ions in an energy group, so are independent of the spatial index. Equation (10) can be written in the form evaluated by the FIRE code by noting that at time $t^{n+1/2}$,

$$u^{n+1/2}_{dr} = u^{n-1/2}_{dr} + \left(\frac{du_{dr}}{dt}\right)^{n-1/2} \Delta t^n \quad . \tag{11}$$

The time derivative u_{dr} has been written as a total derivative because the average deceleration of each energy group is independent of the spatial index. The deceleration is also evaluated from the analytic expressions that are programmed into the FIRE code. Combining Eqs. (10) and (11) gives the expression evaluated in the code,

$$\Delta MOM^n_j = \Delta m^n_{d_{j-1/2}} \left(\frac{du_{dr}}{dt}\right)^{n-1/2} \Delta t^n \quad . \tag{12}$$

The analytic expressions that are programmed into the FIRE code and used to evaluate the deceleration and spatial distribution of the debris are functions of the average radial distance that the debris travel through the gas, r_d. From the expression

$$u^{n+1/2}_{dr} = \frac{r^{n+1}_d - r^n_d}{\Delta t^{n+1/2}} \quad , \tag{13}$$

and Eq. (11), the distance the debris have traveled through the gas (in the Lagrangian reference frame), is

$$r_d^{n+1} = r_d^n + \Delta t^{n+1/2}\, u_{dr}^{n-1/2} + \left(\frac{du_{dr}}{dt}\right)^{n-1/2} \Delta t^n \Delta t^{n+1/2} \quad . \tag{14}$$

When computing the distance traveled by the debris in the Eularian reference frame, the gas motion is accounted for.

IV. The Energy Equations

Because of the high temperatures encountered in the cavity gas (up to tens of eV), thermal radiation can be the dominant energy transport mechanism. The FIRE code uses flux limited diffusion to model radiation transport. The absorption and emission of thermal radiation are strongly temperature dependent, so the radiation diffusion equation is solved simultaneously with the temperature equation. The equations solved by the FIRE code are

$$C_v \frac{\partial T_P}{\partial t} = \frac{\partial}{\partial m_o}\left(r^{\delta-1} K_P \frac{\partial T_P}{\partial r}\right) - \frac{\partial P_P}{\partial T_P} \dot{V} T_P - q\dot{V} + \omega_R E_R - \omega_P T_P + S \tag{15-a}$$

$$\frac{\partial E_R}{\partial t} = \frac{\partial}{\partial m_o}\left(r^{\delta-1} K_R \frac{\partial E_R}{\partial r}\right) - \frac{\rho E_R}{3} \dot{V} \qquad - \omega_R E_R + \omega_P T_P \tag{15-b}$$

where: C_v is the specific heat at constant volume,

K_P is the gas thermal conductivity,

K_R is the radiation thermal conductivity,

ω_R is the radiation absorption coefficient,

ω_P is the radiation emission coefficient,

S is the rate that internal energy is added by the debris.

In writing Eq. (15-a), the thermodynamic identity [6]

$$\frac{\partial E_P}{\partial t} + P_P \dot{V} = C_v \frac{\partial T_P}{\partial t} + \frac{\partial P_P}{\partial T_P} \dot{V} T_P \tag{16}$$

was used to replace $\frac{\partial E_P}{\partial t}$ and $P_P \dot{V}$ with terms involving T_p. To simplify the notation in the finite difference equations that follow, the time index of quantities evaluated at $t^{n+1/2}$ will be omitted. In fully implicit finite difference form, Eqs. (15-a) and (15-b) are

$$C_{v_{j-1/2}} \frac{T_{P_{j-1/2}}^{n+1} - T_{P_{j-1/2}}^{n}}{\Delta t^{n+1/2}} = \frac{1}{\Delta m_{o_{j-1/2}}} \left[\frac{r_j^{\delta-1}}{\left(\frac{\Delta r}{K_P}\right)_j} \left(T_{P_{j+1/2}}^{n+1} - T_{P_{j-1/2}}^{n+1}\right) \right.$$

$$\left. - \frac{r_{j-1}^{\delta-1}}{\left(\frac{\Delta r}{K_P}\right)_{j-1}} \left(T_{P_{j-1/2}}^{n+1} - T_{P_{j-3/2}}^{n+1}\right) \right] - \left(\frac{\partial P_P}{\partial T_P}\right)_{j-1/2} \dot{V}_{j-1/2} T_{P_{j-1/2}}^{n+1} \qquad (17\text{-a})$$

$$- q_{j-1/2} \dot{V}_{j-1/2} + \omega_{R_{j-1/2}} E_{R_{j-1/2}}^{n+1} - \omega_{P_{j-1/2}} T_{P_{j-1/2}}^{n+1} + S_{j-1/2}^{n}$$

and

$$\frac{E_{R_{j-1/2}}^{n+1} - E_{R_{j-1/2}}^{n}}{\Delta t^{n+1/2}} = \frac{1}{\Delta m_{o_{j-1/2}}} \left[\frac{r_j^{\delta-1}}{\left(\frac{\Delta r}{K_R}\right)_j + \frac{\Delta E_{R_j}}{F_{R_j}}} \left(E_{R_{j+1/2}}^{n+1} - E_{R_{j-1/2}}^{n+1}\right) \right.$$

$$\left. - \frac{r_{j-1}^{\delta-1}}{\left(\frac{\Delta r}{K_R}\right)_{j-1} + \frac{\Delta E_{R_{j-1}}}{F_{R_{j-1}}}} \left(E_{R_{j-1/2}}^{n+1} - E_{R_{j-3/2}}^{n+1}\right) \right] - E_{R_{j-1/2}}^{n+1} \frac{\dot{V}_{n-1/2}}{3V_{j-1/2}} \qquad (17\text{-b})$$

$$- \omega_{R_{j-1/2}} E_{R_{j-1/2}}^{n+1} + \omega_{P_{j-1/2}} T_{P_{j-1/2}}^{n+1} .$$

The denominators of the terms in brackets represent the resistance per unit area to thermal and radiative diffusion between zone centers. For instance,

$$\left(\frac{\Delta r}{K_P}\right)_j = \frac{1}{2}\left(\frac{r_{j-1} - r_j}{K_{P_{j+1/2}}} + \frac{r_j - r_{j-1}}{K_{P_{j-1/2}}}\right) \quad , \tag{18}$$

and so on for $\left(\frac{\Delta r}{K_P}\right)_{j-1}$, $\left(\frac{\Delta r}{K_R}\right)_j$, and $\left(\frac{\Delta r}{K_R}\right)_{j-1}$. Equations (17-a) and (17-b) can be written in matrix form as

$$\underline{\alpha}_{j-1/2}\left(\underline{\theta}^{n+1}_{j-1/2} - \underline{\theta}^{n}_{j-1/2}\right) = \underline{a}_j\left(\underline{\theta}^{n+1}_{j+1/2} - \underline{\theta}^{n+1}_{j-1/2}\right) - \underline{a}_{j-1}\left(\underline{\theta}^{n+1}_{j-1/2} - \underline{\theta}^{n-1}_{j-3/2}\right) \tag{19}$$

$$- \underline{\gamma}_{j-1/2}\,\underline{\theta}^{n+1}_{j-1/2} - \underline{\omega}_{j-1/2}\,\underline{\theta}^{n+1}_{j+1/2} + \underline{\beta}_{j-1/2} \quad .$$

where

$$\underline{\alpha}_{j-1/2} = \begin{pmatrix} C_{v_{j-1/2}} & 0 \\ 0 & 1 \end{pmatrix} \frac{\Delta m_{o_{j-1/2}}}{\Delta t^{n-1/2}} \quad ,$$

$$\underline{a}_j = \begin{pmatrix} r_j^{\delta-1}/(\Delta r/K_P)_j & 0 \\ 0 & r_j^{\delta-1}/((\Delta r/K_R)_j + \Delta E_{R_j}/F_{R_j}) \end{pmatrix} \quad ,$$

$$\underline{\gamma}_{j-1/2} = \begin{pmatrix} (\partial P_P/\partial T_P)_{j-1/2}\dot{V}_{j-1/2} & 0 \\ 0 & \dot{V}_{j-1/2}/3V_{j-1/2} \end{pmatrix} \Delta m_{o_{j-1/2}} \quad ,$$

$$\underline{\omega}_{j-1/2} = \begin{pmatrix} \omega_P & -\omega_R \\ -\omega_P & \omega_R \end{pmatrix}_{j-1/2} \Delta m_{o_{j-1/2}} \quad ,$$

$$\underline{\beta}_{j-1/2} = \begin{pmatrix} -q_{j-1/2}\,\dot{V}_{j-1/2} + S^{n}_{j-1/2} \\ 0 \end{pmatrix} \Delta m_{o_{j-1/2}} \quad ,$$

and $$\underline{\theta}^{n+1}_{j-1/2} = \begin{pmatrix} T^{n+1}_{P_{j-1/2}} \\ E^{n+1}_{R_{j-1/2}} \end{pmatrix} .$$

A more compact matrix equation can be written by redefining the coefficients as follows:

$$\underline{\underline{A}}_{j-1/2} = \underline{\underline{a}}_{j} \quad , \quad .$$

$$\underline{\underline{B}}_{j-1/2} = \underline{\underline{\alpha}}_{j-1/2} + \underline{\underline{a}}_{j} + \underline{\underline{a}}_{j-1} + \underline{\underline{\gamma}}_{j-1/2} + \underline{\underline{\omega}}_{j-1/2} \quad ,$$

$$\underline{\underline{C}}_{j-1/2} = \underline{\underline{a}}_{j-1} \quad ,$$

$$\underline{D}_{j-1/2} = \underline{\underline{\alpha}}_{j-1/2}\,\underline{\theta}^{n}_{j-1/2} + \underline{\beta}_{j-1/2} \quad .$$

With these redefinitions, Eq. (19) becomes

$$-\underline{\underline{A}}_{j-1/2}\,\underline{\theta}^{n+1}_{j+1/2} + \underline{\underline{B}}_{j-1/2}\,\underline{\theta}^{n+1}_{j-1/2} - \underline{\underline{C}}_{j-1/2}\,\underline{\theta}^{n+1}_{j-3/2} = \underline{D}_{j-1/2} \quad . \qquad (20)$$

If JMAX is the number of zone boundaries, then Eq. (20) represents a JMAX by JMAX tridiagonal matrix equation that has two by two matrices for elements. If the coefficients of Eq. (20) are evaluated at t^n, it can be solved by

Gaussian elimination. Solutions can be shown to be of the form [7]

$$\underline{\theta}^{n+1}_{j-1/2} = \underline{\underline{E}}_{j-1/2}\,\underline{\theta}^{n+1}_{j+1/2} + \underline{F}_{j-1/2} \quad , \quad \text{for } 1 \leq j < \text{JMAX}$$

$$\theta^{n+1}_{\text{JMAX}+1/2} = \text{BOUNDARY CONDITIONS} \quad , \quad \text{for } j = \text{JMAX} \quad . \tag{21}$$

The $\underline{\underline{E}}$ matrix and $\underline{F}$ vector can be related to known quantities by decreasing the spatial index of Eq. (21) by one, and substituted into Eq. (20). One finds that

$$\underline{\underline{E}}_j = (\underline{\underline{B}}_{j-1/2} - \underline{\underline{C}}_{j-1/2} * \underline{\underline{E}}_{j-3/2})^{-1} * \underline{\underline{A}}_{j-1/2} \quad ,$$

and

$$\underline{F}_{j-1/2} = (\underline{\underline{B}}_{j-1/2} - \underline{\underline{C}}_{j-1/2} * \underline{\underline{E}}_{j-3/2})^{-1} * (\underline{D}_{j-1/2} + \underline{\underline{C}}_{j-1/2} * \underline{F}_{j-3/2}) \tag{22}$$

for $1 \leq j < \text{JMAX}$, and

$$\underline{\underline{E}}_{1/2} = (\underline{\underline{B}}_{1/2})^{-1} * \underline{\underline{A}}_{1/2} \quad ,$$

$$\underline{F}_{1/2} = (\underline{\underline{B}}_{1/2})^{-1} * \underline{D}_{1/2} \quad ,$$

for j=1. To solve Eq. (21), a sweep is made from the first zone out to the wall to evaluate $\underline{\underline{E}}$ and $\underline{F}$, and then back to the center to evaluate the components of the $\underline{\theta}^{n+1}$ vector.

The expression for the thermal conductivity of the gas, K_p, that is used in the FIRE code is the theoretical expression developed for electrons interaction with stationary ions [8]. The theoretical expression includes an

experimentally determined constant to prevent K_P from diverging as the average ionization state approaches zero. The expression is

$$K_P = 20 \left(\frac{2}{\pi}\right)^{3/2} \frac{T_P^{5/2}}{\sqrt{m_e}\, e^4 (Z + 4) \ln \Lambda} , \tag{23}$$

where: e is the electron charge,

m_e is the electron mass,

$\ln \Lambda$ is the Coulomb logarithm.

To save computational effort, the Coulomb logarithm is computed from a curve fit that has an accuracy better than 10% for $\ln \Lambda$ greater than 5. In finite difference form, the thermal conductivities are

$$\begin{aligned} K_{P_{j\pm1/2}} &= \frac{1.22 \times 10^2 \, T_{P_j}^2 \, T_{P_{j\pm1/2}}^{1/2}}{(4 + Z_{j\pm1/2}) \ln \Lambda_{j\pm1/2}} , \\ K_{P_{j-3/2}} &= \frac{1.22 \times 10^2 \, T_{P_{j-1}}^2 \, T_{P_{j-3/2}}^{1/2}}{(4 + Z_{j-3/2}) \ln \Lambda_{j-3/2}} . \end{aligned} \tag{24}$$

The T_P^2 terms are evaluated at the zone boundaries rather than the zone centers to enhance the numerical stability of the solution.

The expression for the radiation conductivity that is used in the FIRE code is a frequency averaged value. If the radiation mean free path is much smaller than the gradients in the radiation energy density, then the frequency dependent radiation flux, $q_{R\nu}$, is given by [9]

$$q_{R\nu} = \frac{\ell_\nu(T_P)\, c}{3V} \frac{\partial E_{R\nu}}{\partial r} , \tag{25}$$

where: ℓ_ν is the frequency dependent radiation mean free path,

$E_{R\nu}$ is the frequency dependent radiation specific energy,

c is the speed of light.

The frequency averaged conductivity is arrived at by integrating Eq. (25) over frequency. The frequency dependence of ℓ_ν is known from theoretical models of radiation absorption, but in general the frequency dependence of $E_{R\nu}$ is not known prior to solving the frequency dependent radiation transport equations. For the radiation diffusion model used in the FIRE code, the frequency dependence of $E_{R\nu}$ is assumed to be a dilute Planckian, that is

$$E_{R\nu} = \varepsilon V \frac{8\pi h\nu^3}{c^3} \frac{1}{\exp\left(\frac{h\nu}{T_R}\right) - 1} \quad , \tag{26}$$

where ε is a proportionality factor and T_R is the radiation temperature. The radiation temperature is defined so as to reflect the temperature of the gas that emitted the radiation occupying the point of interest. The radiation temperature at a point is evaluated by averaging the temperature of the transported radiation, the temperature of the emitted radiation, and the temperature of the radiation already present. In finite difference form, this average is

$$T^{n+1}_{R_{j+1/2}} = \frac{W_1 * T^{n+1/2}_{R_{j-1/2}} + W_2 * T^{n+1/2}_{R_{j+3/2}} + W_3 * T^{n+1/2}_{P_{j+1/2}} + W_4 * T^{n+1/2}_{R_{j+1/2}}}{W_1 + W_2 + W_3 + W_4} \qquad 1 \leq j < JMAX \tag{27}$$

where the weighting functions are defined as

$$W_1 = \left(\frac{q_R r^{\delta-1}\Delta t}{\Delta m_o}\right)^{n+1/2}_{j-1/2} \qquad \text{if } q_{R_{j-1/2}} > 0$$

$$= 0 \qquad \text{if } q_{R_{j-1/2}} < 0 \tag{28}$$

$$W_2 = 0 \qquad \text{if } q_{R_{j+3/2}} > 0$$

$$= \left(\frac{q_R r^{\delta-1}\Delta t}{\Delta m_o}\right)^{n+1/2}_{j+3/2} \qquad \text{if } q_{R_{j+3/2}} < 0 \tag{29}$$

$$W_3 = (\omega_P T_P \Delta t)^{n+1/2}_{j+1/2} \tag{30}$$

$$W_4 = (E_R)^{n+1/2}_{j+1/2} \quad . \tag{31}$$

The frequency averaged radiation flux across zone boundaries is represented by q_R in Eqs (28) and (29), which after integrating Eq. (25) over frequency can be written as

$$q_R = -\frac{\ell(T_P,T_R)c}{3V}\frac{\partial E_R}{\partial r} \quad , \tag{32}$$

where

$$\ell(T_P,T_R) = \frac{15}{4\pi^4}\int_o^\infty \ell_\nu(T_P)\,\frac{U^4 e^{-U}}{(1-e^{-U})^2}\,dU \quad , \tag{33}$$

and

$$U(T_R) = \frac{h\nu}{T_R} \quad . \tag{34}$$

Equation (33) defines the Rosseland mean free path (including spontaneous emission [9]), and is a function of the gas density, the local gas temperature, and the local radiation temperature. From Eq. (32), the frequency averaged radiation conductivity can be written in finite difference form as

$$K_{R_{j\pm1/2}} = 10^{10} \frac{\ell_{j\pm1/2}}{V_{j\pm1/2}} \quad ,$$

$$K_{R_{j-3/2}} = 10^{10} \frac{\ell_{j-3/2}}{V_{j-3/2}} \quad . \tag{35}$$

If the Rosseland mean free path is larger than the spatial zoning, then radiation may stream from zone to zone without being absorbed. In this case the diffusion model overestimates the radiation flux, and must be modified with a flux limiter. The maximum radiation flux, $\frac{cE_R}{V}$, occurs when the radiation intensity of free streaming radiation approaches complete anisotropy. If the radiation intensity is completely isotropic, then the flux limit is $\frac{cE_R}{4V}$. This latter expression is used in the FIRE code. In finite difference form, the flux limit is .

$$F_j = 3.75 \times 10^9 \left[\left(\frac{E_R}{V}\right)^{n+1/2}_{j+1/2} + \left(\frac{E_R}{V}\right)^{n+1/2}_{j-1/2}\right] \qquad 1 < j < JMAX$$

$$F_{JMAX} = 7.5 \times 10^9 \left(\frac{E_R}{V}\right)^{n+1/2}_{JMAX+1/2} \qquad j = JMAX \quad . \tag{36}$$

The expression for the absorption coefficient used in the FIRE code can be arrived at by integrating the frequency dependent absorption rate over frequency. From the definition of the radiation mean free path, the frequency dependent absorption rate is

$$\omega_{R\nu} E_{R\nu} = \frac{cE_{R\nu}}{\ell_\nu(T_p)} \quad . \tag{37}$$

Using Eq. (26) to integrate Eq. (37) over frequency results in (including spontaneous emission)

$$\omega_R E_R = \frac{cE_R}{\ell_1(T_R,T_P)} \quad , \tag{38}$$

where

$$\frac{1}{\ell_1(T_P,T_R)} = \frac{15}{\pi^4} \int_0^\infty \frac{U^3(T_R)\, dU}{\ell_\nu(T_P)(e^{U(T_R)} - 1)} \quad , \tag{39}$$

and

$$U(T_R) = \frac{h\nu}{T_R} \quad . \tag{40}$$

Equation (39) defines the nonequilibrium Planck mean free path, which is the frequency averaged distance that radiation with a temperature T_R will travel in a gas at temperature T_P before being absorbed. The finite difference form of the absorption coefficient is

$$\omega_{R_{j-1/2}}^{n+1/2} = \frac{3 \times 10^{10}}{\ell_1(T_R,T_P)_{j-1/2}^{n+1/2}} \quad . \tag{41}$$

The expression for the radiation emission coefficient that is used in the FIRE code is arrived at by assuming that the gas is in local thermodynamic equilibrium (LTE) [10]. The gas is in LTE if the electrons and ions are in collisional equilibrium with each other. The radiation spectrum emitted by a gas in LTE has a Planckian frequency distribution, because the electron-ion recombination processes are the same as those that occur in a blackbody. Then the frequency dependent emission rate can be written as

$$\omega_{P\nu} T_P = \frac{cV}{\ell_\nu(T_P)} \frac{8\pi h\nu^3}{c^3} \frac{1}{\exp\left(\frac{h\nu}{T_P}\right) - 1} \quad . \tag{42}$$

Averaging Eq. (42) over frequency yields

$$\omega_P T_P = V \frac{4\sigma T_P^4}{\ell_1(T_P)} \quad , \tag{43}$$

where

$$\frac{1}{\ell_1(T_P)} = \frac{15}{\pi^4} \int_0^\infty \frac{U^3(T_P)\, dU}{\ell_\nu(T_P)(e^{U(T_P)} - 1)} \quad , \tag{44}$$

and

$$U(T_P) = \frac{h\nu}{T_P} \quad . \tag{45}$$

Equation (43) defines the equilibrium Planck mean free path, which is the average distance that radiation at a temperature T_P will travel in a gas at temperature T_P before being absorbed. The finite difference form of the emission rate is

$$\omega_{P_{j-1/2}}^{n+1/2} = 4.12 \times 10^5 \left[\frac{VT_P^3}{\ell_1(T_P)}\right]_{j-1/2}^{n+1/2} \quad . \tag{46}$$

An expression for the internal energy deposition rate from target debris can be arrived at by equating the decrease in debris kinetic energy to the increase in the kinetic and internal energy of the gas:

$$-\frac{1}{V_d} u_d \frac{\partial u_d}{\partial t} = \frac{S}{V} + \frac{u}{V} \left(\frac{\partial u}{\partial t}\right)_{P=0} \quad , \tag{47}$$

where u_d is the speed of the debris ions, and the quantity in parenthesis is the acceleration of the gas in the radial direction due to the debris alone, that is, excluding the pressure forces. From conservation of debris momentum it is clear that

$$\frac{1}{V} \left(\frac{\partial u}{\partial t}\right)_{P=0} = -\frac{1}{V_d} \frac{\partial u_{dr}}{\partial t} \quad . \tag{48}$$

Note that $u_{dr} < u_d$ if the trajectory of the debris ions is not straight as they slow down in the gas (such as when the ions scatter off the gas nuclei). Combining Eqs. (47) and (48) and solving for the internal energy source term gives

$$S = - \frac{V}{V_d} u_d \frac{\partial u_d}{\partial t} + \frac{V}{V_d} u \frac{\partial u_{dr}}{\partial t} \quad . \tag{49}$$

In finite difference form, Eq. (49) is

$$S^n_{j-1/2} = - \frac{\Delta m_{d_{j-1/2}}}{\Delta m_{o_{j-1/2}}} \frac{\Delta KE^n_{d_{j-1/2}}}{\Delta t^{n-1/2}} + \frac{u_d^{n+1/2}}{\Delta m_{o_{j-1/2}}} \frac{\Delta MOM^n_{j-1/2}}{\Delta t^{n+1/2}} \quad , \tag{50}$$

where ΔKE_d is the change in debris kinetic energy during Δt^n. The change in debris kinetic energy, the change in debris momentum, and the debris mass are all evaluated from the analytic functions stored in the FIRE code that simulate ion transport in the gas [3].

V. The Equation of State and Opacity Tables

There are five quantities that must be supplied in tabular form by the user of the FIRE code. These are

$Z(n_P,T_P)$	Charge State
$E_P(n_P,T_P)$	Specific Internal Energy
$C_v(n_P,T_P)$	Specific Heat
$\ell(n_P,T_P,T_R)$	Rosseland Mean Free Path
$\ell_1(n_P,T_P,T_R)$	Planck Mean Free Path

These tables are generated for FIRE by the MIXER code [11]. Logarithmic interpolation is used to interpolate between points in the tables. For instance, the charge state is stored as log $Z(\log n_p, \log T_p)$. In what follows, the indices associated with the dependent variables are

$$K - \log T_R \ ,$$

$$L - \log T_p \ ,$$

$$M - \log n_p \ .$$

Points in the two dimensional tables can be represented as a two-dimensional grid, as shown in Fig. 2. The indices with stars denote the location of a quantity located between points in the table, for instance log $Z(L^*,M^*)$. To compute the desired quantity we first interpolate along the M axis:

$$\log Z(L,M^*) = \log Z(L,M) + \frac{Z(L,M+1) - Z(L,M)}{n_p(M+1) - n_p(M)} * (n_p - n_p(M)) \ , \tag{51}$$

$$\log Z(L+1,M^*) = \log Z(L+1,M) + \frac{\log Z(L+1,M+1) - \log Z(L+1,M)}{n_p(M+1) - n_p(M)} * (n_p - n_p(M)) \ , \tag{52}$$

where n_p is the number density corresponding to log $Z(L^*,M^*)$. Now interpolating along the L axis,

$$\log Z(L^*,M^*) = \log (L,M^*) + \frac{\log Z(L+1,M^*) - \log Z(L,M^*)}{T_p(L+1) - T_p(L)} * (T_p - T_p(L)) \ , \tag{53}$$

where T_p is the temperature corresponding to log $Z(L^*,M^*)$.

Figure 2. The indices used to interpolate in a two-dimensional grid.

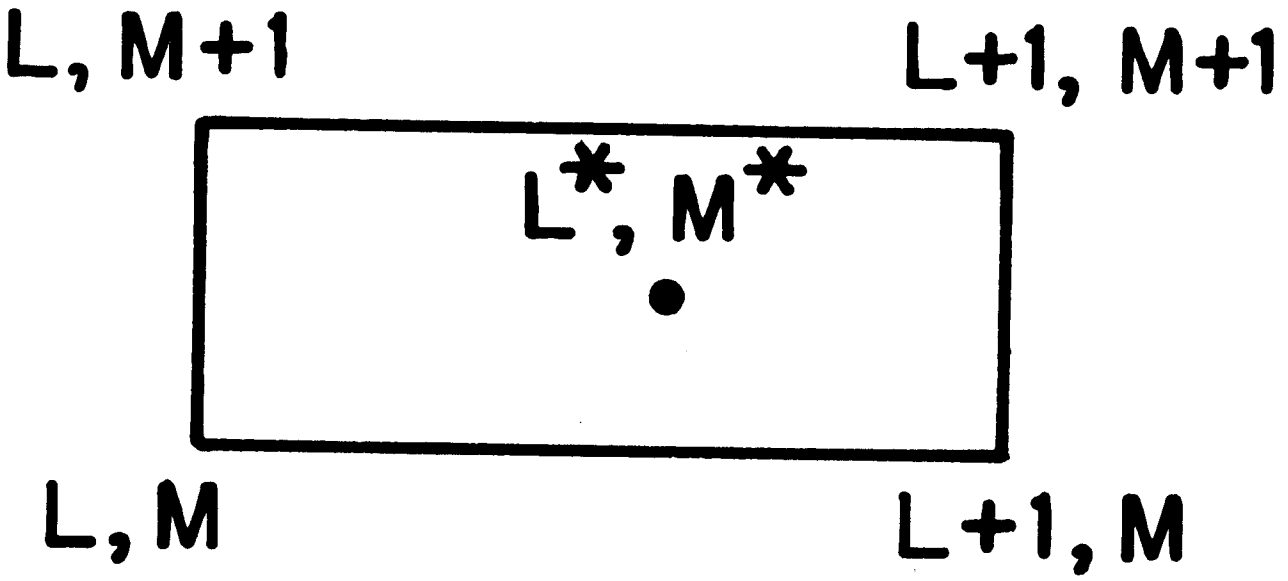

The grids used to interpolate in the three-dimensional tables are shown in Fig. 3. First we interpolate for log $\ell(M,K^*,L^*)$ and log $\ell(M+1,K^*,L^*)$ in the manner prescribed above. Then interpolating in the third dimension,

$$\log \ell(M^*,K^*,L^*) = \log \ell(M,K^*,L^*) + \frac{\log \ell(M+1,K^*,L^*) - \log \ell(M,K^*,L^*)}{n_p(M+1) - n_p(M)} (n_p - n_p(M)) \quad . \tag{54}$$

If the gas temperature computed by solving the energy equations is less than the lowest temperature in the equation of state tables, then the code automatically computes Z and E_p by interpolating between the bounds of the table and the values for a perfect un-ionized gas. This procedure preserves the accuracy of the calculation at low temperatures. The number density, n_p, should never exceed the bounds of the tables, or inaccurate results will be obtained.

VI. The Energy Conservation Check

At the end of each time step, a check is made to insure that the difference equations are conserving energy. This is done by integrating the energy equations over time and space. The two energy equations can be written as

$$\dot{E}_P + P_P\dot{V} = S_P + \dot{Q}_{PR} + \dot{Q}_{DP} \tag{55}$$

$$\dot{E}_R + P_R\dot{V} = S_R - \dot{Q}_{PR} + \dot{Q}_{DR} \tag{56}$$

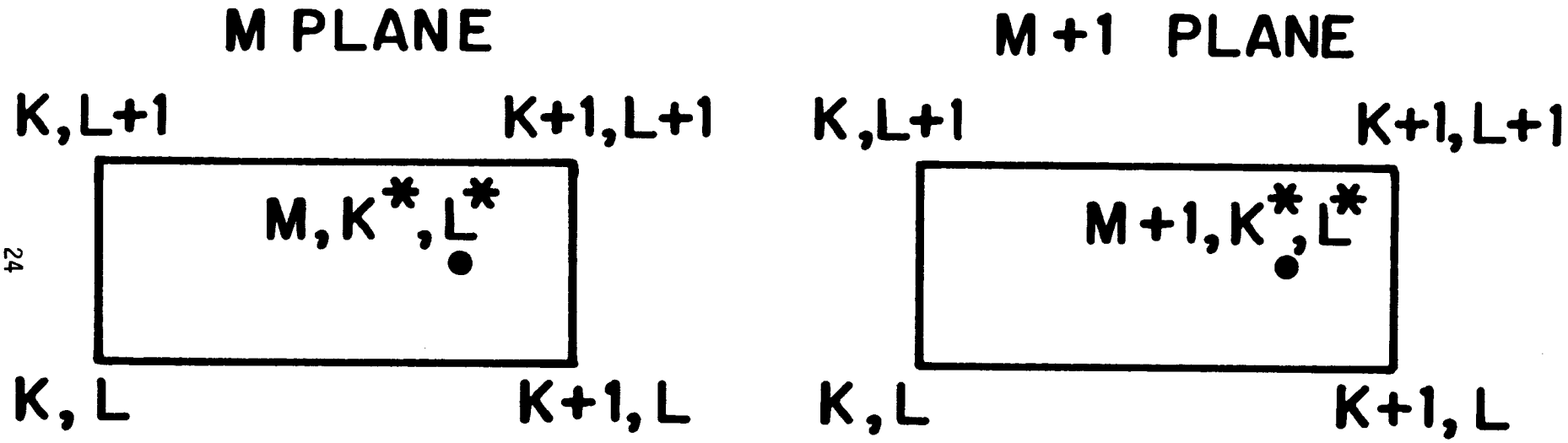

Figure 3. The indices used to interpolate in the three-dimensional tables.

where: $\dot{Q}_{PR} = \omega_R E_R - \omega_P T_P$

$$\dot{Q}_{Dx} = \frac{\partial}{\partial m_o} r^{\delta-1} K_x \frac{\partial(T_P \text{ or } E_R)}{\partial r} \qquad \text{where } x = P \text{ or } R \ ,$$

S_P = source of internal energy,

S_R = source of radiation (S_R = 0 in this version of the code).

After integration over space and time these equations take the form

GAS $$e_P^{n+1} + T^{n+1} = e_P^o + T^o + H_P^{n+1} + E_{RP}^{n+1} - F_P^{n+1} - W_P^{n+1} - G_R^{n+1} \qquad (57)$$

RADIATION $$e_R^{n+1} = e_R^o + H_R^{n+1} - E_{RP}^{n+1} - F_R^{n+1} - W_R^{n+1} + G_R^{n+1} \qquad (58)$$

TOTAL $$e^{n+1} + T^{n+1} = e^o + T^o + H^{n+1} - F^{n+1} - W^{n+1} \qquad (59)$$

The physical definitions of each term are:

e_x -- total internal energy of the gas or radiation.

T -- total kinetic energy of the gas.

H_x -- total source of energy to the gas or radiation.

E_{RP} -- total radiation energy exchanged between the gas to the radiation field.

W_x -- total work done on the outer boundary by the gas or radiation. These are zero in the FIRE code because the outer edge of the gas is stationary.

F_x -- total energy conducted to the first wall from the gas or radiation.

G_R -- work exchanged between the gas and radiation.

Each of these terms are given in finite difference form as follows:

$$e_x^{n+1} = \sum_{j=1}^{JMAX} (E_x)_{j-1/2}^{n+1} \, \Delta m_{o_{j-1/2}} \tag{60}$$

$$T^{n+1} = \frac{1}{4} \Delta m_{o_{JMAX-1/2}} (u_{JMAX}^{n+1/2})^2 + \frac{1}{2} \sum_{j=1}^{JMAX} \Delta m_{o_j} (u_j^{n+1/2})^2 \tag{61}$$

$$H_x^{n+1} = H_x^n + \Delta t^{n+1/2} \sum_{j=1}^{JMAX} (S_x)_{j-1/2}^{n+1/2} \, \Delta m_{o_{j-1/2}} \tag{62}$$

$$E_{RP}^{n+1} = E_{RP}^n + \Delta t^{n+1/2} \sum_{j=1}^{JMAX} (\dot{Q}_{RP})_{j-1/2}^{n+1/2} \, \Delta m_{o_{j-1/2}} \tag{63}$$

$$G_R^{n+1} = G_R^n + \Delta t^{n+1/2} \sum_{j=1}^{JMAX} \dot{u}_j^{n+1/2} (r^{\delta-1})_j^{n+1/2} (P_{R_{j+1/2}}^{n+1/2} - P_{R_{j-1/2}}^{n+1/2}) \tag{64}$$

$$+ \Delta t^{n+1/2} \, u_{JMAX}^{n+1/2} (r^{\delta-1})_{JMAX}^{n+1/2} [P_{R_{JMAX+1}}^{n+1/2} - P_{R_{JMAX-1}}^{n+1/2}]/2$$

$$W_x^{n+1} = W_x^n + \Delta t^{n+1/2} (u_{JMAX}^{n+1/2} (r^{\delta-1})_{JMAX}^{n+1/2} P_{x_{JMAX}}^{n+1/2}) \tag{65}$$

$$F_P^{n+1} = F_P^n + \Delta t^{n+1/2} \left[\frac{r^{\delta-1}}{(\frac{\Delta r}{K_P})}\right]_{JMAX}^{n+1/2} (T_{P_{JMAX+1/2}}^{n+1/2} - T_{P_{JMAX-1/2}}^{n+1/2}) \tag{66}$$

$$F_R^{n+1} = F_R^n + \Delta t^{n+1/2} \left[\frac{r^{\delta-1}}{(\frac{\Delta r}{K_R}) + \frac{\Delta E_R}{F_R}}\right]_{JMAX}^{n+1/2} (E_{R_{JMAX+1/2}}^{n+1/2} - E_{R_{JMAX-1/2}}^{n+1/2}) \tag{67}$$

The calculations made by the FIRE code do not conserve energy exactly because of the finite distance between points in the equation of state tables. The calculations usually conserve energy to within better than 10%.

VII. The Time Step Control

After each time step, the next time step is determined from a set of stability and accuracy constraints. The new time step is determined by

$$\Delta t^{n+3/2} = \mathrm{Max}\left[\Delta t_{min}, \mathrm{Min}\left(\Delta t_{max}, \frac{K_1}{R_1^{n+1}}, \frac{K_2 \Delta t^{n+1/2}}{R_2^{n+1}}, \frac{K_3 \Delta t^{n+1/2}}{R_3^{n+1}}, \frac{K_4 \Delta t^{n+1/2}}{R_4^{n+1}}\right)\right] \quad (68)$$

where:

$$R_1^{n+1} = \mathrm{Max}\left[\left(V_{j-1/2}^{n+1} \; P_{j-1/2}^{n+1}\right)^{1/2} / \Delta r_{j-1/2}^{n+1/2}\right] \quad (69)$$

$$R_2^{n+1} = \mathrm{Max}\left[\left(V_{j-1/2}^{n+1} - V_{j-1/2}^{n}\right) / V_{j-1/2}^{n+1/2}\right] \quad (70)$$

$$R_3^{n+1} = \mathrm{Max}\left[\left(E_{R_{j-1/2}}^{n+1} - E_{R_{j-1/2}}^{n}\right) / E_{R_{j-1/2}}^{n+1/2}\right] \quad (71)$$

$$R_4^{n+1} = \mathrm{Max}\left[\left(T_{P_{j-1/2}}^{n+1} - T_{P_{j-1/2}}^{n}\right) / T_{P_{j-1/2}}^{n+1/2}\right] . \quad (72)$$

The maximum values of R_1, R_2, R_3, and R_4 are found by sweeping over the zones. The input parameters K_1, K_2, K_3, and K_4 determine the severity of each constraint. The default value for K_1, K_2 and K_4 is 0.05. The default value of K_3 is set to 1.0×10^{35}, which in effect removes the radiation energy as a time step constraint. The justification for doing this is that the only place where the radiation energy is changing rapidly enough to constrain the time step is at a radiation wave front. Everywhere else the radiation field is in

quasi-equilibrium with the gas, because the speed of light is very fast. The shape of the radiation wave front cannot be resolved very accurately because of the size of the Lagrangian zones, so this time constraint can be removed.

VIII. The Subroutines and Their Functions

The FIRE code is written in FORTRAN IV, and can be run on any mainframe computer. It is written in a top-down modular style, as shown in Fig. 4. Each subroutine performs a specific function. These functions are briefly described below:

ABCDEF - computes the $\underline{A}$, $\underline{B}$, $\underline{C}$, $\underline{D}$, $\underline{E}$, and $\underline{F}$ matrices and vectors used to solve the energy transfer equations.

CLEAR - sets all common blocks to zero before the start of a calculation.

CROS - searches through the x-ray cross section table and computes the cross section of the gas.

DISTRB - computes the kinetic energy and momentum lost by the debris in each zone during a time step.

DUMP - writes all common blocks on unit 2 at the end of a calculation.

DYNDEP - computes the x-ray deposition and the new absorption cross section of each zone.

ECHECK - computes the integrals used in the energy conservation check.

EDATA - provides the electron shell structure of the gas for the x-ray deposition calculation.

ENERGY - computes T_P, E_R, and then T_R.

EOS,EOS1 - computes the equation of state quantities.

GASDEP - computes the temperature of the gas after x-ray deposition.

HYDRO - solves the equation of motion for the fluid velocity, new zone radii, Δr's, zone volumes, and specific volumes.

INITD - reads LOWEN namelist input and initializes the debris deposition calculation.

Figure 4. The flow diagram of the FIRE code. The dotted lines indicate conditional routes.

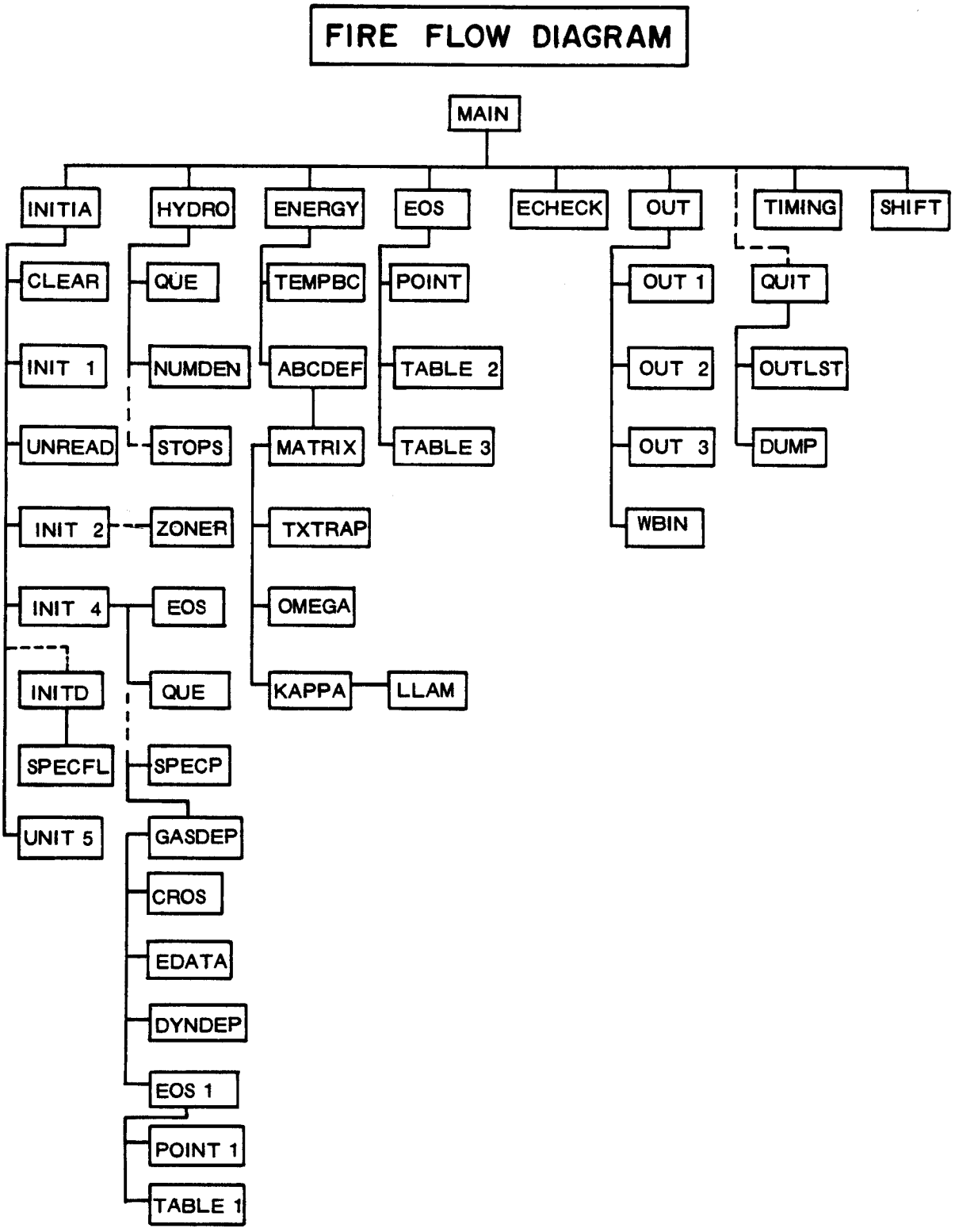

INITIA - reads namelist input and calls other initialization routines.

INIT1 - sets variable default values before reading input.

INIT2,4,5 - computes initial conditions and writes a summary of the initial conditions to unit 6.

KAPPA - computes plasma and radiation thermal conductivity and the radiation flux limit.

LLAM - computes log lambda.

MAIN - calls other routines to form the loop for one time step.

MATRIX - computes $\underline{\underline{a}}$, $\underline{\underline{\alpha}}$, $\underline{\underline{\gamma}}$, and $\underline{\underline{\omega}}$ matrices for use in the energy transfer calculation.

NUMDEN - computes number densities from the specific volume.

OMEGA - computes the radiation emission and absorption coefficients.

OUT,OUT1 - writes output to unit 6 at the end of specified time cycles.

POINT,POINT1 - finds pointers in the equation of state tables.

QUE - computes the artificial viscosity.

QUIT - wraps up the calculation at the end.

SHIFT - shifts values of variables at (n+1) to variables at (n) at the end of a time step.

SPECFL - computes the debris spectrum.

SPECP - computes the x-ray spectrum.

STOPS - computes the total kinetic energy and momentum lost by the debris during each time step.

TABLE2,TABLE1 - interpolates in the equation of state tables using the pointers.

TEMPBC - computes the plasma temperature and radiation specific energy boundary conditions.

TIMING - computes a new time step and determines whether the calculation is over.

UNREAD - reads in the common blocks from unit 4 at the beginning of a restarted calculation.

WBIN - writes binary output to unit 8 for postprocessing.

ZONER - computes the Lagrangian zoning automatically.

IX. Input/Output Units and Storage Requirements

The FIRE code uses ten different I/O units. These units are listed below along with their specific function.

Unit #	Function
2	FIRE writes all common blocks to this unit at the end of a calculation to allow a restart.
3	FIRE reads the equation of state tables from this unit.
4	FIRE reads the common blocks from this unit at the beginning of a restart calculation.
5	FIRE reads the namelist input from this unit.
6	FIRE writes lineprinter output to this unit.
8	FIRE writes binary output to this unit for postprocessing into plots.
9	FIRE writes the times corresponding to the stored heat fluxes on this unit.
10	FIRE writes the radiation heat fluxes to the wall on this unit.
11	FIRE reads x-ray cross section data on this unit.
12	FIRE writes the pellet x-ray spectrum reaching the wall on this unit.

FIRE requires about 60 K words of core storage on a UNIVAC 1110 computer and executes at a rate of approximately 2-5 msec/zone·cycle.

When adding a variable to the common blocks, the block length (set in INIT1) must be changed so that DUMP and UNREAD will write and read the correct number of words for a restart. Notice that the lengths are measured in double

words. This must be changed to single words if single precision is used. All of the variables should be changed to single precision if a CDC computer is used.

X. The Common Blocks

Nearly all of the real variables in the common blocks are in double precision, giving about 14 decimal places of accuracy on an IBM or UNIVAC computer. All real constants are specified with the "D" scientific notation (i.e., 1.=1.D0) to insure that all calculations are performed in double precision. The IBM FORGRAN G and H compilers will not define constants as double precision unless the "D" notation is used.

For many of the variables, the second to the last letter indicates whether the variable is at a zone center or zone boundary, and the last letter denotes the time level. The suffixes are:

1 -- zone boundary

2 -- zone center

A -- t^{n+1}

B -- $t^{n+1/2}$

C -- t^{n}

D -- $t^{n-1/2}$

The letter R will appear in a variable name if the quantity is associated with the radiation field, and N if the quantity is associated with the gas. Thus TR2B(J) is the radiation temperature in the center of zone j at time $t^{n+1/2}$, and U1D(J) is the fluid velocity on the zone j boundary at time $t^{n-1/2}$. The variables are grouped in common blocks so that a subroutine will find most of

the variables that it needs in fewer than all of the blocks. The common blocks are listed below along with their meaning and units. A * superscript denotes mandatory input variables, and a ** superscript denotes a variable with a default value.

[The remainder of the FIRE documentation has been omitted here for brevity. It describes all of the code variables, their units, etc. This is followed by a user's manual.]

C. Fireball Propagation Down Plasma Channels in the LIB-TDF

In this section we have reproduced UWFDM-455. It is a discussion of fireball propagation down plasma channels. This work was presented at the 1981 APS Plasma Physics Meeting.

Fireball Propagation in Preformed Plasma Channels in the Light Ion Beam Driven Target Development Facility

R.R. Peterson

K.J. Lee

G.A. Moses

Fusion Engineering Program
Nuclear Engineering Department
University of Wisconsin
Madison, WI 53706

January 1982

UWFDM-455

Abstract

In most proposed light ion beam driven fusion devices, preformed plasma discharge channels are proposed for propagation of the beams from the diodes to the fusion target. After the target explodes, the non-neutronic fraction of the fusion energy may propagate preferentially back up the plasma channels, causing very large heat fluxes on the diodes or other reactor cavity structures at the ends of the channels.

This problem is investigated for the Sandia Target Development Facility. Models of analysis and results are presented.

I. Introduction

A conceptual picture of the Light Ion Beam Target Development Facility is shown in Fig. 1. The preliminary parameters assume that there are 40 beams of light ions, 20 current return lines and that the reactor cavity is 3 meters in radius. The problem considered in this paper is the propagation of non-neutronic fusion energy down preformed plasma channels, a problem of potential importance to light ion beam driven reactors as well as the Target Development Facility.

In most proposed light ion beam driven fusion devices, the ions propagate from the diodes to the target down plasma channels which are lower in density than the surrounding gas.[1-4] The beams of ions drive the implosion of D-T fusion targets which burn, yielding 50 to 100 times the beam energy in 14 MeV neutrons, x-rays and target debris ions and electrons.[5] The neutronic energy, which accounts for approximately 70% of the yield, is not stopped to any significant degree by the cavity gas and is not affected by the presence of channels. On the other hand, the soft x-rays, ions and electrons[6] are slowed down or absorbed by the cavity gas; hence their movement away from the explosion and towards the cavity walls may be enhanced by the presence of channels. This means that 30% of the target yield may propagate back up the plasma channels where the densities and stopping powers are lower. This could lead to very high heat fluxes on the materials at the end of the channels.

In this study,[7] we have developed models to simulate the propagation of non-neutronic energy down the plasma channels and have obtained some preliminary values for the heat fluxes both axially down the channel and radially out from the channel into the colder surrounding cavity gas. All of the non-neutronic energy is assumed to be initially converted to thermal radiation.

Figure 1 Light Ion Beam Target Development Facility

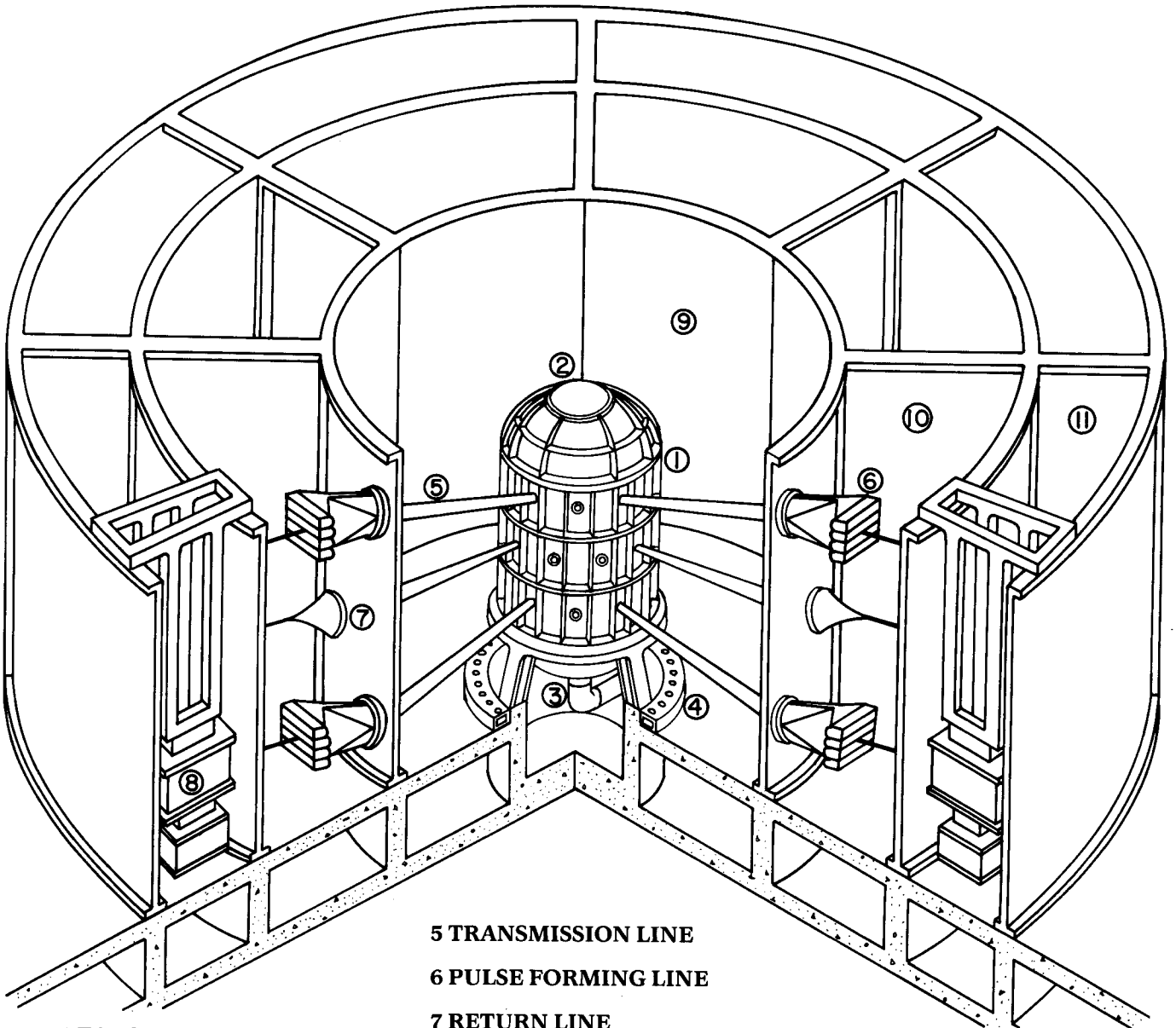

1 TARGET CHAMBER

2 DIAGNOSTIC PORT

3 PURGE LINE

4 AIR BUBBLE PLENUM

5 TRANSMISSION LINE

6 PULSE FORMING LINE

7 RETURN LINE

8 BEAM MARX GENERATOR

9 SHIELDING POOL – WATER

10 PULSE FORMING SECTION – WATER

11 ENERGY STORAGE SECTION – OIL

In Section II, the computer model, which is a one-dimensional simulation of a two- or three-dimensional effect, is described. Preliminary results are presented in Section III and conclusions and recommendations are made in Section IV.

II. Computer Model

A one-dimensional Lagrangian hydrodynamics computer code, FIRE, has been modified to simulate the multi-dimensional nature of blast wave propagation through the cavity gas and down the plasma channels. This is done by first running a series of one-dimensional simulations of the radial heat transfer from the hot center of a channel to the surrounding cavity gas. From this, a phenomenological law for the radial heat loss from a channel is obtained as a function of the radiation energy density in the channel. This law for the radial heat loss is then used in the calculation of the axial heat transfer down the channel. These two types of heat transfer are depicted schematically in Fig. 2 where channels are shown to be connected to the fusion generated fireball. All x-ray, ion and electron energy from the microexplosion is assumed to be stopped in an initial spherical fireball. The energy flows out of the fireball into the plasma channel, then either down the channel or out into the surrounding cavity gas.

The one-dimensional hydrodynamics code, FIRE,[8] includes radiation diffusion and uses tabulated values of equation of state and opacity data. This data is provided by the atomic physics code, MIXER,[9] which uses either Saha or Coronal equilibrium models to compute ionization states, depending on the temperature and density of the gas, and uses a semi-classical optical model to calculate photo-ionization, atomic line absorption, and inverse Bremsstrahlung.

Figure 2
Schematic representation of heat transfer in plasma channels.

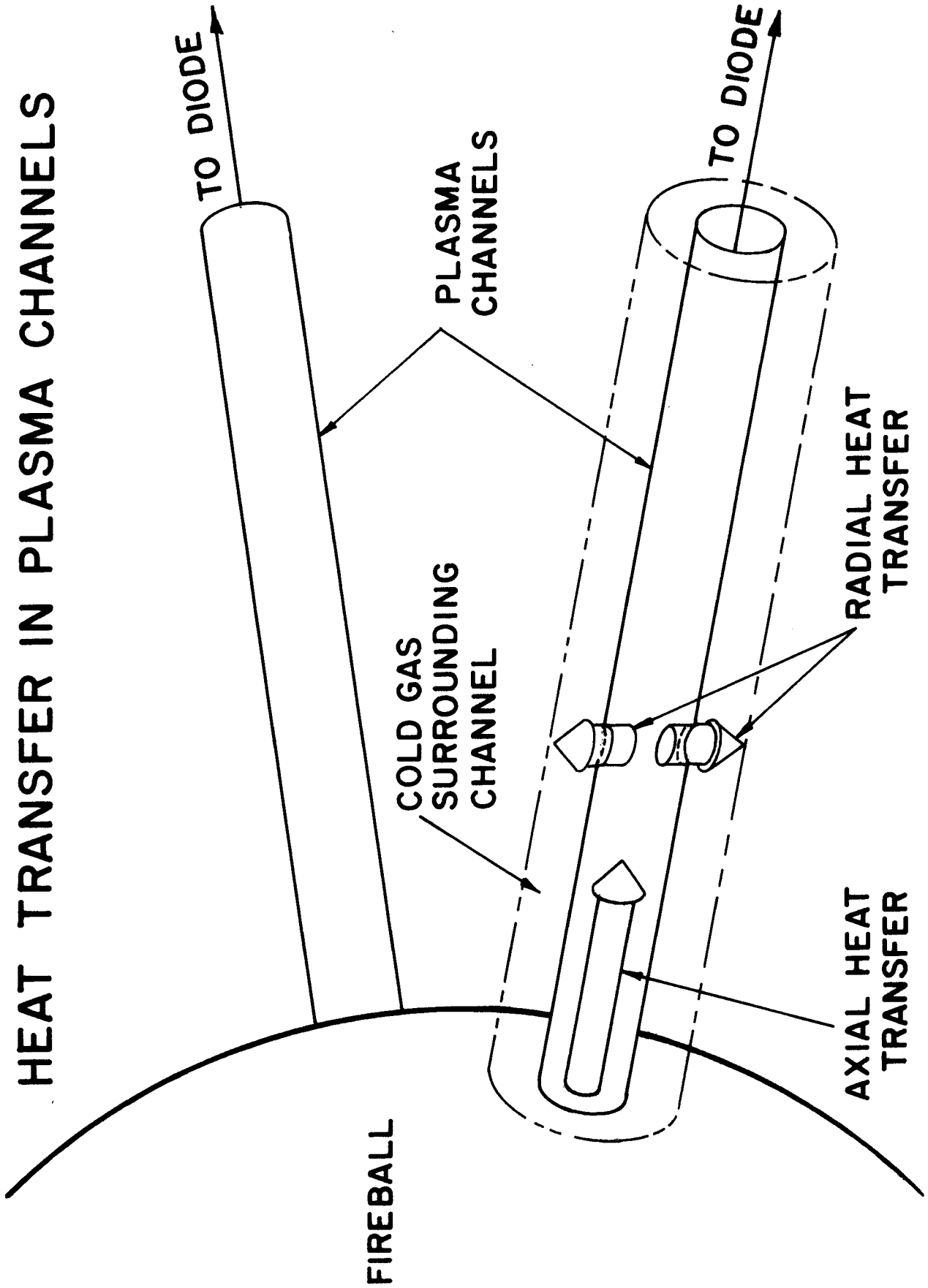

Where appropriate, Thomson scattering and absorption by plasma waves are also included.

There are two changes needed in FIRE to do the axial transport calculation. The addition of a source term which represents the energy added to the channel from the fireball is the first. This is written as

$$S_F = \sigma T_F^4 A_c \tag{1}$$

where T_F is the temperature of the fireball, σ is the Stefan-Boltzmann constant, and A_c is the cross sectional area of the channel. The other is a loss term representing the radial heat loss which is written as

$$S_L = \omega_L E_R \tag{2}$$

where ω_L is the loss coefficient determined by simulations of the radial transport and E_R is the energy of the radiation in the channel. S_F is non-zero only for the Lagrangian zone nearest the fireball while S_L depends on the radiation energy density in each zone.

The plasma and radiation energy transport equations are then rewritten. For the plasma,

$$C_{vp} \frac{\partial T_p}{\partial t} = \frac{\partial}{\partial m_o} \left(K_p \frac{\partial T_p}{\partial r}\right) - \frac{\partial P_p}{\partial T_p} \left(\frac{\partial V}{\partial t}\right) T_p + J_R - J_p + S_F \ , \tag{3}$$

where C_{vp} is the specific heat at constant volume, T_p is the plasma temperature, m_o is the Lagrangian mass, K_p is the plasma conductivity, P_p is the plasma pressure, V is the specific volume of the plasma, J_R is the radiant

power density absorbed by the plasma and J_p is the power density lost to emission by the plasma. For the radiation,

$$\frac{\partial}{\partial t} E_R = \frac{\partial}{\partial m_o} \left(K_R \frac{\partial}{\partial r} E_R\right) - P_R \frac{\partial}{\partial m_o} u - J_R + J_p - S_L \ , \qquad (4)$$

where K_R is the radiation conductivity, P_R is the radiation pressure, and u is the hydrodynamic velocity. In both Eqs. (3) and (4), plane geometry is assumed.

III. Results

The model outlined in Section II was used to calculate the propagation of fusion generated energy down the plasma channels. Since the model is only one-dimensional and the effects may be multi-dimensional, these results must be considered preliminary until some two-dimensional calculations are done to verify them. The purpose of presenting these preliminary results here is to demonstrate which effects are important. Table I shows a list of parameters for the calculations done which are consistent with a Light Ion Beam Target Development Facility.

The radial energy loss was calculated for a number of channel radiation energy densities. Results of a typical calculation are shown in Figs. 3 and 4 where the radiation temperature and the plasma temperature are respectively plotted against distance from the center of the channel for various times. These plots show how radiation from the hot channel center heats up the cavity gas surrounding the channel. These calculations were done with FIRE in its cylindrically symmetric form.

From these calculations, the radial loss coefficient, ω_L, has been determined for several initial channel center radiation energy densities. These

Table I

LIGHT ION BEAM CHANNEL PARAMETERS

GAS TYPE	ARGON WITH 0.2% SODIUM
AMBIENT GAS DENSITY	7×10^{17} ATOM/CC
GAS DENSITY IN CHANNEL	1.8×10^{17} ATOM/CC
AMBIENT GAS TEMPERATURE	0.05 eV
GAS TEMPERATURE IN CHANNEL (AT TIME OF MICROEXPLOSION)	25 eV
NUMBER OF CHANNELS	60
LENGTH OF CHANNELS	3 m
RADIUS OF CHANNELS	0.8 cm
INITIAL FIREBALL ENERGY	60 MJ
INITIAL FIREBALL VOLUME	6.5×10^{4} CC

Figure 3

Radial radiation temperature profiles.

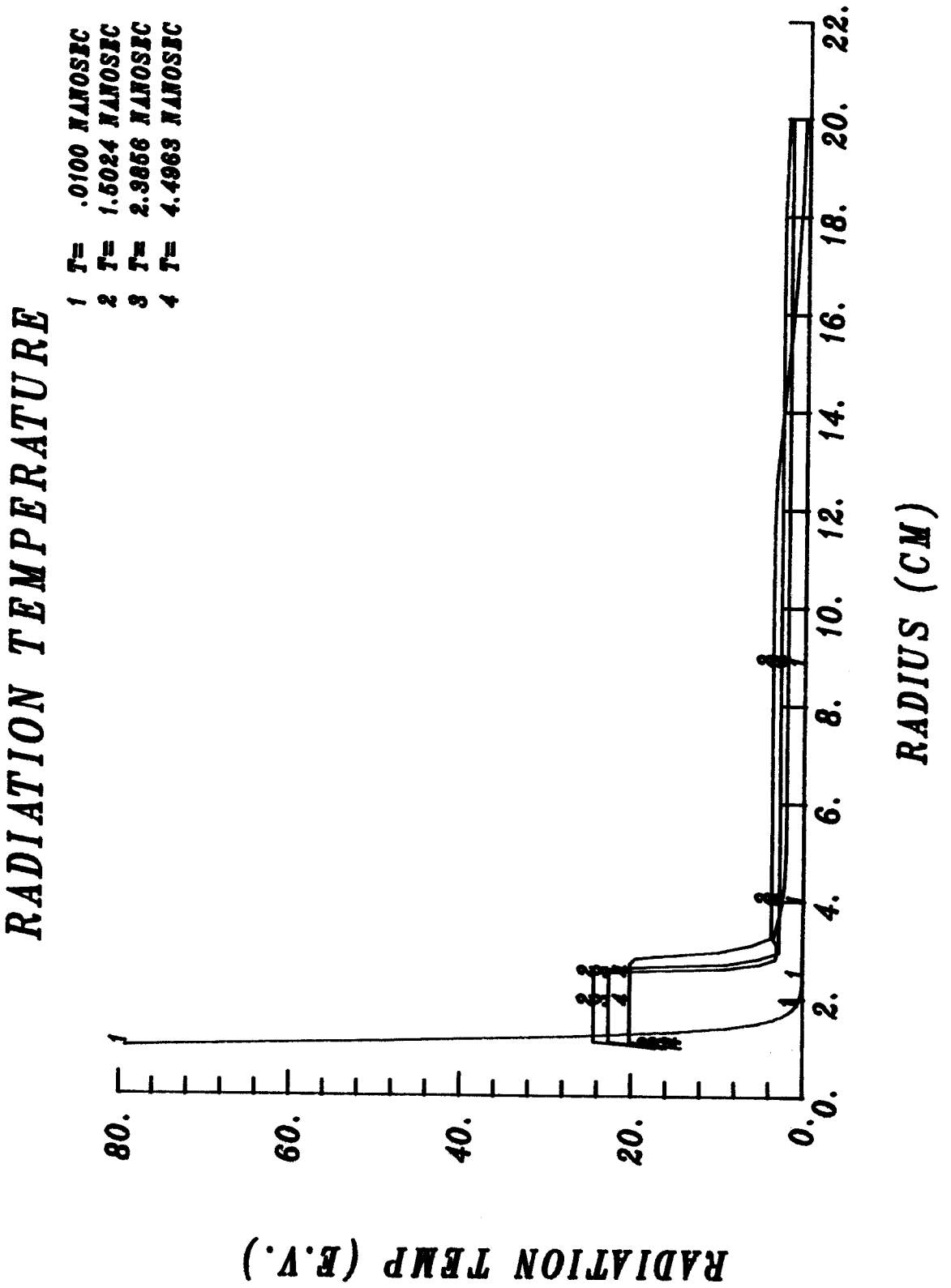

Figure 4

Radial plasma temperature profiles.

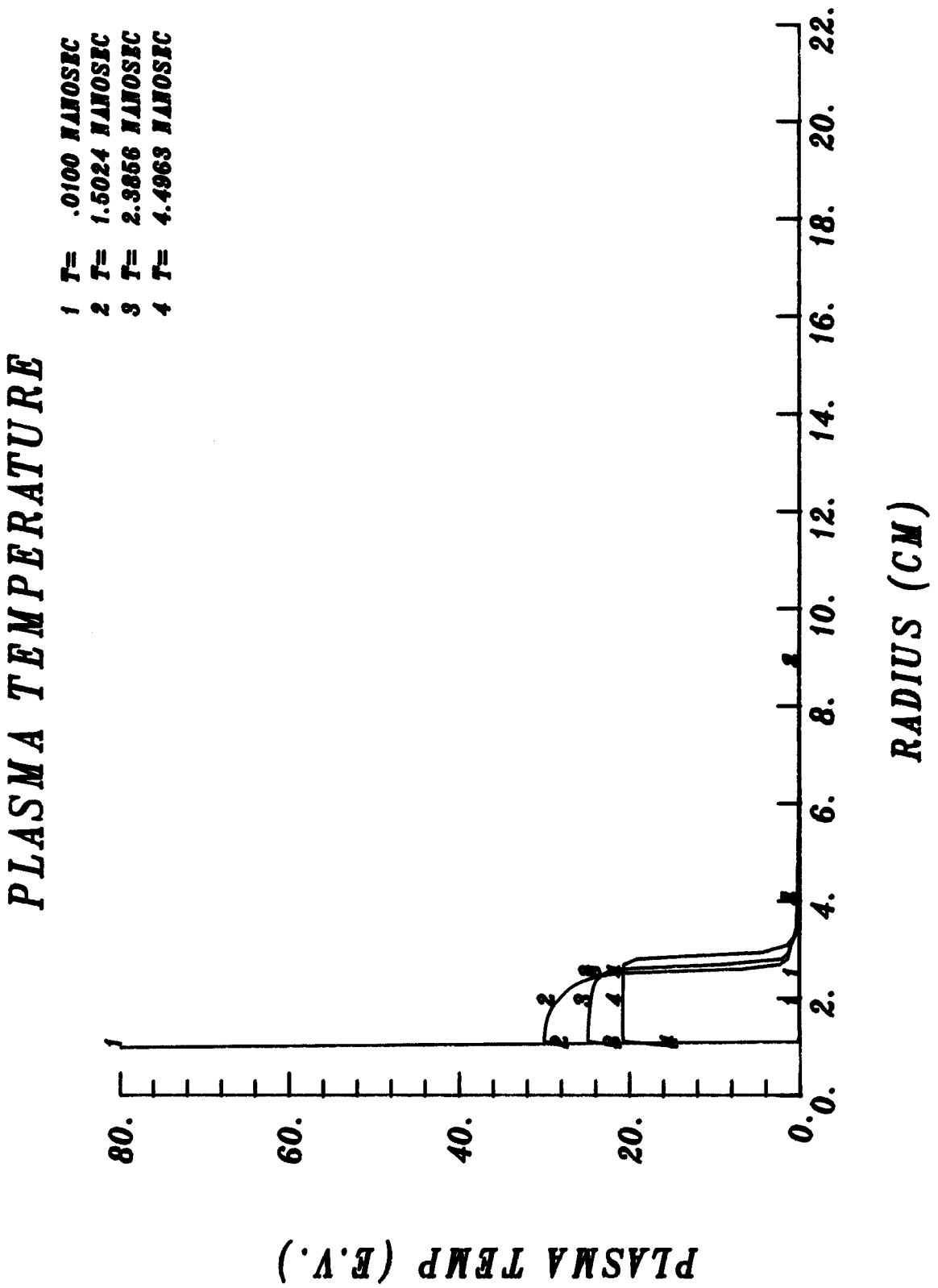

are plotted against radiation energy density in Fig. 5. This is not a single valued function because at a given radiation energy density the gas surrounding the channel may be at any of a range of plasma temperatures. At a radiation energy density of 10^5 J/g, ω_L varies by an order of magnitude. This variation shows that in converting the problem from two-dimensional to one-dimensional, there is an unavoidable loss of accuracy. However, the range of ω_L is known so that the sensitivity of the axial heat transport calculation to this uncertainty may be tested. Also shown in Fig. 5 is the phenomenological value for ω_L,

$$\omega_L = 1.4 \times 10^9 \, E_R^{0.138} \ \text{sec}^{-1} \ ,$$

where E_R is in J/g. This is the value of ω_L used in all axial calculations but those done to test the sensitivity to ω_L.

Once ω_L has been determined, the axial fireball propagation can be simulated. Figure 6 shows how the total energy in the fireball decreases with time. It has an irregular shape because the fireball loses energy at a rate proportional to T_F^4 and the specific heat of the gas is a strong function of temperature. The hydrodynamic motion of the gas in the channels is shown in Figs. 7 and 8, where first the positions of the Lagrangian zone boundaries are plotted against time and then the plasma mass density is plotted against distance down the channel for various times. A four-fold increase in the mass density is caused by the propagating blast wave. In Figs. 9 and 10, the plasma and radiation temperatures are shown versus axial position and time. From these two plots, one can see that channels cool off rapidly from initial temperatures of 25 eV to about 1 eV. This is due to large losses in radiant

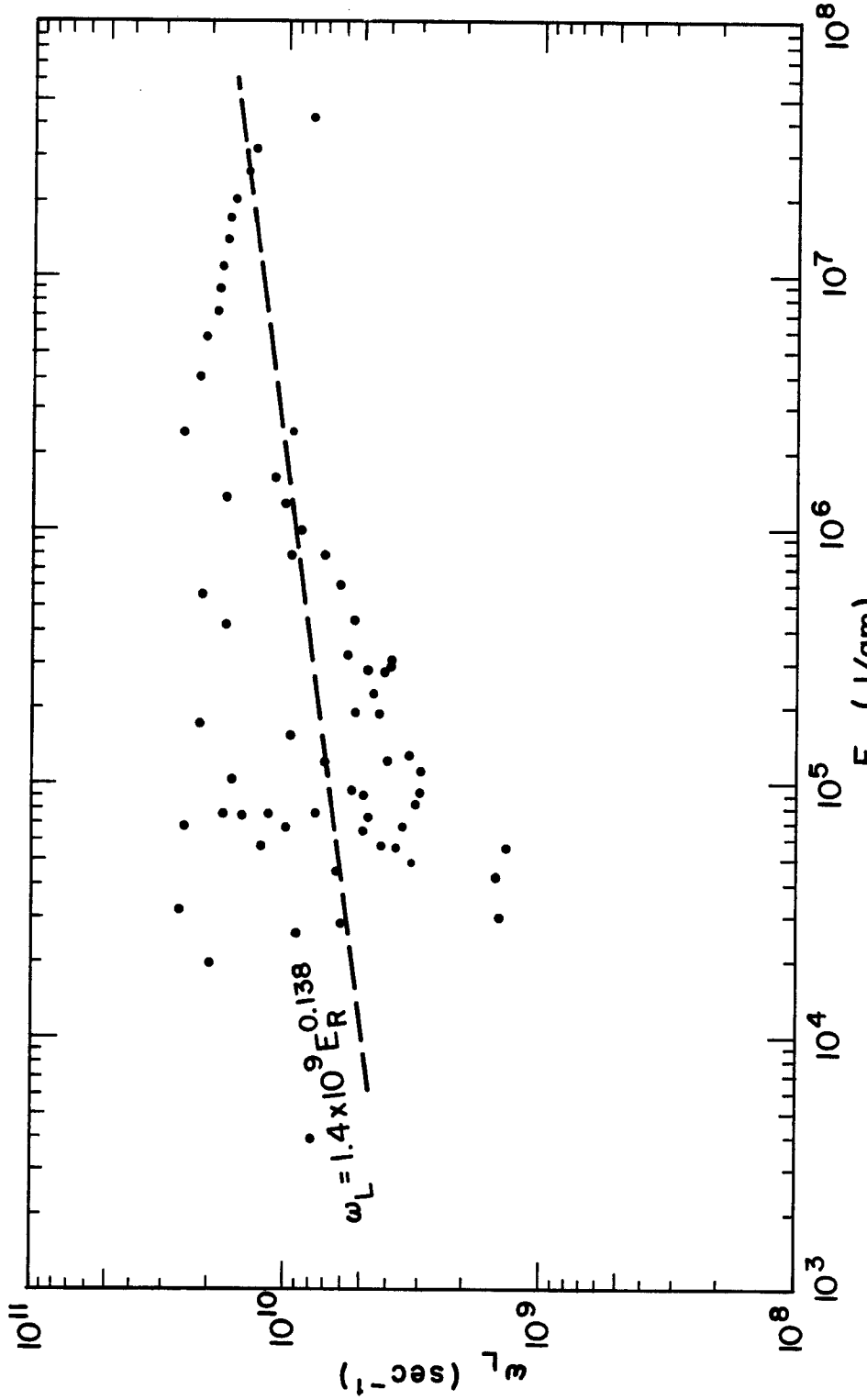

Figure 5 Radial loss coefficient versus radiation energy density in center of channel.

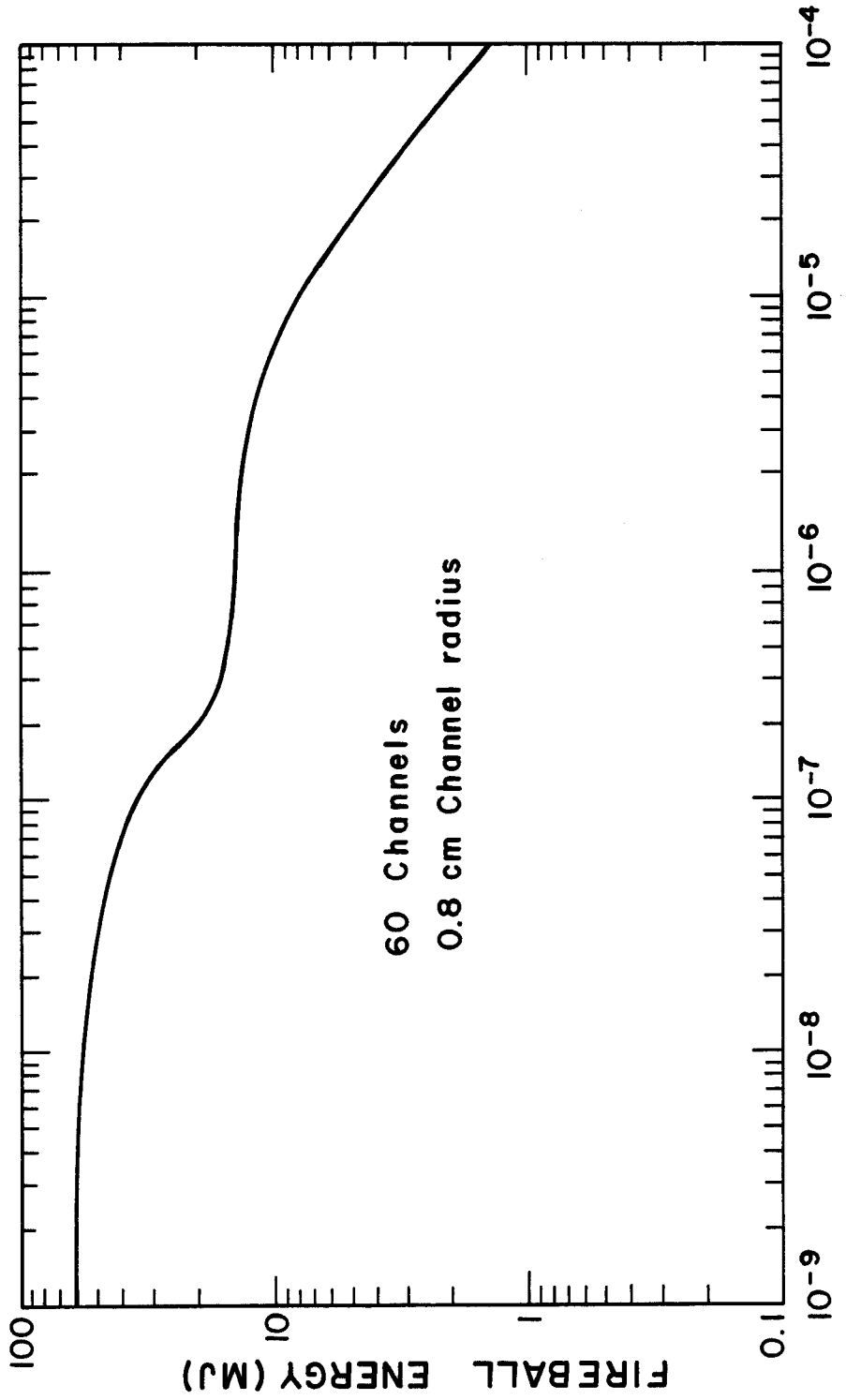

Figure 6 Energy in fireball vs. time.

Positions of Lagrangian zone boundaries versus time.

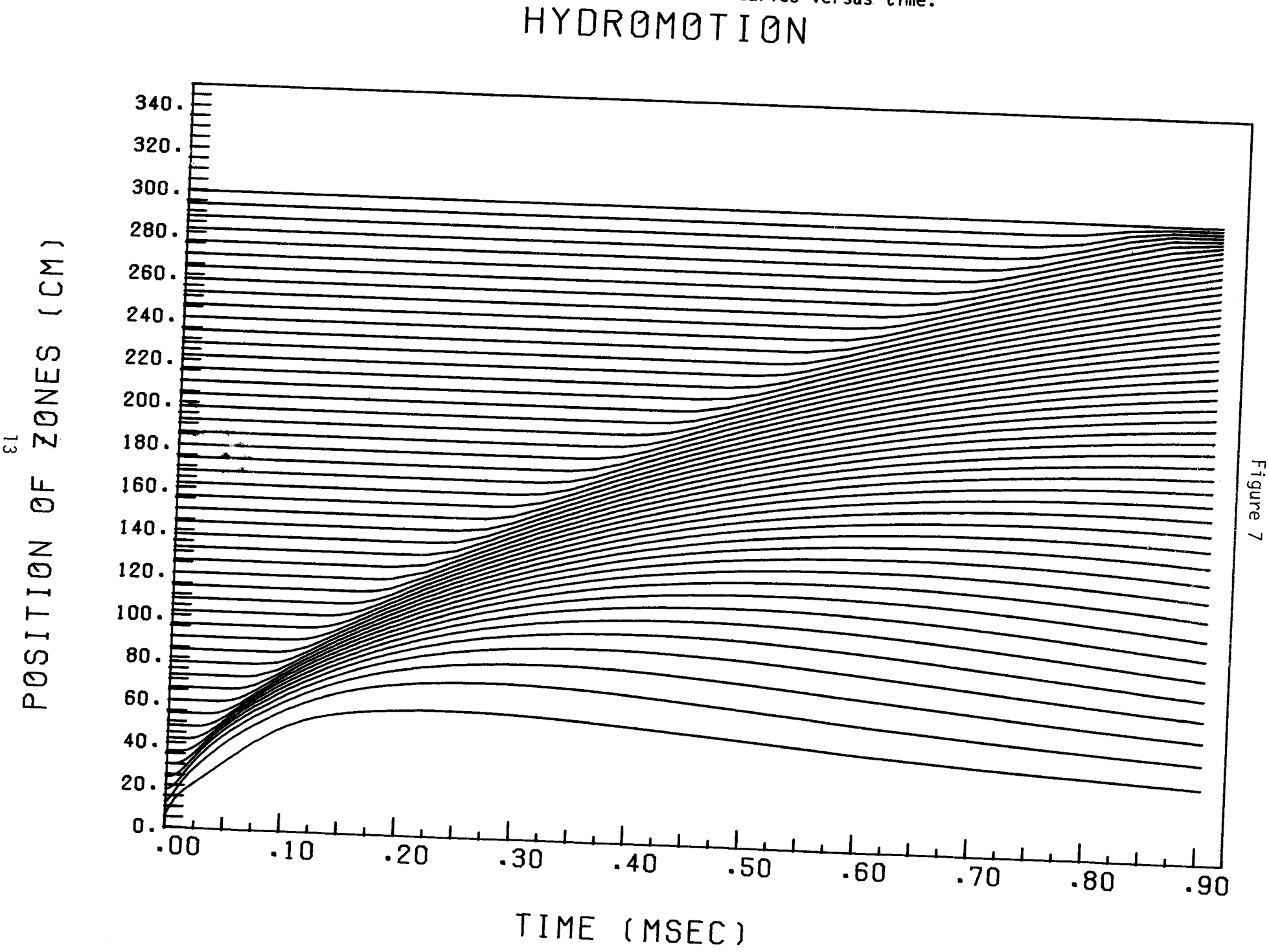

Figure 7

Figure 8

Plasma mass density profiles axially down channels.

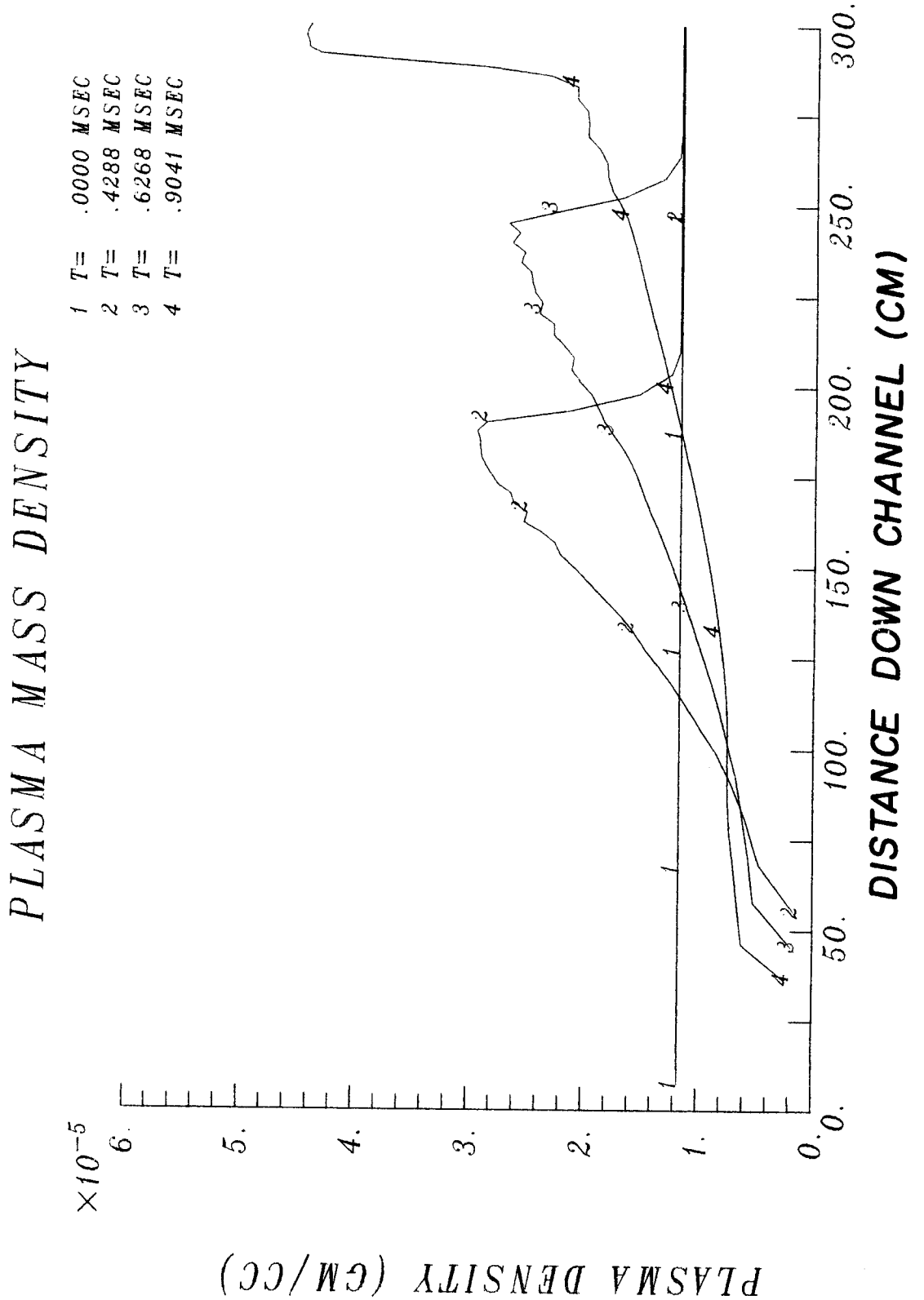

Figure 9

Plasma temperature profiles axially down channels.

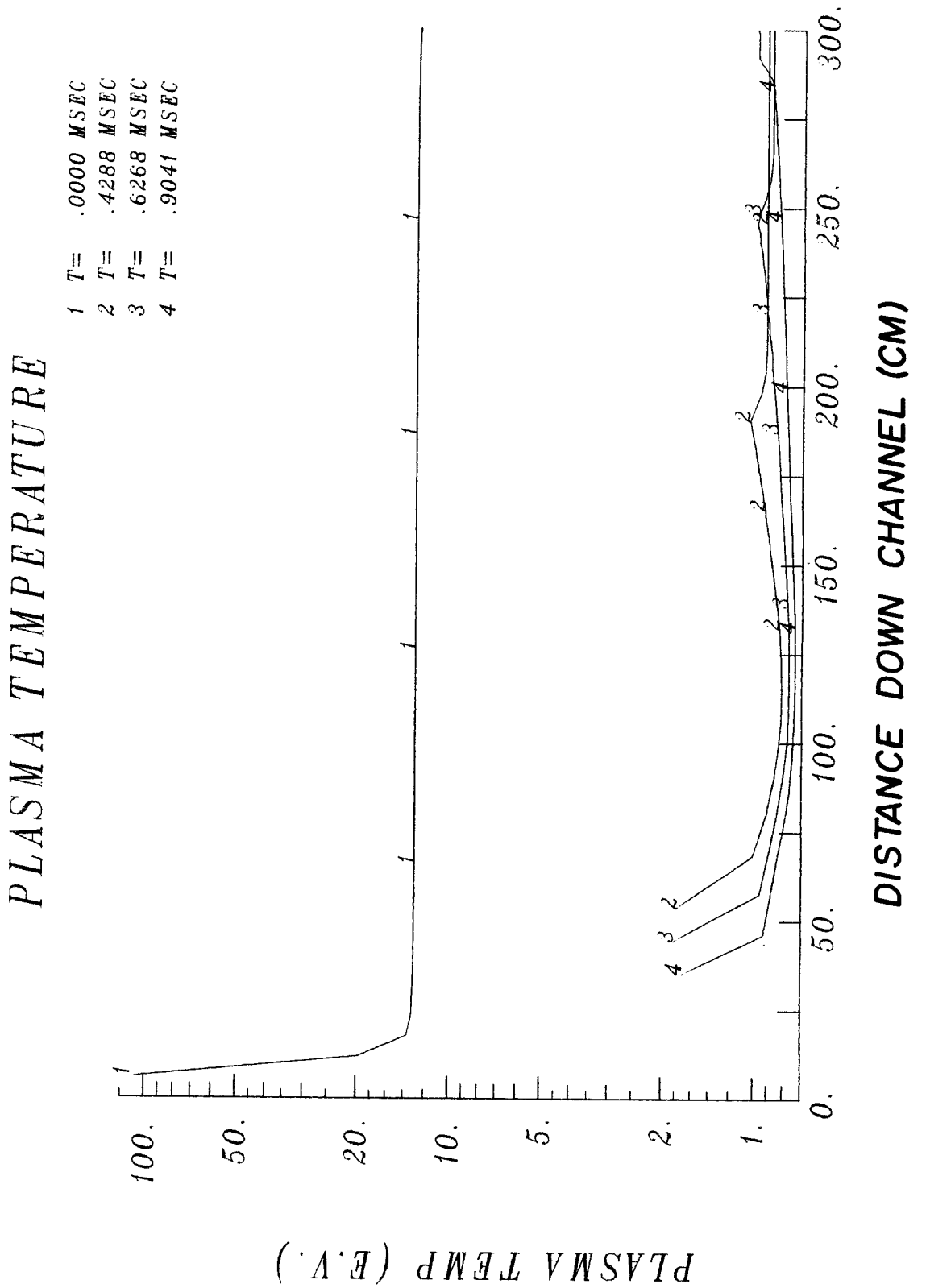

Figure 10

Radiation temperature profiles axially down channels.

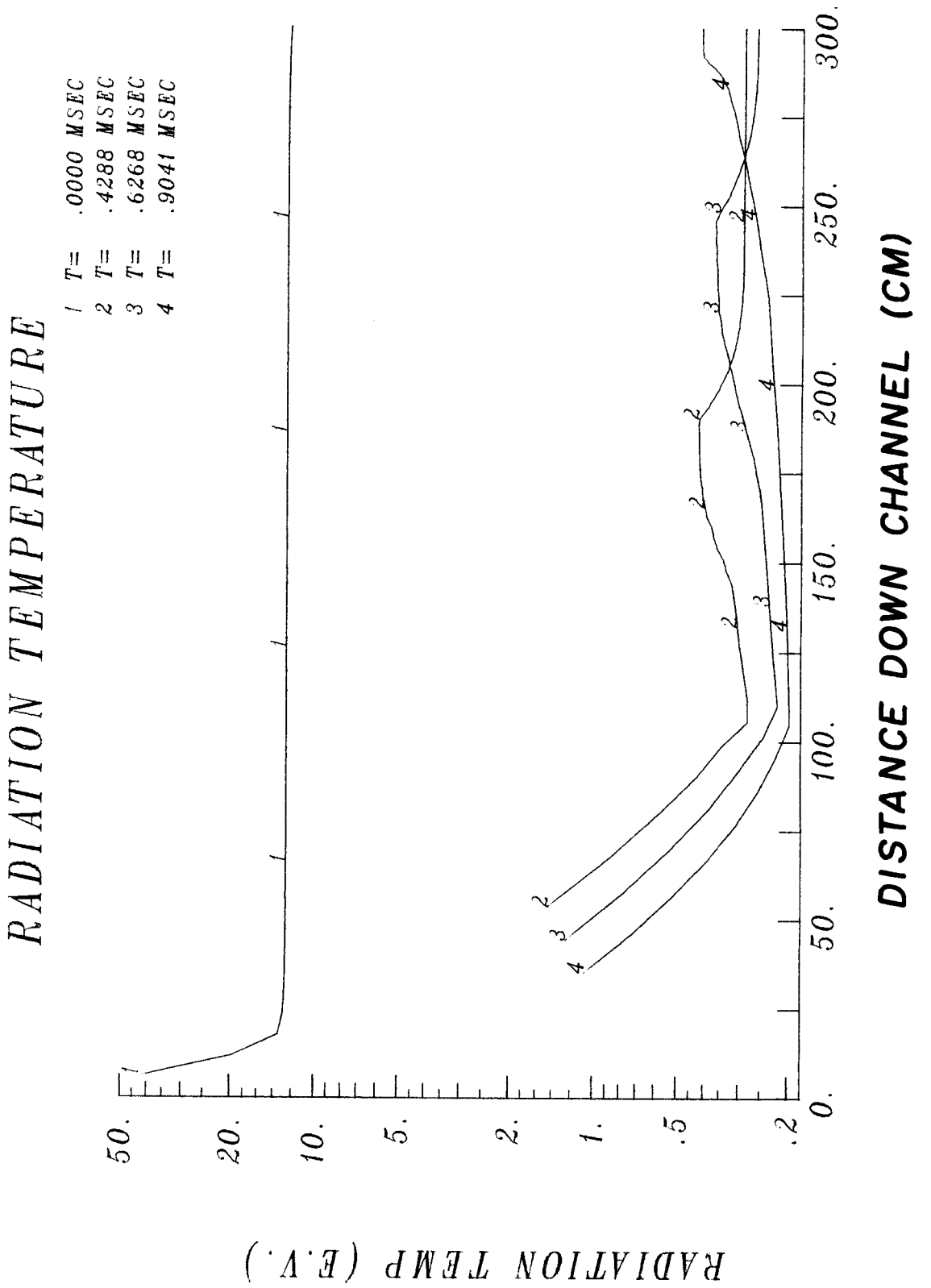

energy to the cold cavity gas surrounding the channels. One may also see the warm blast front propagating down the channel. Similar calculations have been made for values of ω_L that range over the order of magnitude of uncertainty shown in Fig. 5. They are not greatly different from the results presented here. This means that the results presented here are not very sensitive to changes in ω_L.

The energy balance for a channel is shown in Fig. 11. The fireball loses 60 MJ during the calculation and there are 60 channels so that each channel receives 1 MJ from the fireball. Of this, only 13.4 J reaches the end of the channels directly and 999,986.6 J are lost to the cavity gas. Once energy is in the cavity gas, it is assumed to follow the behavior previously predicted by spherical fireball calculations[10] (no channels). This spherical calculation predicts that 29 J/cm^2 are uniformly radiated to the first wall of the Target Development Facility. With the 13.4 J deposited at the end of the 1 cm^2 cross sectional area channels, the radiated energy density at the end of the channels becomes 42.4 J/cm^2. This is shown in the graph in Fig. 11.

The heat transfer to the cavity gas is roughly 10^5 times larger than the transfer down the length of the channel, a fact which can be explained by simple physical arguments. The area of the sides of a single cylindrical channel is 1.5×10^3 cm^2 compared with a cross sectional area of 2 cm^2, so that a factor of 10^3 is gained by the radial transport from the difference in area. The atomic physics calculations in MIXER have shown that the important radiation mean free paths for radial transport are typically 3×10^4 cm while those governing axial transport are roughly 7×10^2 cm. Thus radial transport gains another factor of 50 from the differences in opacities making a total difference of 5×10^4 which is close to the observed difference.

Figure 11

Schematic representation of preliminary energy balance in plasma channels and density of energy radiated to first surface versus position on surface.

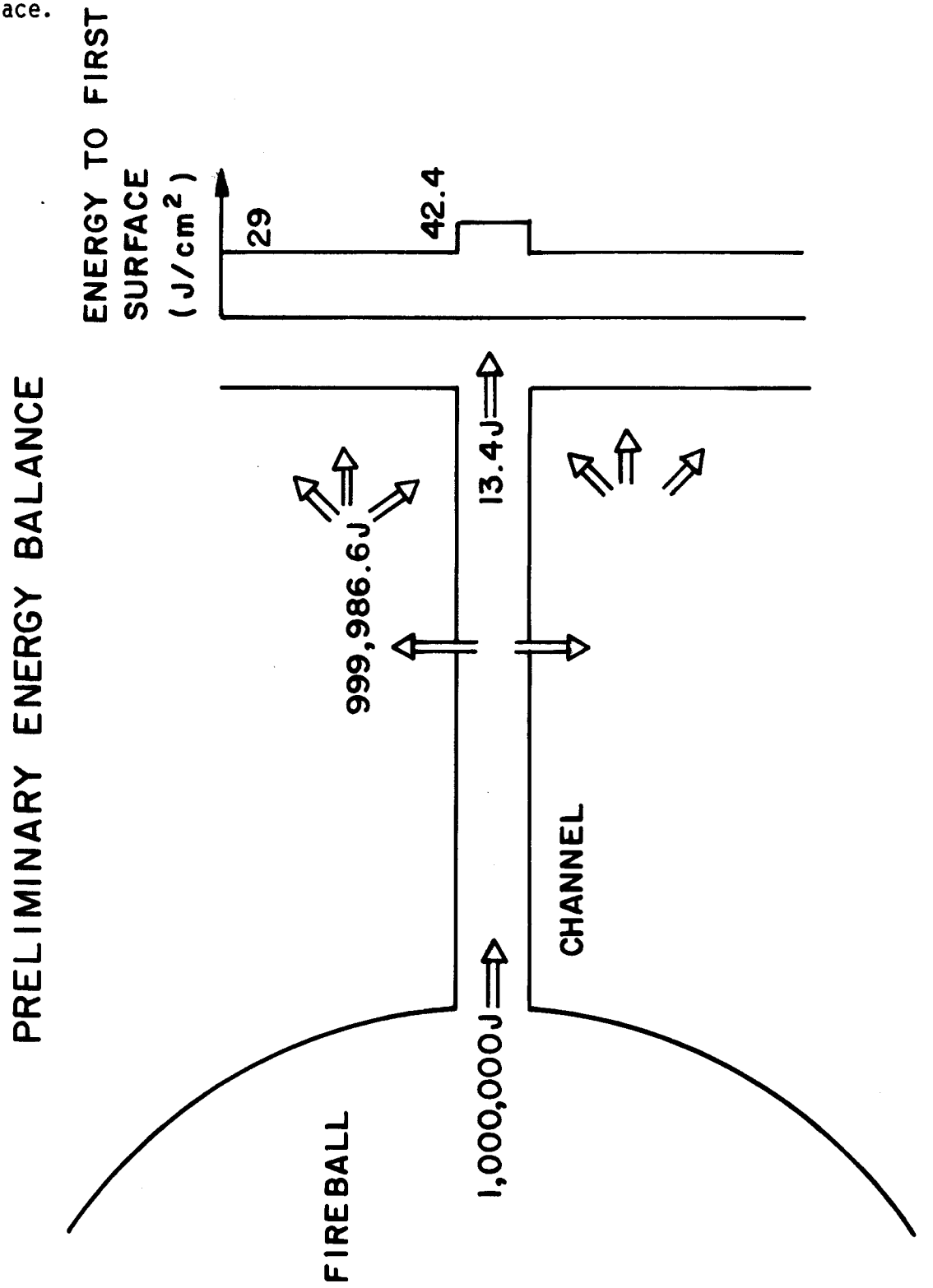

IV. Conclusions and Recommendations

A potentially important problem for light ion driven fusion devices has been considered. The following conclusions may be made:

1. The results indicate that propagation of fireball energy down preformed plasma channels increases the thermal load on the wall by roughly 50%, an increase which can be accommodated by minor changes in the first wall design.
2. It must be re-emphasized that the analysis of this problem treats it as one-dimensional while it is actually a multi-dimensional effect. This causes unavoidable uncertainty in the accuracy of the results, though the sensitivity of the results to the loss coefficient was tested and found not to be great.

As a consequence of this study, the following recommendations are made.

1. A two-dimensional simulation of fireball propagation down plasma channels should be made to verify the results presented here.
2. The spherical fireball simulation should be done by including the losses from the channel as a source instead of assuming that it behaves as if there were no channels present.

Acknowledgment

This work was supported by Sandia National Laboratories under contract DE-AS08-81DP40161.

References

1. T.P. Wright et al., "Light Ion Transport in Plasma Channels for ICF," Sandia Report SAND-03670 (1980).

2. J.N. Olsen, "Laser-Initiated Channels for Ion Transport: CO_2-Laser Absorption and Heating of NH_3 and C_2H_4 Gases," J. Appl. Phys. 52, (1981) 3279.

3. J.N. Olsen, D.J. Johnson, and R.J. Leeper, "Propagation of Light Ions in a Plasma Channel," Appl. Phys. Lett. 36, (1980) 808.

4. R.R. Peterson, G.A. Moses, and G.W. Cooper, "Cavity Gas Analysis for Light Ion Beam Fusion Reactors," Nucl. Tech./Fusion 1, (1981) 377.

5. R.O. Bangerter, J.W-K. Mark, and D.J. Meeker, "Target Gain for Ion Driven Inertial Fusion Targets," Bull. Am. Phys. Soc. 26, (Oct. 1981) 1009.

6. The potential problem of energetic electrons preferentially moving down the plasma channel was suggested by S.A. Goldstein.

7. This work was described in part at the APS Plasma Division Meeting in October 1981; R.R. Peterson, K.J. Lee, and G.A. Moses, "Fireball Dynamics in Preformed Plasma Channels in Light Ion Beam Fusion Reactors," Bull. Am. Phys. Soc. 26, (1981) 900.

8. G.A. Moses and R.R. Peterson, "FIRE - A Computer Code to Simulate Cavity Gas Response to Inertial Confinement Target Explosions," University of Wisconsin Fusion Engineering Program Report UWFDM-336 (Jan. 1980); also, T.J. McCarville, R.R. Peterson, and G.A. Moses, "Improvements in the FIRE Code for Simulating the Response of a Cavity Gas to Inertial Confinement Fusion Target Explosions," University of Wisconsin Fusion Engineering Program Report UWFDM-407 (June 1981; Revised February 1982).

9. R.R. Peterson and G.A. Moses, "MIXER - A Multi-Species Optical Data and Equation of State Computer Code," University of Wisconsin Fusion Engineering Program Report UWFDM-372 (Sept. 1980).

10. R.R. Peterson, K.J. Lee, and G.A. Moses, "Low Density Cavity Gas Fireball Dynamics in the Light Ion Beam Target Development Facility," University of Wisconsin Fusion Engineering Program Report UWFDM-442 (Oct. 1981); also presented at the 9th Symposium on Engineering Problems of Fusion Research, Chicago, IL, 26-29 October 1981.

Appendix

The following is an updated list of the publications, reports, conference proceedings, theses, etc., that were supported in part by Sandia Laboratory.

PUBLICATIONS SUPPORTED BY SANDIA CONTRACT

1. M. Ragheb, G.A. Moses, C.W. Maynard, "Pellet and Pellet-Blanket Neutronics and Photonics for Electron Beam Fusion," Nucl. Tech. 48, 16 (1980).

2. G.A. Moses and R. Spencer, "Compact Electron Beam or Light Ion Beam Fusion Reactor Cavity Design Using Nonspherical Blast Waves," Nucl. Fusion 19, 1386 (1979).

3. G.A. Moses and R.R. Peterson, "First Wall Protection in Particle Beam Fusion Reactors by Inert Cavity Gases," Nucl. Fusion 20, 849 (1980).

4. R.R. Peterson and G.A. Moses, "MFP - A Code for Calculating Equation of State and Optical Data for Noble Gases," Comp. Phys. Comm. 20, 353 (1980).

5. R.R. Peterson, G.W. Cooper, and G.A. Moses, "Cavity Gas Analysis for Light Ion Beam Fusion Reactors," Nucl. Tech./Fusion 1, 377 (1981).

CONFERENCE PROCEEDINGS SUPPORTED BY SANDIA CONTRACT

1. D.L. Cook, G.A. Moses, R.R. Peterson, E.G. Lovell, et al., "Light Ion Driven Inertial Fusion Reactor Concepts," Fourth ANS Top. Mtg. on Fusion Technology, King of Prussia, PA, Oct. 1980.

2. E.G. Lovell, R.R. Peterson, R.L. Engelstad, and G.A. Moses, "Transient Electric Stresses in ICF Reactor First Wall Structural Systems," Second ANS Top. Mtg. on Fusion Materials, Seattle, WA, Aug. 1981.

3. R.R. Peterson, K.J. Lee, and G.A. Moses, "Low Density Cavity Gas Fireball Dynamics in the Light Ion Beam Target Development Facility," IEEE Ninth Symp. on Engin. Probs. of Fusion Research, Chicago, IL, Oct. 1981.

MEETING TRANSACTIONS SUPPORTED BY SANDIA CONTRACT

1. R.R. Peterson and G.A. Moses, "Response of Cavity Gases to Particle Beam Target Explosions," Trans. ANS 33, 46 (1979).

2. G.W. Cooper, R.R. Peterson, and G.A. Moses, "Cavity Gases for Light Ion Beam Fusion Reactors," IEEE Conf. on Plasma Science, Madison, WI, 1980.

3. R.R. Peterson and G.A. Moses, "Light Ion Beam Fusion Cavity Gas Physics and Its Impact on Reactor First Walls," Bull. APS 25, 1030 (1980).

4. R.R. Peterson, K.J. Lee, and G.A. Moses, "Fireball Dynamics in Preformed Plasma Channels of Light Ion Beam Fusion Reactors," Bull. APS 26, 900 (1981).

UNIVERSITY OF WISCONSIN FUSION ENGINEERING PROGRAM

FUSION DESIGN MEMOS SUPPORTED BY SANDIA CONTRACT

UWFDM #

307. R.R. Peterson and G.A. Moses, "MFP - A Calculation of Radiation Mean Free Paths, Ionization and Internal Energies in Noble Gases," (May 1979).

315. R.R. Peterson and G.A. Moses, "Blast Wave Calculations in Argon Cavity Gas for Light Ion Beam Fusion Reactors," (Oct. 1979).

320. G.A. Moses et al., "First Wall and Cavity Design Studies for a Light Ion Beam Driven Fusion Reactor," (Oct. 1979).

322. R.L. Engelstad and E.G. Lovell, "First Wall Mechanical Design for Light Ion Beam Fusion Reactors," (Dec. 1979).

323. G.A. Moses and R.R. Peterson, "First Wall Protection in ICF Reactors by Inert Cavity Gases," (Oct. 1979).

336. G.A. Moses and R.R. Peterson, "FIRE - A Computer Code to Simulate Cavity Gas Response to Inertial Confinement Target Explosions," (Jan. 1980).

371. R.R. Peterson, G.W. Cooper, and G.A. Moses, "Cavity Gas Analysis for Light Ion Beam Fusion Reactors," (Aug. 1980).

372. R.R. Peterson and G.A. Moses, "MIXER - A Multi-Species Optical Data and Equation of State Computer Code," (Sept. 1980).

382. R.R. Peterson, R.D. Watson, W.G. Wolfer, and G.A. Moses, "TSTRESS - A Transient Stress Computer Code," (Dec. 1980).

405. T.J. McCarville, G.L. Kulcinski, and G.A. Moses, "An Analytical Model for the Motion and Radiative Response of a Low Density Inertial Confinement Fusion Buffer Gas," (Jan. 1981).

406. T.J. McCarville, G.L. Kulcinski, and G.A. Moses, "A Model for the Deposition of X-Rays and Pellet Debris from Inertial Confinement Fusion Targets into a Cavity Gas," (Jan. 1981).

407. T.J. McCarville, R.R. Peterson, and G.A. Moses, "Improvements in the FIRE Code for Simulating the Response of a Cavity Gas to Inertial Confinement Fusion Target Explosions," (June 1981; revised Feb. 1982).

414. B. Badger et al., "Progress Report to Sandia for Light Ion Beam Activities During 1980-1981," (Jan. 1982). (Limited distribution.)

421. E.G. Lovell, R.R. Peterson, R.L. Engelstad, and G.A. Moses, "Transient Elastic Stresses in ICF Reactor First Wall Structural Systems," (Aug. 1981).

423. A.M. Hassanein, T.J. McCarville, and G.L. Kulcinski, "First Wall Evaporation in Inertial Confinement Fusion Reactors Utilizing Gas Protection," (Aug. 1981).

442. R.R. Peterson, K.J. Lee, and G.A. Moses, "Low Density Cavity Gas Fireball Dynamics in the Light Ion Beam Target Development Facility," (Oct. 1981).

455. R.R. Peterson, K.J. Lee, and G.A. Moses, "Fireball Propagation in Preformed Plasma Channels in the Light Ion Beam Driven Target Development Facility," (Jan. 1982).

456. R.R. Peterson, K.J. Lee, A. White, R.L. Engelstad, E.G. Lovell, G.L. Kulcinski, and G.A. Moses, "Choice of First Wall Material in the Light Ion Beam Target Development Facility," (Feb. 1982).

457. B. Badger et al., "Report to Sandia Laboratory on University of Wisconsin Fusion Engineering Program Design Activities for the Light Ion Beam Fusion Target Development Facility from August 1981 to February 1982," (Feb. 1982).

PH.D. THESES SUPPORTED BY SANDIA CONTRACT

T.J. McCarville, "A Numerical Model for Simulating the Dynamic Response of an Inertial Confinement Fusion Cavity Gas to a Target Explosion," University of Wisconsin Nuclear Engineering Department, January 1982. (Current position - TRW.)

D.J. Drake, "Alpha Particle Transport Modeling in Dense ICF Plasmas," University of Wisconsin Nuclear Engineering Department, to finish in March 1982. (Future position - KMS Fusion.)